

Radiation Behavior of High-Entropy Alloys for Advanced Reactors

Nuclear Energy Enabling Technologies

Dr. Peter K. Liaw

University of Tennessee-Knoxville

In collaboration with:

CompuTherm, LLC.

Sue Lesica, Federal POC
Lizhen Tan, Technical POC

Radiation Behavior of High-Entropy Alloys for Advanced Reactors

Final Report

For the period: September 2011 - September 2014

Principal Investigator: Peter K. Liaw¹

Collaborators: Takeshi Egami², Chuan Zhang³, Fan Zhang⁴, and Yanwen Zhang⁵

Students: Wei Guo⁶, Yuting Li⁷, Lou Santodonato⁸, and Zhi Tang⁹

1. The University of Tennessee, 406 Ferris Hall, Department of Materials Science and Engineering, The University of Tennessee, Knoxville, TN, 37996-2200. Phone: (865) 974-6356; Fax: (865) 974-4115; E-mail: pliaw@utk.edu

2. B201 Joint Institute for Neutron Sciences P.O. Box 2008 MS-6453, Oak Ridge, TN, 37831-6453. Phone: (865) 574-5165; Fax: (865) 574-8631; E-mail: egami@utk.edu

3. 437 S. Yellowstone Dr., Suite 217, Madison, WI, 53719-1096. Phone: (608) 274-1414 ext 2; Fax: (608) 274-6045; E-mail: chuan.zhang@computherm.com

4. 437 S. Yellowstone Dr., Suite 217, Madison, Wisconsin 53719-1096. Phone: (608) 274-1414 ext 2; Fax: (608) 274-6045; E-mail: fan.zhang@computherm.com

5. 203 Tandec, Department of Materials Science & Engineering, The University of Tennessee, Knoxville, TN, 37996-1950. Phone: (865) 974-0482; E-mail: yanwen@utk.edu

6. The University of Tennessee, 106 Science & Engineering Research Facility Building, Department of Materials Science and Engineering, The University of Tennessee, Knoxville, TN, 37996-2200. Phone: (865) 974-0645; Fax: (865) 974-4115; E-mail: vigo332@gmail.com

7. The University of Tennessee, 211 Science & Engineering Research Facility Building, Department of Materials Science and Engineering, The University of Tennessee, Knoxville, TN, 37996-2200. Phone: (865) 974-0645; Fax: (865) 974-4115; E-mail: yli82@utk.edu

8. Oak Ridge National Laboratory, Staff and University of Tennessee, Student, 1 Bethel Valley Road Oak Ridge, TN 37831. Phone: (865)719-0656; E-mail: lsantod1@utk.edu

9. The University of Tennessee, 106 Science & Engineering Research Facility Building,

Department of Materials Science and Engineering, The University of Tennessee, Knoxville,
TN, 37996-2200. Phone: (865) 974-0645; Fax: (865) 974-4115; E-mail: cstzhi@gmail.com

Papers

Zhang Y, Zuo TT, Tang Z, Gao MC, Dahmen KA, Liaw PK, et al. Microstructures and properties of high-entropy alloys. *Prog Mater Sci.* 2014;61:1-93.

Zhang Y, Lu ZP, Ma SG, Liaw PK, Tang Z, Cheng YQ, et al. Guidelines in predicting phase formation of high-entropy alloys. *MRS Communications.* 2014;4:57-62.

Tang Z, Huang L, He W, Liaw P. Alloying and Processing Effects on the Aqueous Corrosion Behavior of High-Entropy Alloys. *Entropy.* 2014;16:895-911.

Komarasamy M, Kumar N, Tang Z, Mishra RS, Liaw PK. Effect of Microstructure on the Deformation Mechanism of Friction Stir-Processed Al_{0.1}CoCrFeNi High Entropy Alloy. *Mater Res Lett.* 2014;DOI: 10.1080/21663831.2014.958586.

Antonaglia J, Xie X, Tang Z, Tsai CW, Qiao JW, Zhang Y, et al. Temperature Effects on Deformation and Serration Behavior of High-Entropy Alloys (HEAs). *Jom-Us.* 2014;66:2002-8.

Zuo TT, Ren SB, Liaw PK, Zhang Y. Processing effects on the magnetic and mechanical properties of FeCoNiAl_{0.2}Si_{0.2} high entropy alloy. *Int J Miner Metall Mater.* 2013;20:549-55.

Zhao W, Sun Z, Tang Z, Liaw PK, Li J, Liu RP, et al. ANSYS-Based Simulation and Optimization on Temperature Field of Amorphous Ingot Made by Water Quenching. *Metall Mater Trans A.* 2013;45:2371-5.

Zhang Y, Zuo T, Cheng Y, Liaw PK. High-entropy Alloys with High Saturation Magnetization, Electrical Resistivity, and Malleability. *Sci Rep.* 2013;3:1455. Welk BA, Williams RE, Viswanathan GB, Gibson MA, Liaw PK, Fraser HL. Nature of the interfaces between the constituent phases in the high entropy alloy CoCrCuFeNiAl. *Ultramicroscopy.* 2013;134:193-9.

Tang Z, Gao MC, Diao HY, Yang TF, Liu JP, Zuo TT, et al. Aluminum Alloying Effects on Lattice Types, Microstructures, and Mechanical Behavior of High-Entropy Alloys Systems. *Jom-Us.* 2013;65:1848-58.

Ma SG, Zhang SF, Gao MC, Liaw PK, Zhang Y. A Successful Synthesis of the CoCrFeNiAl_{0.3} Single-Crystal, High-Entropy Alloy by Bridgman Solidification. *Jom-Us.* 2013;65:1751-8.

Laktionova MA, Tabchnikova ED, Tang Z, Liaw PK. Mechanical properties of the high-entropy alloy Ag_{0.5}CoCrCuFeNi at temperatures of 4.2-300 K. *Low Temp Phys.* 2013;39:630-2.

Guo W, Dmowski W, Noh J-Y, Rack P, Liaw P, Egami T. Local atomic structure of a

high-entropy alloy: an x-ray and neutron scattering study. *Metall Mater Trans A*. 2013;44:1994-7.

Zhang Y, Yang X, Liaw PK. Alloy design and properties optimization of high-entropy alloys. *Jom-Us*. 2012;64:830-8.

Hemphill MA, Yuan T, Wang GY, Yeh JW, Tsai CW, Chuang A, et al. Fatigue behavior of Al_{0.5}CoCrCuFeNi high entropy alloys. *Acta Mater*. 2012;60:5723-34.

Presentations

Tang Z, Senkov ON, Zhang C, Zhang F, Lundin CD, and Liaw PK. “Al-Co-Cr-Fe-Ni phase equilibria and properties”. TMS 2015, March 15-19, Walt Disney World, Orlando, FL, USA

Zhang C, Zhang F, Chen SL, Cao WS, Zhu J, Tang Z, Diao HY, and Liaw PK. “Computational-thermodynamics-aided development of multiple-principal-component Alloys”. TMS 2015, March 15-19, Walt Disney World, Orlando, FL, USA

Dahmen KA, Carroll B, Xie X, Chen SY, Antonaglia J, Brinkman B, LeBlanc M, Laktionova MO, Tabachnikova ED, Tang Z, Qiao JW, Yeh JW, Lee C, Tsai VW, Uhl J, and Liaw PK. “A model for the deformation mechanisms and the serration statistics of high entropy alloys”. TMS 2015, March 15-19, Walt Disney World, Orlando, FL, USA

Kumar N, Komarasamy M, Tang Z, Mishra RS, and Liaw PK. “On the friction stress and Hall-Petch coefficient of a single phase face-centered-cubic high entropy alloy”. TMS 2015, March 15-19, Walt Disney World, Orlando, FL, USA

Tang Z, Lundin CD, McHargue CJ, and Liaw PK. “Corrosion-fatigue behavior of a single-phase face-centered-cubic high-entropy alloy”. MS&T 2014. October 12-16, David L. Lawrence Convention Center, Pittsburgh, PA, USA

Tang Z, Yuan T, Tsai CW, Yeh JW, Lundin CD, and Liaw PK. “Fatigue behavior and statistical modeling of cold-rolled $\text{Al}_{0.5}\text{CoCrCuFeNi}$ high-entropy alloys”. MS&T 2014. October 12-16, David L. Lawrence Convention Center, Pittsburgh, PA, USA

Tang Z, Senkov ON, Parish CM, Miracle DB, Zhang C, Zhang F, Gao MC, Liaw PK, and Egami T. “Tensile characterization and in-situ neutron diffraction of as-cast and homogenized AlCoCrFeNi high-entropy alloys”. MS&T 2014. October 12-16, David L. Lawrence Convention Center, Pittsburgh, PA, USA

Tang Z, Gao MC, Diao HY, Yang TF, Liu JP, Zuo TT, Zhang Y, Lu ZP, Cheng YQ, Zhang YW, Dahmen KA, Liaw PK, and Egami T. “Aluminum alloying effects on lattice types, microstructures, and mechanical behavior of high-entropy alloys systems”. TMS 2014, February 16-20, San Diego Convention Center, San Diego, CA, USA

Kai W, Chen WS, Sung CC, Tang Z, and Liaw PK. “The oxidation behavior of AlCoCrFeNi high-entropy alloy at 1023-1323K (750-1050°C)”. TMS 2014, February 16-20, San Diego Convention Center, San Diego, CA, USA

Komarasamy M, Kumar N, Tang Z, Mishra RS, and Liaw PK. “Mechanical behavior of an Al_{0.1}CoCrFeNi high entropy alloy”. TMS 2014, February 16-20, San Diego Convention Center, San Diego, CA, USA

Yang SZ, Habibi MH, Wang L, Guo SM, Tang Z, Liaw PK, Tan LX, Guo C, and Jackson M. “The hot corrosion resistance properties of Al_xFeCoCrNi”. TMS 2014, February 16-20, San Diego Convention Center, San Diego, CA, USA

Xie X, Antonaglia J, Liu JP, Tang Z, Qiao JW, Wang GY, Zhang Y, Dahmen KA, and Liaw PK. “Strain-rate effects on the structure evolution of high entropy alloys”. TMS 2014, February 16-20, San Diego Convention Center, San Diego, CA, USA

Tang Z, Senkov ON, Parish CM, Santodonato LJ, Miracle DB, Wang GY, Zhang C, Zhang F, and Liaw PK. “Non-equilibrium and equilibrium phases in AlCoCrFeNi high-entropy alloys”. TMS 2013, March 3-7, Henry B. Gonzalez Convention Center, San Antonio, TX, USA

Tang Z, Hemphill MA, Yuan T, Wang GY, Yeh JW, Tsai CW, and Liaw PK. “Minor phase and defect effects on fatigue behavior of wrought Al_{0.5}CoCrCuFeNi high-entropy alloys”. TMS 2013, March 3-7, Henry B. Gonzalez Convention Center, San Antonio, TX, USA

Parish CM, Miller MK, Santodonato LJ, Tang Z, and Liaw PK. “Phase separation and intermetallic formation in high-entropy alloys”. TMS 2013, March 3-7, Henry B. Gonzalez Convention Center, San Antonio, TX, USA

Zhang C, Zhang F, Chen S, Cao W, Zhu J, Tang Z, and Liaw PK. “Computational thermodynamics aided high-entropy alloy design”. TMS 2013, March 3-7, Henry B. Gonzalez Convention Center, San Antonio, TX, USA

Santodonato LJ, Zhang Y, Gao MC, Parish CM, Feygenson M, Tang Z, Neuefeind J, Weber R, and Liaw PK. “Ordering behavior in the Al(x)CoCrCuFeNi high-entropy alloys”. TMS 2013, March 3-7, Henry B. Gonzalez Convention Center, San Antonio, TX, USA

Yuan T, Hemphill MA, Tang Z, Wang GY, Chuang CP, Tsai CW, Yeh JW, and Liaw PK. “Statistical fatigue-life modeling for high-entropy alloys”. TMS 2013, March 3-7, Henry B. Gonzalez Convention Center, San Antonio, TX, USA

Yokoyama Y, Xie X, Antonaglia J, Hemphill MA, Tang Z, Yuan T, Wang GY, Tsai CW, Yeh JW, Chuang CP, Dahmen KA, and Liaw PK. “Automatic fabrication of high-entropy alloys and their properties”. TMS 2013, March 3-7, Henry B. Gonzalez Convention Center, San Antonio, TX, USA

Dahmen KA, Xie X, Antonaglia J, Laktionova MA, Tabachnikova ED, Tang Z, Qiao JW, Greer J, Yeh JW, Uhl J, and Liaw PK. “Extracting materials properties from crackling noise and slip avalanche statistics of slowly-sheared materials”. TMS 2013, March 3-7, Henry B. Gonzalez Convention Center, San Antonio, TX, USA

Tang Z, Senkov ON, Miracle DB, Santodonato LJ, Wang GY, Zhang Y, and Liaw PK. “Tensile behavior and fracture mechanism of AlCoCrFeNi high-entropy alloy subjected to hot isostatic pressing and annealing”. MS&T 2012, October 7-11, David L. Lawrence Convention Center, Pittsburgh, PA, USA

Hemphill MA, Tang Z, Yuan T, Wang GY, Yeh JW, Tsai CW, Chuang CP, and Liaw PK. “Fatigue behavior of Al_{0.5}CoCrCuFeNi high-entropy alloys”. MS&T 2012, October 7-11, David L. Lawrence Convention Center, Pittsburgh, PA, USA

Zhang Y, Tang Z, Santodonato LJ, Hemphill MA, Wang GY, Gao MC, and Liaw PK. “Mechanical behavior of high-entropy alloys”. MS&T 2012, October 7-11, David L. Lawrence Convention Center, Pittsburgh, PA, USA

Santodonato LS, Zhang Y, Feygenson M, Neuefiend J, Tang Z, Weber R, Gao MC, and Liaw PK. “Experimental study of local and long-range atomic ordering in the high-entropy Al_xCoCrCuFeNi alloys during solidification”. MS&T 2012, October 7-11, David L. Lawrence Convention Center, Pittsburgh, PA, USA

Dahmen KA, Xie X, Antonaglia J, Laktionova MA, Tabachnikova ED, Tang Z, Qiao JW, Greer J, Yeh JW, Uhl J, and Liaw PK. “Extracting materials properties from crackling noise and slip avalanche statistics of slowly-sheared materials”. MS&T 2012, October 7-11, David L. Lawrence Convention Center, Pittsburgh, PA, USA

Networks or Collaborations Fostered

Prof. Nagase in Osaka University

Prof. Phil Rack in the University of Tennessee

Dr. George M. Stocks in Oak Ridge National Laboratory

Dr. Michael C. Gao in National Energy Technology Laboratory

Prof. Rajiv Mishra in University of North Texas

Prof. Julia Greer in California Institute of Technology

Prof. Karin Dahmen in University of Illinois at Urbana-Champaign

Prof. Yong Zhang in University of Science and Technology Beijing

Prof. Jien-Wei Yeh in National Tsing Hua University

Drs. Oleg N. Senkov and Daniel B. Miracle in Air Force Research Laboratory

Prof. Junwei Qiao in Taiyuan University of Technology

Prof. Fuqian Yang in University of Kentucky

Dr. Tengfei Yang in Peking University

Dr. Yongqiang Cheng in Oak Ridge National Laboratory

Summary

In the first task, we have demonstrated the radiation damage and the recrystallization behaviors in multicomponent alloys through molecular-dynamics simulations. It is found that by alloying with atoms of different sizes, the atomic-level strain increases, and the propensity of the radiation-induced crystalline to amorphous transition increases as the defects cluster in the cascade body. Recrystallization of the radiation induced supercooled or glass regions show that by tuning the composition and the equilibrium temperature, the multicomponent alloys can be healed. The crystalline-amorphous-crystalline transitions predict the potential high radiation resistance in multicomponent alloys.

In the second task, three types of high-entropy alloys (HEAs) were fabricated from AlCoCrFeNi and AlCuCrFeNi quinary alloys. Hardness and reduced contact modulus were measured using nanoindentation tests. Heavy ion irradiation were performed using 10 MeV gold and 5 MeV nickel to study radiation effects. Al_{0.5}CrCuFeNi₂ shows phase separation upon the presence of copper. Both hardness and contact modulus exhibit the same trend as increasing the applied load, and it indicates that excessive free volume may alter the growth rate of the plastic zone. The as-cast Al_{0.1}CoCrFeNi specimen undergone the hot isostatic pressing (HIP) process and steady cooling rate which mitigate the quenching effect. The swelling behavior was characterized by the atomic force microscopy (AFM), and the swelling rate is approximately 0.02% dpa. Selected area diffraction (SAD) patters show irradiation-induced amorphization throughout the ion projected range. Within the peak damage region, an amorphous ring is observed, and a mixture of amorphous/ crystalline structure at deeper depth is found. The Al_{0.3}CoCrFeNi HEAs shows good radiation resistance up to 60 peak dpa. No voids or dislocations are observed. The crystal structures remain face-centered-cubic (FCC) before and after 5 MeV Ni irradiation. Higher dpa might be required to study defects formation mechanisms.

In the third task, all the constituent binary and ternary systems of the Al-Co-Cr-Fe-Ni system were thermodynamically modeled within the whole composition range. Comparisons between the calculated phase diagrams and literature data are in good agreement. The multi-component thermodynamic database of the Al-Co-Cr-Fe-Ni system was then obtained via extrapolation. The current Al-Co-Cr-Fe-Ni thermodynamic database enables us to carry out the calculations of phase diagrams, which can be used as useful guidelines to identify the Al-Co-Cr-Fe-Ni HEAs with desirable microstructures.

In the fourth task, we discuss how as-cast and homogenized phases can be identified, what

phases are usually found in the as-cast and homogenized conditions, and what the thermodynamics and kinetics of phase transformations are in the AlCoCrFeNi HEA. The microstructure and phase composition were studied in as-cast and homogenized conditions. It showed the dendritrical structure in the as-cast condition consisting primarily of a nano-lamellar mixture of A2 [disorder body-centered-cubic (BCC)] and B2 (ordered BCC) phases, in addition to a very small amount of A1 [disorder face-centered-cubic (FCC)] phases. The homogenization heat treatment resulted in an increase in the volume fraction of the A1 phase and formation of a Sigma (σ) phase. Tensile properties in as-cast and homogenized conditions are reported at 700 °C. Thermodynamic modeling of non-equilibrium and equilibrium phase diagrams for the AlCoCrFeNi HEA gave good agreement with the experimental observations of the phase contents. The reasons for the improvement of ductility after the heat treatment are discussed.

1. Task 1: First-Principles Calculations and Molecular-Dynamics (MD) Simulations

1.1. Introduction

The emerging applications of high-entropy alloys (HEA, also known as multicomponent alloys) intrigue extensive research interests in the metallurgy community, since the early proposal by Yeh [1] and Cantor [2]. Besides the mechanical properties of high strength [3], high toughness [4], excellent wear resistance, and good corrosion and oxidation resistances [5], the radiation properties of HEAs demand special attention [6]. Since atoms of different sizes and chemistries reside in the lattice, which is not specifically designed for each individual atom, the atoms are under considerable stresses, which distort the lattice and increase the lattice friction for dislocations [7]. Consequently, the HEAs are not stable and can be vitrified under irradiations. The radiation-induced amorphization region, however, can be healed by the following recrystallization upon cooling through the heat dissipation to the matrix. In this sense, HEAs are inherently radiation resistant. By using molecular dynamics (MD) simulations and the first-principles calculations, this part of work aimed at providing some fundamental information about the radiation-damage effect and the recrystallization in multicomponent alloys, which can provide guidelines for the alloy design.

The defect production by irradiation and their recombination determines the performance and life of the nuclear reactor materials [8, 9]. As we aim to develop suitable HEAs for the radiation resistance purpose, it is important to study how the primary damage plays its role in the HEAs. The principal questions are two-folds: First, how does the multi-component system affect the radiation cascades, specifically, the number of surviving vacancies and interstitials after primary knock-on atom (PKA) induced cascades? Second, how does the multicomponent system affect the recrystallization process, which to some extent is the self-healing effect, after the cascades? To address these two questions, we studied the following aspects, which are further organized into three subtopics. Firstly, we examined the PKA atomic-size effect on the threshold displacement energy in quinary systems and its effect in terms of creating stable defects in binary systems. Secondly, we studied the primary damage in quinary systems with a focus on the defect production and annealing treatment. Thirdly, the recrystallization processes in quinary systems were investigated. Through these studies, we have achieved a comprehensive understanding about the radiation damage properties and a sensible prediction about the radiation tolerance in HEAs.

The research on HEAs is still at an early stage. In particular, very little is known about the irradiation effects on these alloys, even though the initial results indicate that they are excellent irradiation-resistant materials [6]. Thus, we focused our initial effort on gaining knowledge concerning the general behavior of the multi-component systems, rather than

studying specific alloys systems. Much of the research on HEAs is now directed to the $3d$ transition metal alloys, but as the research advances, we may find different kinds of alloys to be more suitable for the irradiation resistance. Therefore, we decided to concentrate our effort on the study of the atomic size effect using model systems. We strongly suspect that it is the atomic size effect, not specific chemistry, which plays the decisive role in the irradiation effects in HEA. Thus, we chose a very simple model of iron interacting with the modified Johnson potential, scaled to represent the atomic-size effect. Consequently, the results are not expected to reflect any realistic alloys. On the other hand through this initial study, we garnered a large amount of knowledge about the size effect, without the interference from the chemical effect. As the preparation for the next stage of research, we are now undertaking some first-principles calculations of the atomic-level stresses on $3d$ -transition metal HEAs.

1.2. The Primary Knock-on Atom Size Effect

Previous radiation studies by molecular-dynamics simulations were carried out extensively in monatomic body-centered cubic (bcc), face-centered-cubic (fcc), and hexagonal-close-packed (hcp) systems such as Cu [10-12], Fe [13-17], Mo [18], V [19], Ni [10], Ti [20], and Zr [21, 22]. The radiation induced defect production and displacement cascade evolutions in binary systems, such as Fe-Cu [23], Ni₃Al [24, 25], Cu-Au [26], and Cu-Ti [27] were also studied. However, due to the absence of applicable potentials for multiple elemental interactions, the radiation behavior in multicomponent alloys has not yet been studied. It is natural to raise the question that what is the effect of the PKA atomic species on the radiation damage in multi-component high-entropy alloys.

Gao and Bacon [25] noted that in the Ni₃Al system, for primary recoils with energy more than a few hundred eV, there is no obvious difference in the cascades generated by different PKAs with energy not exceeding 5 keV. Deng and Bacon [26] also reported that there is no remarkable difference between low energy cascades initiated by Au or Cu PKAs in the ballistic/collision phase. Neither is there any difference when the mass of the PKAs is reduced by purpose. This also applied in Cu-Ti systems [27]. Ackland [23] observed the slight difference in both the defect migration energy and the threshold displacement energy calculated between Cu and Fe PKAs in a dilute Fe-Cu alloy with a many-body potential. However, Calder *et al* [17] demonstrated that the total number of defects decreases with the PKA mass and the cascade effect is stronger at lower energy. The difference between the two conflicting results may root from the PKA energy applied: Calder [17] used the PKA energy ranging from 5 - 20 keV while others used the energy not exceeding 5 keV. Nevertheless, to our knowledge, the previous results focus mainly on the mass of the PKAs, but the effect of the PKA size on the cascades in metals has not been studied thoroughly by MD simulations.

It is popular to adopt the embedded atom methods (EAM) to define the atomic interaction potential, in which along with the pair potential, an embedding energy term is associated to the atom [28-31]. Based on the density functional theory, Dow and Baskes [28-30] derived the embedding energy to be related to the background electron density, which is a simple function of the atomic density determined by the atomic positions. The Finnis and Sinclair [31] potential used a polynomial form for the electron density function and a square root function for the embedding energy term to mimic the results of the tight-binding theory. The EAM potentials are advantageous to fit the Cauchy relationship in order to obtain satisfactory elastic moduli, Poisson ratio and the vacancy formation energy in real materials over pair potentials [31]. The previous results listed before [10-27] mainly used the EAM potentials. However, it is rather complicated to build specific EAM potentials for multiple atomic interactions. For simplicity we choose the pair potentials which are to be scaled according to the atom sizes to demonstrate the PKA size effect. This approach avoids the embedding energy terms which account for a sizable portion of the potential energy but are less important to the PKA size effect.

1.2.1. Simulation Methods

In this subsection, both binary and quinary body-centered-cubic (BCC) solid solution systems are modeled for different purposes. In binary systems, the model systems used are the binary A-B random solid solution systems, in which A is Fe and B is a fictitious element, Fe', which is Fe with an expanded atomic size. In the crystalline state they have the bcc structure. In this model the Fe' atom has the same mass as Fe but the radii of Fe and Fe' atoms, R_A and R_B , have the ratio of $R = R_B/R_A$, where R is the atomic size ratio which equals to 1.15 which is within the Hume-Rothery rule. The interatomic interaction is defined by a scaled modified Johnson potential (mJp) rather than the original mJp itself. The interatomic force is scaled according to the pair type and distance. For Fe-Fe pairs, it is the same as in mJp, while for Fe-Fe' and Fe'-Fe' pairs of atom i and j , the interatomic potentials are defined as: $V_{ij}(r) = \xi \phi(r/\xi)$, where ϕ is the interatomic potential between Fe-Fe atoms and ξ is the scaling factor. Thus the interatomic force is obtained as:

$$\frac{dV_{ij}(r)}{dr} = \frac{d(\xi \phi(\frac{r}{\xi}))}{dr} = \frac{d\phi(\frac{r}{\xi})}{d(\frac{r}{\xi})} = \frac{d\phi(r')}{dr'} \quad (1.1)$$

where $r' = r/\xi$. Atoms with different sizes are treated so that they have similar force and acceleration when interacting with Fe atoms. Thus, only the atomic size effect is changed with varying compositions. The cutoffs of the potentials are 3.44ξ Å and the potential minimums are -0.2516ξ eV for different i - j pairs. In order to adjust the atomic size mismatch, the B content was changed from 0 - 100% with different R in model systems which contain

250,000 atoms. For quinary systems, concentration of each element is 20%, and the atomic sizes are $1-2\delta$, $1-\delta$, 1 , $1+\delta$, $1+2\delta$ times the size of the atom in the monatomic Fe systems using the original modified Johnson potential, whereas, δ is a mismatch factor ranging from 0 - 5%. The interatomic potentials between different elements in the quinary systems are defined similar to the binary system. The systems are relaxed using a number-pressure-temperature (NPT) ensemble at 0 K for a long time to reach equilibrium states.

The threshold displacement energy in a certain crystallographic direction was determined by creating a stable defect from PKA events where the kinetic energy was assigned to an iron atom from a random lattice site. The PKA events are repeated for several times with the energy resolution of 1 eV. The cascade study of the PKA size effect in binary systems was carried out using a 5 keV PKA of different species. The surviving number of defects was monitored after long time relaxation.

1.2.2. Threshold Displacement Energy

In order to produce stable Frenkel defects (pairs of vacancy and interstitial), a minimum kinetic energy, that is the displacement threshold energy E_d , is needed for the PKA. The E_d is essential to evaluate the number of Frenkel pairs N_{FP} an projectile particle produces. The Kinchin-Pease [32] or the NRT (Norgett-Robinson-Torrens) [33] model states:

$$N_{FP} = \frac{0.8T}{2E_d}, \quad (1.2)$$

whereas, T is the PKA kinetic energy. For a specific metal, E_d varies in different crystallographic directions due to the different packing efficiencies (usually explained as the ease of the 'lenses' needed to penetrate), and it is difficult to accurately measure in experiments. However, with the aid of computer simulations, it is viable to obtain E_d with satisfactory accuracy from reasonable potentials. The average threshold energy is about 15 - 50 eV for metals [34].

Since the pair potentials are used in the current work, it is necessary to compare the results with previous reports using EAM or F-S potentials.

Table 1 lists the E_d in different orientations of bcc iron at 0 K using the mJp. Figure 1 shows the angular dependence of the E_d with respect to the [100] direction. Note that during the simulation, the E_d values are tested by an increment of 1 eV of a random PKA, indicating that the errors are within ± 0.5 eV. The E_d values of in [100] and [210] are 21 and 51 eV, which agree with previous results by Bacon [11] and Ackland [23] using the F-S potentials. Other than these two directions, the E_d values show significant disagreements. For example, the E_d in the [110] direction is 46 eV, which is about 50% larger than that in Ref. [11] and [23]. In the previous reports, it was difficult to obtain the threshold in the [111], [221], and [211] directions due to the generation of a long replacement-collision sequence (RCS) in the

directions near the close packed rows [11], consequently, there are three peaks in the threshold curve that are indispensable to produce stable Frenkel defects [11]. However, in our results, except for the [532] direction, the threshold curve shows rather continuous and smooth transition. The general trend of the curve is: when the recoil projectile is within 20° to the [100] direction, the threshold is close to the minimum; it further reaches a maximum when the angle is around 35° at [211] direction with a peak value of 71 eV; the threshold fluctuates between [110] and [111] direction with a magnitude not exceeding 20 eV.

It is not a surprise at all to observe the two distinct curves if one considers the difference between the potentials used. In the previous studies, the potentials used connect the universal Ziegler-Biersack-Littmark (ZBL) potential, which is very strongly repulsive in the short range interaction. The strong repulsive force and the focused energy in the compact direction can easily triggers the RCS. However, in the current work, the short range interaction of the mJp is rather soft, in this case, the RCS can be easily affected and terminated by other neighbors. The [111] crowdion defects can easily migrate to the [110] dumbbells given the activation energy of 0.33 eV for rotation [35] and the formation energy of the latter is ~ 0.5 eV, smaller than the former [36], and thus the chance of producing stable Frenkel defects is high. Except for the difference in the potential and the threshold energy in different directions, it should be noted that the mechanism of the PKA recoil in the [100], [110], and [111] directions agree with previous descriptions [11, 23]. However, the obvious large threshold in the [532] direction is different. Our observation is that in this high order direction, there is no RCS in any of the close-packed direction, and the energy dissipation after the PKA initiation is rather fast due to the quick recombination of defects in a very small volume.

Table 2 lists the E_d values in the [111] direction with different PKA atom species in the quinary bcc systems with different atomic size mismatch ratio δ . It is shown that for the PKA with the atomic size of Fe, as the atomic size ratio factor δ increases, the threshold energy fluctuates significantly with a minimum of 30 eV and a maximum of 46 eV. When the PKA atoms are changed to smaller or larger atoms, the thresholds decrease to 90% or even 50% of that from the Fe PKAs. Note that the number densities of the six systems are 0.08547, 0.08542, 0.08526, 0.08498, 0.08437, and 0.08322 \AA^{-3} , which are less than 2.6% in difference.

It is thus clear that by mixing the crystalline lattice with varying types of atoms, the local distortion in the lattice effectively decreases the threshold displacement energy. Table 6-2 implies that by alloying the system, the defects production might become quite different from the monatomic systems. Indeed, the process of obtaining E_d is quite different from the radiation cascades between which the energy used and the atoms involved are not similar in the two cases. Thus, the study of the cascades in multicomponent systems is a necessity. However, we always bear in mind that the NRT model is a major reference for the defect comparison in different systems.

Table 1. The threshold displacement energy E_d vs. crystallographic directions in bcc iron system at 0 K with modified Johnson potential. Note that the errors are within ± 0.5 eV.

Direction	E_d	Angle
$\langle 100 \rangle$	21	0
$\langle 110 \rangle$	46	45
$\langle 111 \rangle$	41	54.74
$\langle 210 \rangle$	51	26.57
$\langle 211 \rangle$	71	35.26
$\langle 221 \rangle$	26	48.19
$\langle 310 \rangle$	25	18.43
$\langle 311 \rangle$	42	25.24
$\langle 321 \rangle$	68	36.7
$\langle 332 \rangle$	28	50.24
$\langle 401 \rangle$	21	14.04
$\langle 411 \rangle$	33	19.47
$\langle 421 \rangle$	51	29.21
$\langle 431 \rangle$	65	38.33
$\langle 432 \rangle$	28	42.03
$\langle 433 \rangle$	31	46.69
$\langle 443 \rangle$	30	51.34
$\langle 510 \rangle$	20	11.31
$\langle 521 \rangle$	28	24.09
$\langle 531 \rangle$	61	32.31
$\langle 532 \rangle$	101	35.8
$\langle 553 \rangle$	28	49.39

Table 2. The threshold displacement energy E_d in the $\langle 111 \rangle$ directions vs. PKA element species with various atomic size ratio factor δ in quinary systems at 0 K. Note that the errors are within ± 0.5 eV.

δ	r	$(1-2\delta)r$	$(1+2\delta)r$
0	41	-	-
0.01	43	35	38
0.02	36	32	28
0.03	46	26	25
0.04	30	28	32
0.05	46	23	27

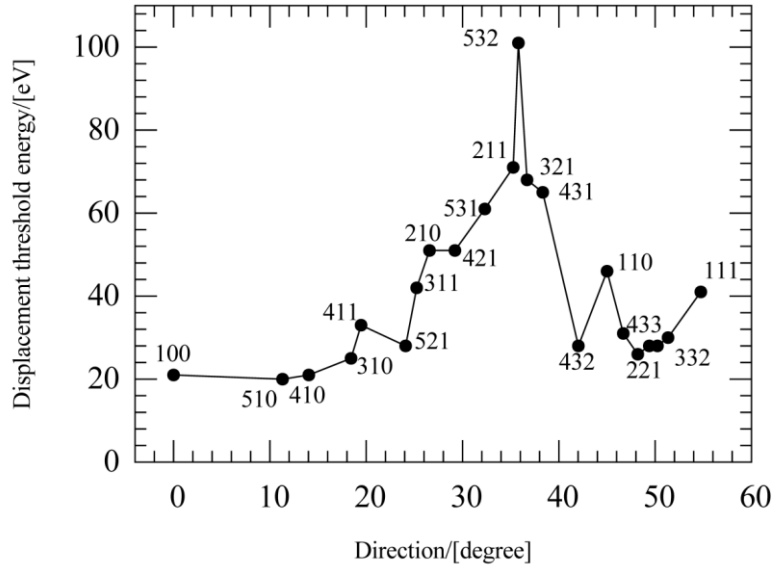


Figure 1. The threshold displacement energy E_d curve for α iron at 0 K using modified Johnson potential. The directions are calculated with respect to the [100] direction. Note that the errors are within ± 0.5 eV.

1.2.3. The Surviving Defects from Different PKA

For simplicity, we applied the A-B binary model to study the PKA size effect. The radius of B atom is 15% larger than A atoms. Figure 2 shows the average number of surviving defects (Frenkel pairs) displaced by 5 keV A/B PKAs in systems with different B atom concentrations after 101 ps. There are three features to be noted.

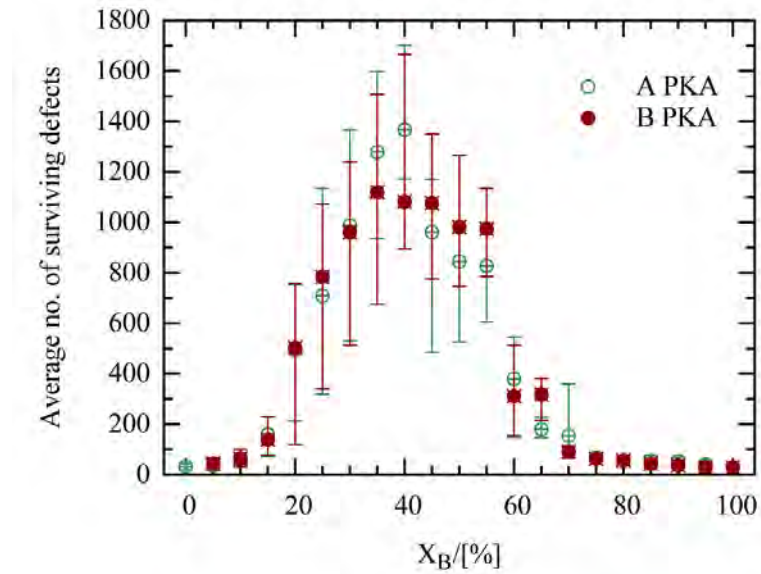


Figure 2. The average number of surviving Frenkel pairs generated by single 5 keV A/B PKA cascades in the binary A-B systems with various X_B concentrations. Note that the atomic size

ratio is $R_B/R_A = 1.15$.

First, a general trend which applies for either PKA type is that when the system is alloyed, the average defect amount increases as the solute concentration increases. The defect amount can increase 30 times when the solute concentration increase from 0 to 40%. It is also understandable that the deviation of the statistics is high in the alloyed region. As indicated by the error bars showing the minimum and maximum, the magnitude of the deviation in some cases can be as large as 50%, which states that the defect production is quite a stochastic process. The alloying effect on the lattice stability due to the local atomic level strain has been discussed in [37], and the results agree with the threshold displacement energy calculated in the previous section.

Second, it is clear that in systems with low solute concentration, there is no remarkable difference in the defect amounts by cascades from A/B PKAs. For example, when the B atom concentration is less than 20% or larger than 70%, the defect amount difference is marginal. When the B atom concentration is between 20% and 70%, the defect amount difference is notable. Especially when the large solute concentration is between 35% and 55%, the defect amount difference can be as large as 30%. However, the difference is still small if compared with the data between different compositions.

The third feature is that the fluctuation of the average number of defects generated by the smaller PKA is greater than the larger PKA. There are two drastic decreases in the defect number as observed when the solute concentration increases from 40% to 45% or from 55% to 60% when the PKA is A atom. However, there is only one sharp decrease at 60% when the PKA is B atom, and the average defect number kept rather stable in the region of 35% to 55% X_B .

Overall, the average number of surviving defects depends only slightly on the PKA size due to the stochastic process of cascade development. In the low alloyed systems, the difference is not obvious; in the highly alloyed systems, the cascade efficiency is slightly different whereas the small PKAs have larger fluctuations. Nevertheless, it is hard to draw a general conclusion that which PKA creates more defects since the difference due to the different PKA is overshadowed by the composition variation.

1.2.4. Discussion and Conclusions

As introduced earlier, previous results focused on the radiation damage of monatomic or binary alloys with fixed compositions, which left the systematic study of the effect of local lattice distortion untouched. The local distortion is rather significant which could not be neglected and cannot be disguised by thermal vibration [37, 38]. Indeed, the atomic level stress calculations do show some correlation between the initial level of stress and the cascade efficiency. Figure 3a shows the average atomic level shear stress before and after the

cascades in the binary systems with A/B PKAs. Note that in these simulations the mJp is connected with the universal ZBL potential using a fifth order polynomial between 1.2 and 2 Å following Ref. [13] and then further scaled according to the atomic sizes. The local stress increases as the remaining defects distort the lattice. The general trend of Figure 3b agrees with Figure 2. For example, the stress increase in low solute systems is rather small as compared with that in the highly alloyed systems. Also the stress difference by the A/B PKAs is also overshadowed by that in different compositions.

It thus can be concluded that the PKA size effect on the defect production is rather small and can be neglected in the low solute systems. In high concentration systems, the difference in some cases can be large as indicated by the large fluctuation of statistics. But in any cases, the effect of composition on the surviving defects is more significant.

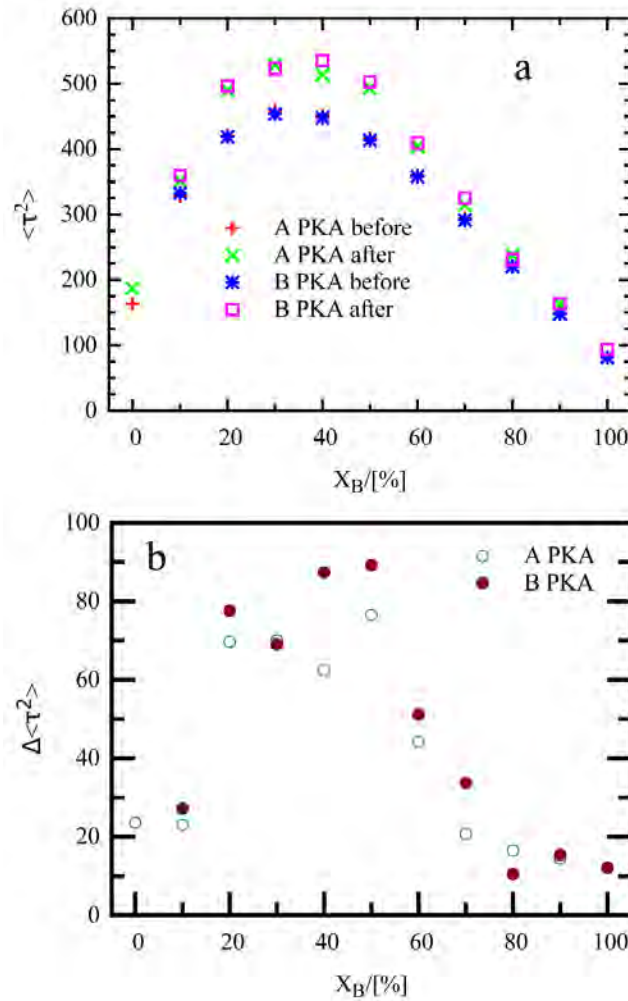


Figure 3. The atomic level shear stress calculated before and after a 5 keV A/B PKA initiated cascade (a). The mJp is connect to a ZBL universal potential between 1.2 and 2 Å using a fifth order polynomial. The atomic size ratio is 1.15. The difference of the atomic level shear stress after cascades (b).

1.3. Primary Damages and Defect Production in Quinary Systems

HEAs are usually defined to contain 5 or more elements with nearly equal concentrations. The variation of the chemistry and size of the atoms will cause the lattice strain as illustrated previously. The proposed problem that how the local distortion affect the radiation behaviors has not been studied before. The chemistry is rather difficult to tackle for the alloys since it involves the electron structure, band structure, magnetism, density of state, and phonon dispersion calculations between different atoms. Modern approaches using density functional theory and *ab initio* simulations are successful to calculate the local strain and the elastic properties [39, 40] to predict the properties of multicomponent alloys. The problem is that these calculations are rather expensive if applied to study the radiation behaviors such as the cascades. The time and size scale using *ab initio* simulations are very limited. However, the atomic size effect on the radiation damage can be investigated through MD simulations as we have already studied in binary systems. Classic MD can be very efficient to handle systems with million atoms to timescales long enough for the radiation damage studies. The challenge roots in that there is no applicable interatomic potentials for systems with so many elements. For a better demonstration of the atomic size effect, it is reasonable to simplify the problem by linking the potential with the atomic sizes. In this section, we extend the previous methods of scaling the potential with atomic sizes to study the radiation cascades in the equi-molar quinary systems. By comparing the cascade behaviors in multicomponent and monatomic systems with previous results [11, 13, 17, 23, 41, 42], a comprehensive understanding of how the alloy design by choosing the element sizes affects the radiation behaviors will be provided.

1.3.1. Simulation Methods

The simulations start from bcc crystalline lattices. The 5 element types of varying sizes are randomly assigned to the atoms on the lattice to mimic random solid solutions. The amount of each atom type is equal to 20% of the system, which contains 250,000 atoms in total. The atomic radii of the 5 elements are set to be $1-2\delta$, $1-\delta$, 1 , $1+\delta$, and $1+2\delta$ times R_{Fe} , the radius of iron in the modified Johnson potential, and δ is the atomic size mismatch factor of the simulated systems ranging from 0 - 5%. The interatomic potentials are defined according to the atomic sizes of the pairs, as already introduced before. In this case, there are 15 pair types in the quinary systems. The initial lattice constants are presumed to be the same as pure iron, which also meet the Vegard's law due to the cancellation of the positive and negative scaling of the atomic sizes. After the construction of the crystalline lattices, the systems are equilibrated using a NPT ensemble for 50 ps at 300 K. Afterwards, an atom, which located at the position of about 0.3 times the box length away from the simulation box edges with a radius of R_{Fe} is chosen as the PKA. The direction of the recoil is chosen to be $\langle 111 \rangle$ because the threshold displace energy in this direction is close to the average value of all directions as tested in Figure 1. The kinetic energy of the PKAs ranges from 0.5 - 5.5 keV.

Note that the simulation box size and the number of atoms are large enough to contain the PKAs and cascades. The time step for the Verlet leapfrog integration of the Newtonian equations is set to be 0.01 fs for the initial 2 ps, and is changed to 0.02 fs for the subsequent 2 ps, and then 0.05 - 1 fs for varying but long enough durations. This variation is necessary because for high recoil energy cases the energy transfer between the PKA and neighbors needs be evaluated more frequently to avoid error and channeling. The simulations are terminated after ~ 700 ps, which is long enough for defects evolution. Since the initiation of the PKA recoil, the NVT ensemble and periodic boundary conditions are employed for all the simulations. The calculations are repeated, with PKAs of same element species at different lattice sites, for 5 times for each combination of PKA energy and δ to improve statistics.

The defect identification through analyzing the trajectory by computer algorithms can be accomplished mainly by two methods, the Wigner-Seitz cell and the displaced atom methods [42]. For the former method, when there is no atom in the W-S cell of a lattice site, this site is defined as a vacancy; when there are more than one atoms inside the W-S cell, these atoms are called self-interstitial atoms (SIA). The latter method used an empirical value, for example, $0.3a$ (a is the lattice constant), to distinguish the displaced atom. If one atom is displaced more than $0.3a$ away from a lattice site, it is considered as an interstitial; while if there is no atom closer than $0.3a$ to a lattice site, the lattice site is identified as a vacancy. Both of the two methods require a reference lattice, usually the initial perfect lattice before radiation. The advantages and drawbacks of both of the two methods are summarized in Ref. [42]. In this work, we use the displaced atom method due to its simplicity, efficiency and clarity of defects identification.

1.3.2. Results

Figure 4 shows the potential energy (PE) per atom plotted against temperature for pure bcc iron and five equi-molar quinary bcc systems with atomic size mismatch factor δ ranging from 1 - 5%. The NPT ensemble was used for the volume scaling. For the monatomic system, the PE increases with temperature linearly below ~ 2100 K. The PE jump at 2100 K indicates the phase transition from solid to liquid, and the PE difference per atom is 0.2 eV, which corresponds to the latent heat. As we increase the atomic size mismatch, the energy of the system increases as indicated by the superposition of the PE curves. The PE increase does not exceed 0.08 eV for the largest difference. Furthermore, the melting temperature and the latent heat decrease as δ increases. This is reasonable because the local distortion by the atomic size mismatch subsidize the thermal vibration effect towards melting. Nevertheless, since the radiation PKAs are initiated at 300 K, and the temperature rise does not exceed 100 K in each systems, it is feasible to evaluate the radiation damage far under the melting temperature for each systems. In the liquid state PE is almost independent of the atomic size. This is because in the liquid state the structure is adjusted to accommodate the size differences. Consequently the atomic level stresses are independent of the composition and size [37], and PE reflects

this independence.

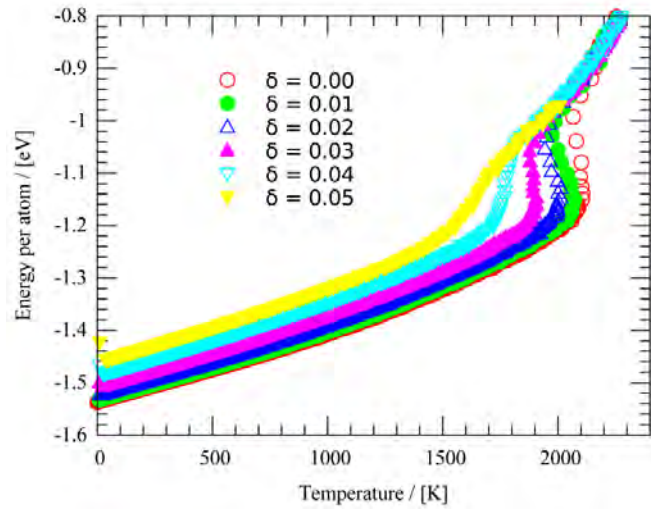


Figure 4. The potential energy per atom vs. temperature plot of monatomic system ($\delta = 0$) and quinary systems with atomic size ratio factor δ ranging from 0.01-0.05. The NPT ensemble is used. The potential energy jump at high temperature in each system corresponds to the melting temperature T_m . The T_m of monatomic system is about 2100 K. The T_m decreases as the δ increases.

Figure 5 through Figure 7 shows the snapshots of the cascades at different times during evolution by 5 keV $\langle 111 \rangle$ PKAs in three different systems. For the pure bcc iron, the cascade morphology is similar to previous studies [13]. In the early stage within 0.1 ps, the PKA knocks the lattice atoms off their sites to produce interstitials and creates the high density vacancy region backwards as the 'spaghetti' region [42]. The cascade region continues to expand and the displaced atoms develop into the $\langle 111 \rangle$ focused replacement chains. The RCS chains are further detached from the main body of the cascade, and they further evolve into $\langle 111 \rangle$ replacement chains and $\langle 110 \rangle$ dumbbell defects as illustrated in the snapshots from 0.38 to 0.93 ps. The defects start to recombine after some time and the cascade starts to decay as the energy in the cascade core dissipates. Quite a large amount of Frenkel pairs are created outside the cascade body due to the heat production and they soon recombine locally. The displaced atoms further evolve during the annealing of the cascades, and after a long time evolving, they become stable defects in the form of clusters, single interstitials or vacancies, $\langle 110 \rangle$ dumbbells, and $\langle 111 \rangle$ crowdions.

Except for the amount of displaced atoms, there is no obvious difference in the morphology between the cascades in different systems during the very early stages. However, after about 1 ps, inhomogeneity develops in the cascade body with the increase in the atomic size mismatch factor δ . As shown in the snapshots of 1.08 ps in Figure 6, 1.27 and 1.58 ps in Figure 7, the cascade body stretches out in several directions as the density of displaced atom

in those directions increases. This phenomenon is most exaggerated when δ reaches 0.05. Further observation shows that the displaced atoms in these regions are mostly elastically deformed as compared with the perfect lattice of the reference. This is not a simple artifact of the displaced atom method used since the same method is employed for all the cascades in different systems. The reason why increasing δ induces inhomogeneity is still unknown, but the elastic deformation due to the high thermal expansion in the matrix is well understood and known as the Eshelby inclusion problem [43]. Details about the shape and the elastic stress and strain Eshelby field is beyond the scope of this work, and they can be found in similar cases as discussed elsewhere [44].

The final structures after the cascade relaxation are also different when increasing the atomic size mismatch factor δ . As shown in Figure 5, the cascade in the $\delta = 0.00$ system is fully annealed after about 6 ps and the defects are rather stable after 701 ps till the end of the simulation. The defects are mainly individual vacancies, interstitials, and some $\langle 110 \rangle$ dumbbells. The dumbbells are prone to form clusters within the previous cascade body. This is similar in the $\delta = 0.03$ case as shown in Figure 6. The clustering of the dumbbells is more frequently found with larger cluster sizes. However, the cascade fails to fully anneal after a very long time till the end of the simulation in the $\delta = 0.05$ system as shown in Figure 7. The D-A analysis show that the remnant of the cascade body is full of interstitials and vacancies as compared with the perfect reference lattice. Further observations show that the interstitial density in this region is rather homogeneous. Thus, it is better to name this region radiation induced amorphous area. By comparison, we still perceive the atoms in this region as defects.

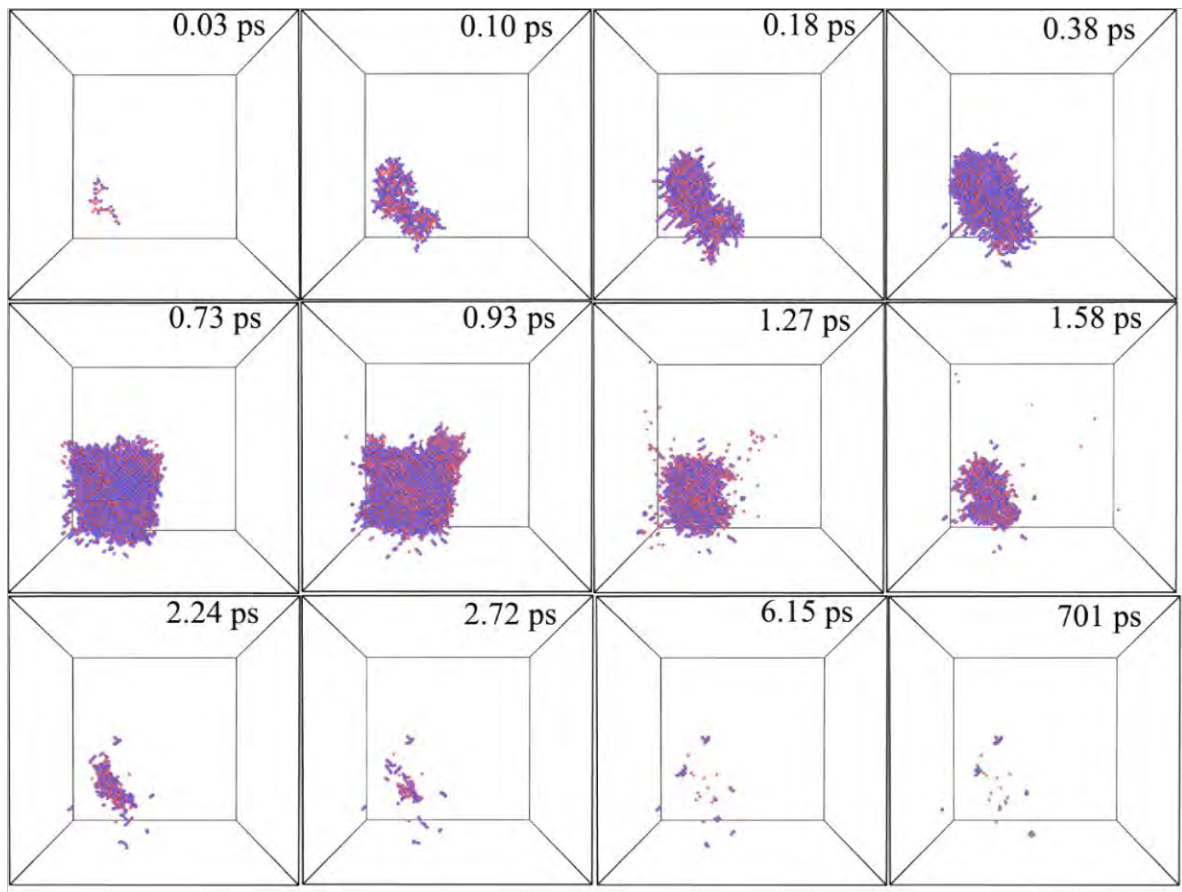


Figure 5. The snapshots of the cascade evolution by a 5 keV $\langle 111 \rangle$ PKA in the pure iron system at different times. The vacancies are represented by red spheres and the interstitials are represented by blue spheres.

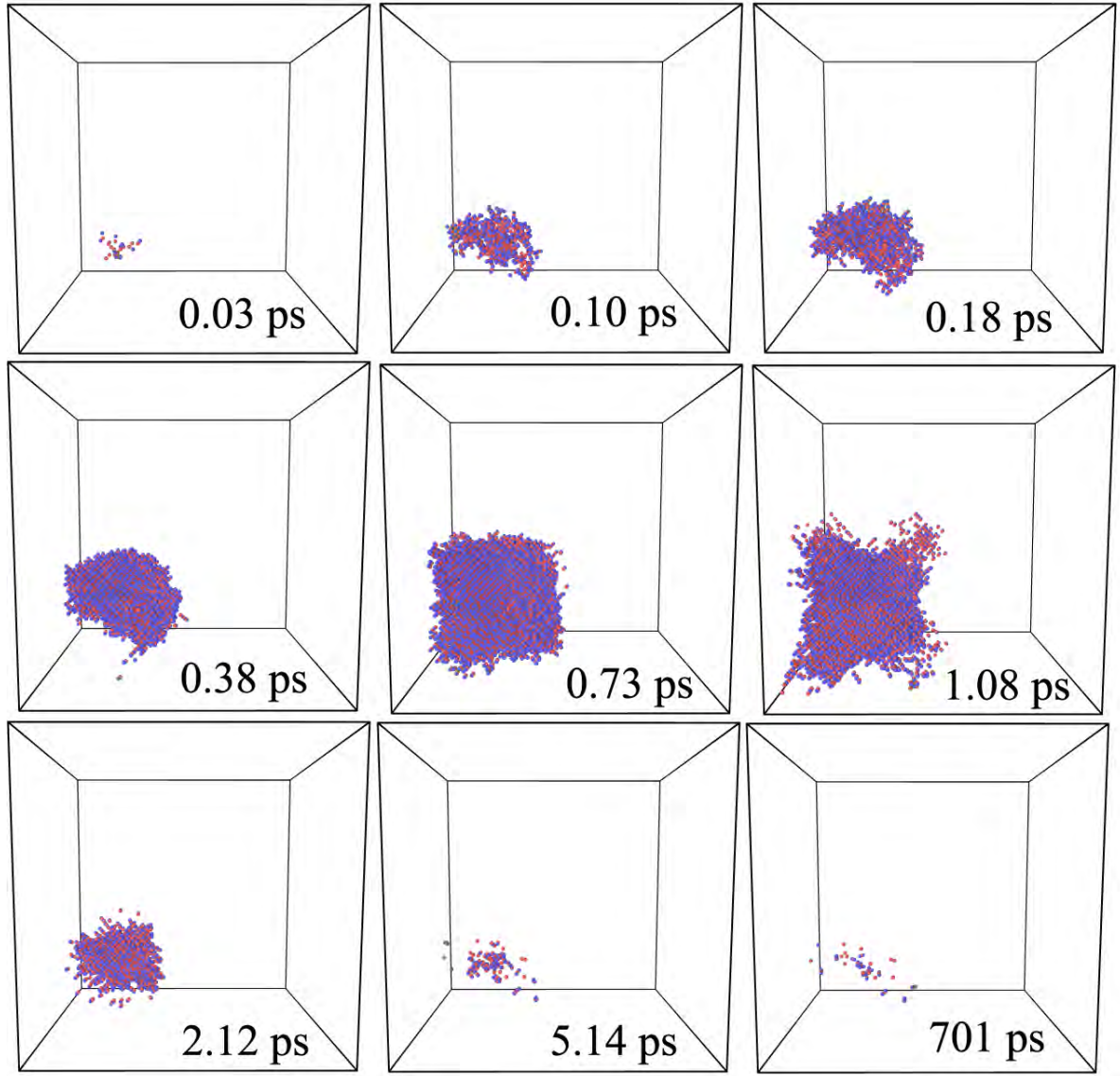


Figure 6. The snapshots of the cascade evolution by a 5 keV $\langle 111 \rangle$ PKA in the quinary system ($\delta = 0.03$) at different times.

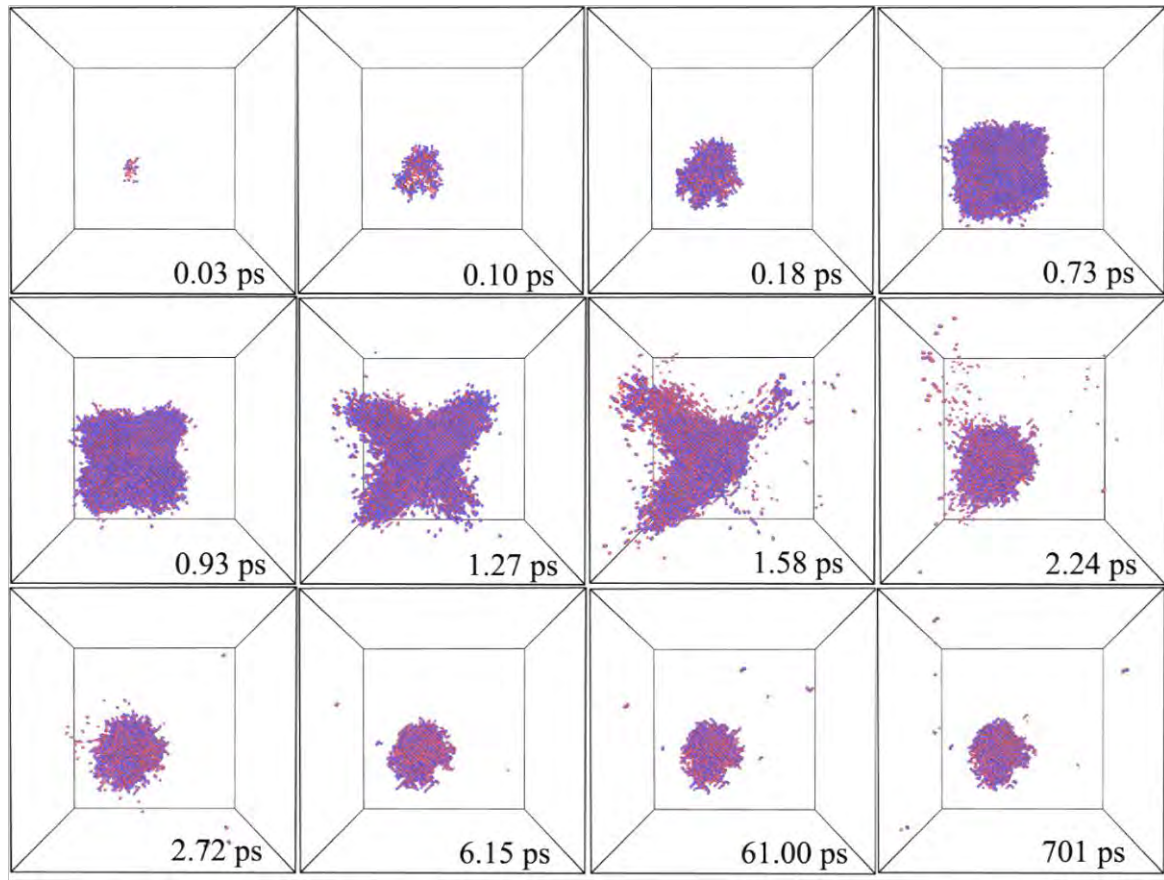


Figure 7. The snapshots of the cascade evolution by a 5 keV $\langle 111 \rangle$ PKA in the quinary system ($\delta = 0.05$) at different times.

Figure 8 shows that the number of displaced atoms N_d changes with time in the three systems for different PKA energy in the $\langle 111 \rangle$ directions. Since the cascades simulation are rather stochastic in term of morphology and the amount of displaced atoms for a specific PKA energy and δ combination, we plot the minimum and maximum N_d cases out of the 5 simulations for each PKA energy. A general fashion of the curves is that the N_d first increases until the peak time t_{peak} as the cascade grows since the PKA initiated, it then decreases as the cascade anneals due to the recombination of the defects. The N_d further stabilizes as the defects evolve in the long run. The second peaks in the $\delta = 0.03$ and 0.05 cases at 5 keV are due to the elastic displaced atoms in the vicinity of the cascade core as they were displaced away more than $0.3a$ (lattice constant) from their perfect lattice sites. Another message from Figure 8 is that N_d increases with the PKA energy, at least during the cascade develop time. This is expected and will be further discussed later.

The average peak time and maximum displaced atom N_d of the simulated cascades are shown in Figure 9 and Figure 10. For the pure iron, t_{peak} ranges from 0.2 to 0.8 ps and the average maximum N_d ranges from about 100 to 5000 for the PKA energy between 0.5 and 5.5 keV. The t_{peak} and the average maximum N_d increase with the recoil energy, and they do not follow any linear fashion in the whole energy range simulated. Moreover, the t_{peak} is slightly larger and the maximum N_d is almost doubled than the previous results [13]. Two reasons may account for the difference. First, as pointed out earlier, the potential used in this work is quite different from the literature. The mJp is much softer in the short range as compared with the ZBL potential, and in the medium range the potential is attractive while the Born-Mayer potential is quite repulsive [13]. The difference in the potential limits the stopping range of the PKAs and increases the amount of displacement of atoms. Second, atoms in the elastically distorted region may be counted as displaced atoms as shown in Figure 6 and Figure 7. These atoms are still residing at the distorted lattice sites rather than being moved to the interstitial positions. This effect is more pronounced at high energies and the elastically displaced atoms contribute a fair portion of the displaced atoms in Figure 10. As pointed out by Calder [42], the D-A method reports the amount of displaced atoms by one order of magnitude more than the W-S approach due to the uneven distortion of the lattice. The D-A method is unbiasedly applied to the different systems in this work, though the quantitative accuracy may be compromised to some extent. It is still acceptable for our demonstration of the atomic size effect on the radiation damage of multicomponent systems.

From Figure 9, at energy below 3 keV, the t_{peak} changes linearly with the recoil energy, and when δ is smaller than 0.03, the increase of t_{peak} with δ is not obvious, and when δ is greater than 0.03, the t_{peak} increases with δ slightly. At energy above 3 keV, there is an obvious transition in t_{peak} . When δ is smaller than 0.03, t_{peak} slows down with the energy increase, while δ is greater than 0.03, t_{peak} increases with the recoil energy drastically. Similar trend also applies to the maximum N_d in Figure 10. The difference is that for recoil energy greater than 3 keV, the maximum N_d seems to increase with δ in all the cases, although with

varying rates. The high rate increases of t_{peak} and N_d at high recoil energy and larger δ are also due to the elastically displaced atoms as explained in the previous paragraph.

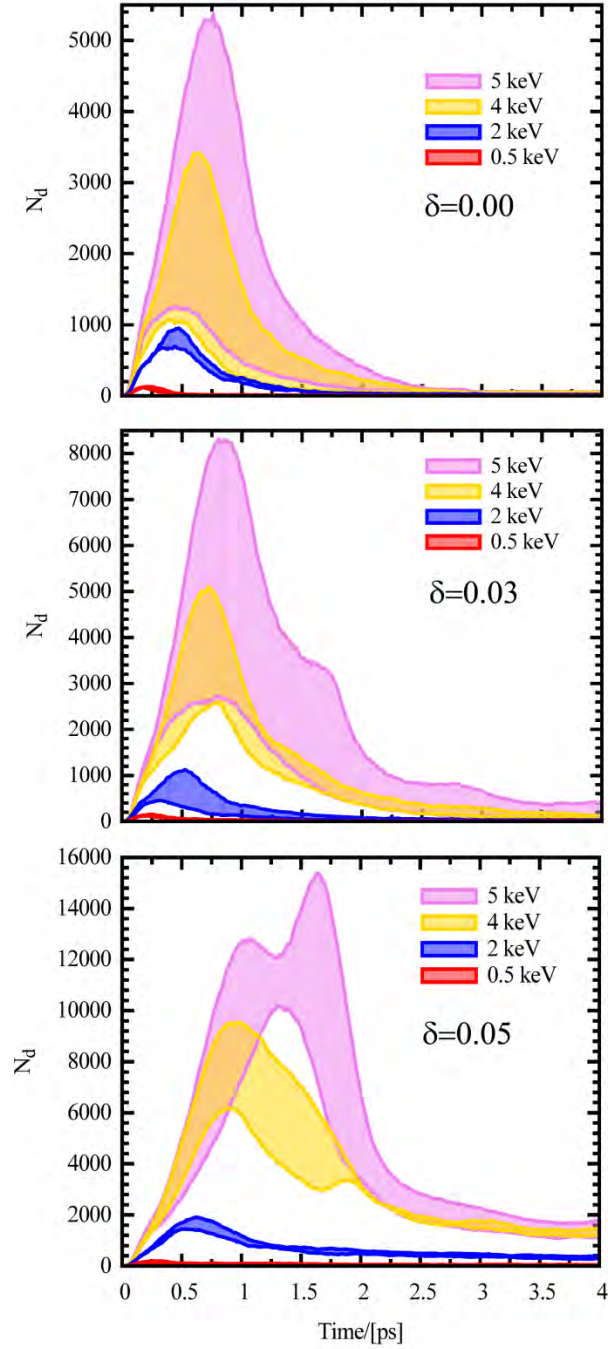


Figure 8. The number of displaced atoms evolutions of cascades by 0.5, 2, 4, and 5 keV $\langle 111 \rangle$ PKAs in three systems with $\delta = 0, 0.03$, and 0.05 , respectively.

Up to now, we provided a general view about how the cascade develops in the multicomponent systems by the characterization with t_{peak} , N_d , and δ as compared with the

pure bcc iron. It is further interesting to understand the effect of alloying on the annealing of the cascades after the peak time. The number of the displaced atoms decreases with time as the defects recombine. The N_d after the peak time can be fitted by an exponential form as [13]:

$$(N_d - N_f) \propto \exp(-t / \tau_d) \quad (1.3)$$

where N_f is the number of final surviving defects, α is the fitting parameter, and τ_d is the relaxation time. Figure 11 shows the average relaxation time of the cascades simulated at different PKA energy for three selected systems with δ equals to 0, 0.03, and 0.05. The error bars are plotted from the standard deviations. In the pure iron system, τ_d increases from 0.13 to 0.35 ps with the recoil energy from 0.5 to 5.5 keV. The τ_d has a sharp increase from 0.5 to 1 keV, and then slows down the increase till 5 keV. The shape of the curve is slightly different from the previous results [13] due to the potential difference. When δ changes to 0.03, τ_d increases ~ 0.05 to 0.12 ps as compared with values for the pure iron systems at each recoil energy. As δ further increases to 0.05, τ_d increases significantly at energy below 4 keV and slightly decreases at 5 keV. The fluctuation of the mean τ_d with recoil energy in the $\delta = 0.05$ system is rather large that τ_d does not follow any linear or exponential relationship with the recoil energy, and is also quite distinct from the pure iron and $\delta = 0.03$ cases. This is due to the higher local strain and instability of the lattice. In all, the high values of τ_d indicate slow annealing of the cascades in the elastically displaced regions. It should be noted that τ_d is not equal to the duration from the peak time to the instance that the cascades are fully relaxed and the defects are stabilized, as can be compared with Figure 8 and Figure 9. Thus, τ_d can be viewed as a characteristic time for the cascade annealing.

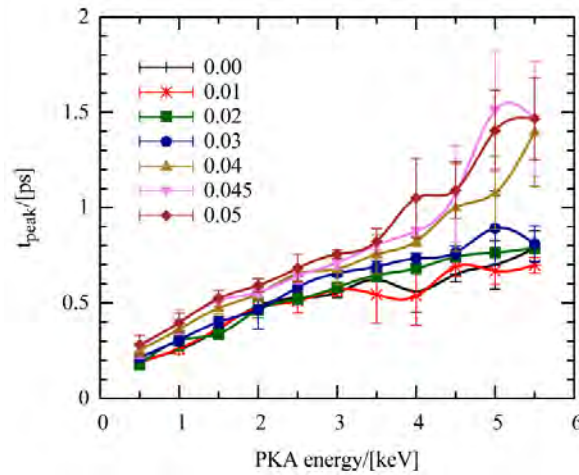


Figure 9. The average peak time of the cascades in the simulated cascades.

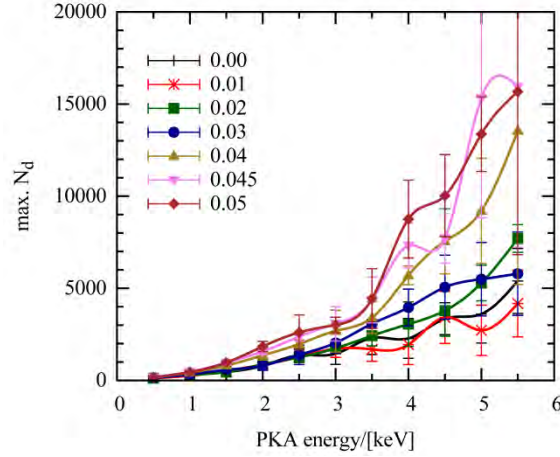


Figure 10. The average maximum number of displaced atoms of cascades initiated by different PKA energy in the $\langle 111 \rangle$ direction for the pure iron and 6 quinary systems.

The cascade simulations are terminated at about 700 ps after initiation. Note that this is a fairly long time for the defects to evolve as assured by the damped fluctuations in the number of displaced atom vs. time logs. The number of defects after cascades is an important parameter to evaluate the radiation damage in alloys. Figure 12 shows the average number of surviving defects in the six systems with 0.5 - 5.5 keV PKAs in the $\langle 111 \rangle$ directions. Here, the 'surviving defects' is used to refer to the Frenkel pairs and does not differentiate the single vacancies, the dumbbell and crowdion interstitials, or clusters of any type. The error bars are plotted according to the minimum and maximum values of each data set. The NRT model is also plotted as a reference using the threshold energy $E_d = 41$ eV as in the pure iron. Generally, the defect number increases with the recoil energy as expected in each quinary system. However, the main features of Figure 12 are two folded. When δ is smaller than 0.04, the defect number is of the order of the NRT values. Specific comparisons is illustrated in Figure 13 in terms of the cascade efficiency factor k , as defined by $k = 2N_d E_d / T$. It is obvious that at PKA energy below 1.5 keV, k is greater than the NRT value 0.8 in the quinary systems when δ is 0.01 - 0.03, while at higher energy, k is slightly smaller than 0.8, ranging from 0.5 - 0.8. This agrees with previous results [13] and seems to be a general phenomenon despite of differences in potentials and crystal structures [45] since the thermal spike ensuing the cascades aids the relaxation of the Frenkel pairs. The detail difference in the values of k may link to the cascade structure and other properties determining the ease of the cascade annealing. When δ is larger than 0.04, the number of surviving defects far exceeding the NRT values is found, and is strongly dependent on the specific system, for example, the atomic size mismatch factor. For system with $\delta = 0.04$, the number of defects fluctuates around at 1.5 times of NRT model value, or the $k = 1.2$. When δ further increases to 0.045, the defect number increases exponentially, with the k value changes from 2 to 5 within the energy range simulated. More conspicuously, the k value increases from 6 to 21 in the system when $\delta = 0.05$. The large number of the surviving defects is also confirmed by the large volume of

amorphous region after the cascade annealing as shown in Figure 7.

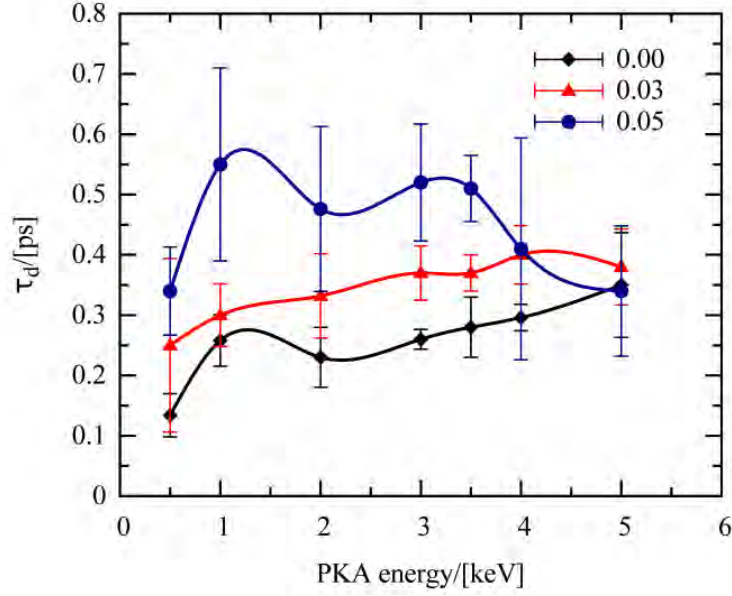


Figure 11. The average relaxation time of cascades by $\langle 111 \rangle$ PKAs with different energy in three systems.

Previously, using the NRT model to predict the number of defects obtained from molecular dynamics has never been successful. The introduction of the cascade efficiency factor k has well explained the origin of this problem. An alternative model proposed by Bacon [46] used an exponential function

$$N_F = A(E_p)^m \quad (1.4)$$

whereas, A and m are fitting parameters. This model has been satisfactory to fit the relationship between the number of defects and the recoil energy (in keV) in Fe, Cu, Ti, Zr, and Ni₃Al at energy below 10 keV [46]. The values of A and m are around 5.7 and 0.77 for Fe and the values for other metals and alloys do not change significantly. However, the application of this exponential relation to our current results is unsuccessful. Using the fitting parameters A and m from the previous studies, the calculated values are still smaller than the simulated values for pure iron. It further fails to fit the results of the alloyed systems with larger δ with the fixed A and m . It was feasible to fit the same exponential form using A and m as variables, but the values are too far away from the published results. Since Eq. 4 serves as a universal empirical accounting with specific A and m , and the physical explanation is still unknown, it is prudent not to put further its applications to the current results; it simply does not apply for the current cases.

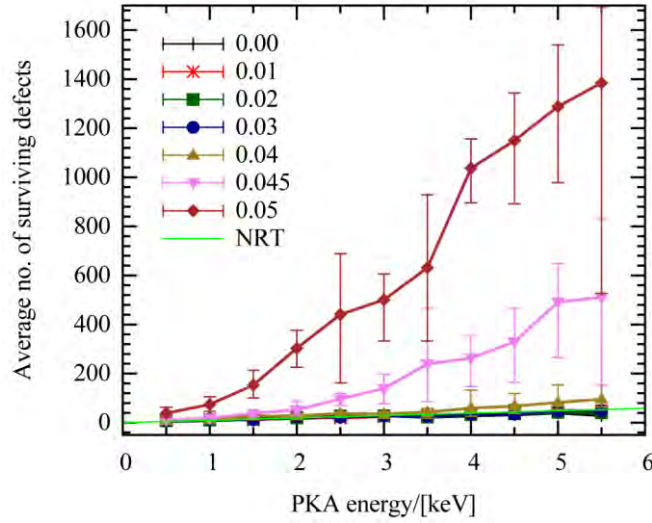


Figure 12. The average number of surviving defects vs. $\langle 111 \rangle$ PKA energy in quinary systems with different atomic size mismatch factors δ , which ranges from 0-5%. The NRT model (Eq. 6-1) is used as a guide to the eyes, the E_d used here is 41 eV.

1.3.3. Discussion

Through the results from Figure 4 to Figure 13, we have demonstrated the huge variations in the radiation behaviors among the multicomponent systems with different atomic size mismatch. The cascade morphology, cascade peak and relaxation times, and the surviving defect clusters and their numbers, in all, undergo major transitions as we tune the atomic size mismatch and the potentials of the systems. Our calculations show that the atomic level strain in the quinary systems prior to the cascades doubled or tripled when the atomic size mismatch factor δ increases from 0 to 0.05. However, there is no obvious correlation between the surviving defects and the atomic level strain since the magnitude of surviving defect change with δ is by several orders of magnitude greater than the change of atomic level strain. But there is a clear point that as the local strain of the crystal increases, the propensity of crystalline to amorphous transition by irradiation becomes higher.

Several limitations should be noted here. First, the pair potential used in the simulations are rather soft as compared with the ZBL universal potential in the short range. In this case, the amount of the displaced atoms is higher in the current work if compared with previous results. The potential effect is more pronounced in the higher energy cascade simulations. For example, when the PKA energy exceeds 3.5 keV, the amount of displaced atom is larger than that in hard potentials, and the volume of elastic deformation also increase in larger δ systems. It was popular to use the ZBL potential for the cascades simulations in the short range. However, our initial attempt of connecting the mJp with the ZBL potential at short range failed due to the strong repulsion in the large δ quinary systems that a perfect crystalline cannot be stabilized. Scaling the connected potential for larger atom makes the repulsive

force too strong in the first nearest neighbor shells. To illustrate the atomic size effect by our scaling approach, a potential soft enough is necessary. In this case, the radiation damage really depends on the potential chosen.

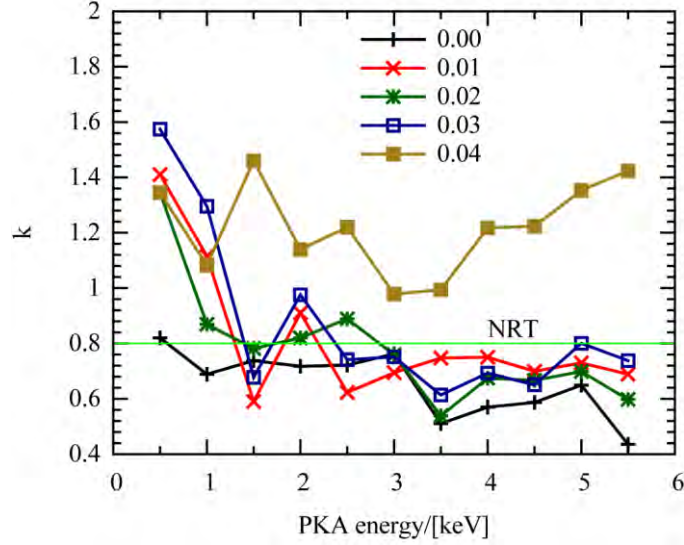


Figure 13. The cascade efficiency factor k for the cascades simulated in the 5 quinary systems with $\delta \leq 0.04$.

Second, as we scale the potential energy according to the atomic size in the random quinary system, the potential energy of an atom fluctuates depending its type and neighbors. Consequently, the formation energy of defects can be affected. Our calculations show that the fluctuation of this energy is rather high. For example, the vacancy formation energy (VFE) of iron atom at 300 K can change from 1.37 eV in pure system to as high as 2.88 eV and as low as -1.05 eV in $\delta = 0.05$ quinary systems. Negative VFE is not uncommon in our observations in the quinary systems, simply because the lattice is so distorted that removing one atom from the lattice site helps stabilizing the local environment. Consequently, the defect generation in the locally distorted lattice sites can be very easy. The stochastic defect production further makes the lattice more susceptible to the damage. In this case, it is reasonable to observe the exceeding number of defects in the severe distorted system such as δ greater than 0.04 systems. However, it is pointed out that the VFE in pair potentials may not be properly evaluated when significant local atomic density occurs [47]. It can be corrected if the embedded energy from the electron densities can be included. Thus, great caution should be exercised when comparing the current results with data from many body potentials and EAM potentials in monatomic systems.

Third, the current simulation assumes the infinite substitution solid solutions in all the quinary systems. The crystalline lattices are built and equilibrated at 300 K. Thus the local

distortion may be rather high due to the constraint of the phonon dispersion at such a low temperature. However, this may not happen in real alloys because the local distortion by the atomic size mismatch may be reduced after melting and crystallization during casting. The local energy from distortion may be released by phase separation, precipitations, dislocations, and grain boundaries. These microstructural defects may be effective sinks to trap defects during irradiations [8, 48, 49]. Experimental studies show that alloys with nanoprecipitates have shown excellent creep and potential radiation resistance due to the high density of sinks [49, 50]. To this end, the current simulations only reports the ideal single phase case in solid solutions.

In all, since our interest mainly focus on the atomic size effect on the radiation damage in solid solutions, the current results have clearly demonstrated the trend of local distortion affecting on the damage. Indeed, we have circumvented several important problems to reduce the computational complexity. We acknowledge that those problems may also play decisive roles in the radiation damage of alloys. Future work is suggested to study these problems.

1.3.4. Summary and Conclusions

Through MD simulations, we have demonstrated the atomic size effect on the radiation damage in quinary alloys for a simple representation of single phased bcc high-entropy alloys. The quinary alloys are modeled by alloying atoms with different atomic sizes and potentials. Results show that:

1. The melting temperature of the systems decreases with atomic size mismatch factor δ , this is related to the lattice distortion and potential energy increase with δ .
2. The cascade morphology changes with the PKA energy and the atomic size mismatch. The elastic deformation region increases with the atomic size mismatch, and further affect the displaced atom peak time and number. The high local strain further affect the annealing of the cascades by leaving clusters of defects in large δ systems.
3. The relaxation time τ_d of the cascades increases with δ . For small δ systems, τ_d increases with the PKA energy, while in systems with large δ , the τ_d fluctuates more remarkably. The increase of τ_d is due to the slow annealing of the systems by the large local distortion.
4. The number surviving defects is close to the NRT model values in small δ systems. When δ is larger than 0.04, the number of surviving defects is orders of magnitude larger than the NRT model. This reflects the huge susceptibility to defect in severe distorted system.
5. For our purpose of demonstration, the current simulations use scaled pair potentials which is rather soft in the short range to represent the force field. The results are proved to be potential and atomic size dependent, and the results in some quinary cases are quite distinct from previous results in monatomic systems. Limitations of the current work should be noted when comparing with previous results.

1.4. Recrystallization in Quinary Systems

Previously, we have demonstrated the radiation damage through cascades in multicomponent alloys. The high temperature core in the cascade body induces local melting as indicated by the defect clustering and the crystalline to amorphous transitions in different systems. It is therefore interesting to investigate the recrystallization property in the multicomponent alloys. More specifically, how does alloying affect the recrystallization? This is of great importance since the mobility and the recombination of the Frenkel defects are affected by the local temperature rise. Accordingly, the relaxation time of the cascades and the surviving defect numbers are always connected to the recrystallization of the melting zone as the energy is dissipated during the thermal spike. The results of this effect have been discussed in the previous section. In this section, we will discuss and compare the recrystallization process in multicomponent systems in a less complicated but more general circumstance where the cascade behaviors is out of consideration.

Since the local melting in the cascade region is caged in the crystalline matrix, the nucleation of the melting zone can be assumed to happen at the liquid and solid interface. In this case, there is no need to consider the nucleation of the liquids after cascades. The main concern of this problem becomes the recrystallization rate in the multicomponent alloys. As we have illustrated before, the volume of the cascade cores are different by the PKA energy and the composition of the system, it is therefore necessary to consider a uniform method to evaluate the recrystallization.

Previously, the melting line of materials was studied to understand the equilibration properties of the liquid and solid phases. The competition of the two phases can be represented by the transformation of the melting lines [51]. For example, the melting temperature can be determined directly by the coexistence method from molecular dynamics simulations with reliable accuracy [52]. It is also feasible to study the recrystallization of metals though the characterization of the phases using proper order parameters [51, 53]. In this section, we adopt this method to study the recrystallization rate in multicomponent alloys.

1.4.1. Simulation Methods

The simulation starts from the equilibration of bcc crystals at certain interested temperature well below the melting point of the system. The system contains 125,000 atoms and the lattice box size is $25 \times 50 \times 50$ unit cells. The NPT ensemble is used to guarantee zero external pressure during the 200 ps equilibration. The crystal part of the coexistence is then saved for later joining. The melting part of system is then obtained separately from heating the crystal part to temperatures slightly above the melting temperate using the NVT ensemble to ensure identical number densities on both sides of the interface. It is then equilibrated for

another 200 ps and then fast quenched to the same temperature as the crystal part to obtain the supercooled liquid or glass state. Afterwards, the crystal part is bisected normal to the Z axis, and the atoms in the upper part is moved to positive Z axis by the length of the box in the Z direction. The quenched part is then sandwiched in between the crystal parts. The system is then relaxed briefly for 40 ps with fixed volume and temperature ensemble. The interface of the two phases are initially flat and the atoms from the two parts may be joined too close. To overcome this, the displacement of the atoms are controlled not to exceed 0.5 Å during the relaxation. Subsequently, the system is further equilibrated with the NVT ensemble for 1.2 ns for data collection.

1.4.2. Results

Figure 14a shows a typical configuration of the simulation box after joining the crystalline and supercooled liquid parts. The crystalline and the amorphous phases have clear and straight interfaces. The interfaces gradually migrate as the competing two phases evolve during relaxation. After 36 ps at 1,400 K, the crystalline phase increases their volume and the interfaces move towards the center of the box as shown in Figure 14b.

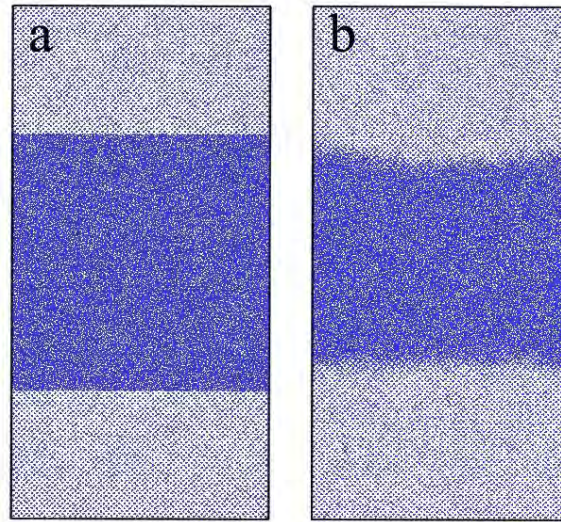


Figure 14. The crystalline-liquid coexistence simulation configuration of the Z-X projection right after joining (a). After relaxation of 36 ps at 1,400 K, the interfaces migrates towards to the center of the box as the volume of the crystalline phase increases, indicating the recrystallization process.

Since we are interested in the recrystallization rate in different systems, it is necessary to obtain the ratio of the two phases during evolution. Here, we follow the method of bond orientational order as introduced by Steinhardt [54]. Particularly, we find that the \hat{W}_6 order parameter is rather useful to distinguish the atoms of icosohedral or bcc phases since the difference is about 12.6 times in the two phases. The icosohedral clustering is popular in

liquids and glasses. Thus, it is feasible to differentiate glass or liquid atoms from the crystalline atoms. Figure 15 shows the atomic position projection in the Z direction with the \hat{W}_6 parameter in a typical simulation. When the two parts of the simulation box are joined together, the clear interfaces in Figure 14a are reflected by the sharp boundaries of the narrow and wide transitions of the \hat{W}_6 parameter. The boundaries are blurred and migrating towards to the center of the simulation box as the recrystallization proceeds. This also agrees with the observations in Figure 14b.

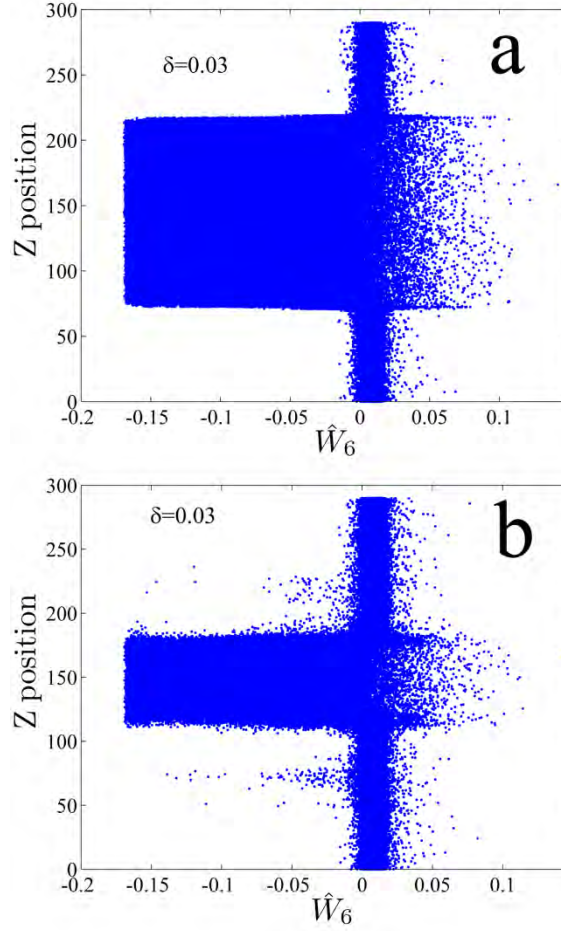


Figure 15. Two examples of the atomic position in Z axis vs. the bond orientational order parameter \hat{W}_6 distribution when joining and after 1.2 ns of relaxation at 900 K.

Here, it is necessary to consider the range of the \hat{W}_6 distributions with temperature. For the perfect bcc lattice, the \hat{W}_6 is strictly 0.0132. As the phonon vibrations with temperature are introduced, the angles between atoms deviate from the observations in perfect lattice. Consequently, the \hat{W}_6 factor also fluctuates. Figure 16 shows the mean values and the

standard deviations of the \hat{W}_6 parameter of atoms in the crystalline system with $\delta = 0.02$ at various temperatures. As the temperature increases, the mean value of \hat{W}_6 decreases from 0.0132 at 300 K to 0.0082 at 1,500 K, and the standard deviation increases from 0 to 0.0077. The changes in the mean and standard deviation with temperatures seem to follow some quadratic polynomials. The reason for the mean value changes is unknown, but the standard deviation change is obviously connected with the phonon vibration amplitude, which also has a second order relationship with the temperature. Compared with the value of -0.1698 in the icosahedral clusters, the mean and the standard deviation are still small. This is also true in systems with larger atomic size mismatch factors. The scatter points outside of the crystalline and the amorphous regions in Figure 15b represents the local defects in the crystalline matrix as the \hat{W}_6 values of the clustering around these atoms are so close to the values for the amorphous state.

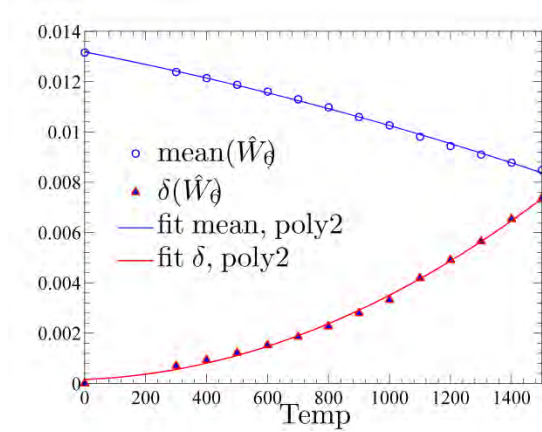


Figure 16. The mean values and the standard deviations of \hat{W}_6 in crystalline lattice with atomic size mismatch factor 0.02 at various temperatures.

Note that the ranges of the two values changing with temperature are indeed far smaller than those in amorphous phase as illustrated in Figure 15. The fitted curves of the mean and the standard deviation with temperature both follow some quadratic polynomials in fashion, consequences of the thermal lattice vibration.

Up to now, we are able to calculate the recrystallization rate of the joining systems at various temperatures. We calculate the number of atoms with the \hat{W}_6 values falling in the range of 95% the minimum and maximum \hat{W}_6 values of relaxed crystalline at corresponding temperatures. These atoms are identified as crystalline atoms. An error associated with this

scheme is that the atoms in the amorphous region with \hat{w}_6 values still in that range are still treated as crystalline. The error in the high temperatures is larger due to the wider range of the \hat{w}_6 factor as the lattice vibration amplitude is larger. In this case, the error is slightly higher for higher temperature simulation. It is the same situation in systems with larger atomic size mismatch factors. However, the amount of atoms contributes to the error is limited, about 5-8% of the total system. The error improves in systems where recrystallization proceeds since the amorphous volume decreases. In all, this method is acceptable for a rough evaluation.

Figure 17 through Figure 20 show the evolution of the fraction of the crystalline atoms for systems simulated with different δ and T . The number of crystallized atoms is N_x and the total number of atoms is N . At the beginning of the simulation, the ratio is around 0.5. In some high temperatures, the ratio is slightly larger due to the error noted before. As shown in Figure 17 for the $\delta = 0.01$, the crystalline atom fraction increases with time due to recrystallization. The slope of this fraction, which is the crystal growth rate, seems to be dependent on the equilibration temperature. The growth rate increases generally with the temperature from 800 K to 1,500 K. It is the same case for $\delta = 0.02$ and 0.03 quinary systems as shown in Figure 18 and Figure 19. The crystal growth rate at 1,400 or 1,500 K is slightly smaller in these systems. The crystalline ratio finally saturates to ~ 0.94 , which is slightly below 1 due to the surviving defects after recrystallization. The major difference in the three systems is that the growth rate decreases with increase in the atomic size mismatch factor at all temperatures. For example, at 800 K, it takes 150 ps to finish the growth in the $\delta = 0.01$ system, while it takes about 2,200 ps in the $\delta = 0.03$ system. The same fashion also applies to the high temperature cases at 1,500 K. The crystal growth rate is calculated and can be explained [55]:

$$u = \frac{k_B T}{3\pi l^2 \eta} [1 - \exp(-\frac{n\Delta G}{k_B T})]. \quad (\text{Eq. 5})$$

Here, l is the average atomic diameter, n is the average atomic volume, η is the viscosity, and ΔG is the free energy difference from melting. Since the simulated temperatures are below the melting, ΔG and η are positive and they decrease with T . Consequently, the growth rate increases with T .

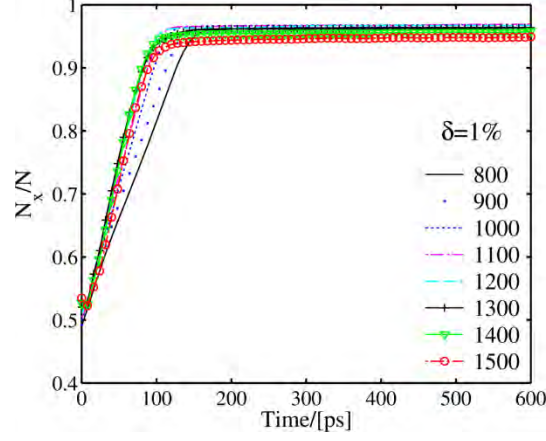


Figure 17. The evolution of the ratio of crystalline atoms N_x in the N atom joining quinary systems when $\delta = 0.01$ at various temperatures. The ratio starts from 0.5 and finally equilibrates to 0.94 due to the surviving structure defects.

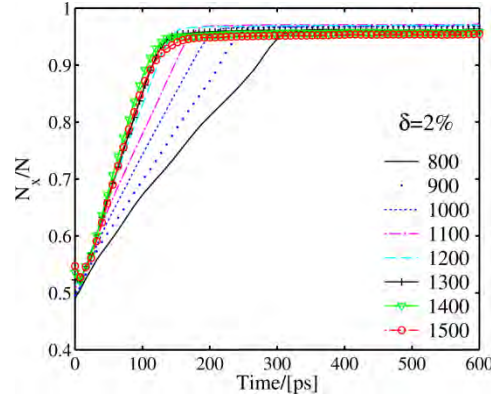


Figure 18. The same evolution of the crystalline atom ratio in the $\delta = 0.02$ quinary systems at various temperatures. Note that the decreasing slopes of the curves before saturation indicate the slower recrystallization speeds.

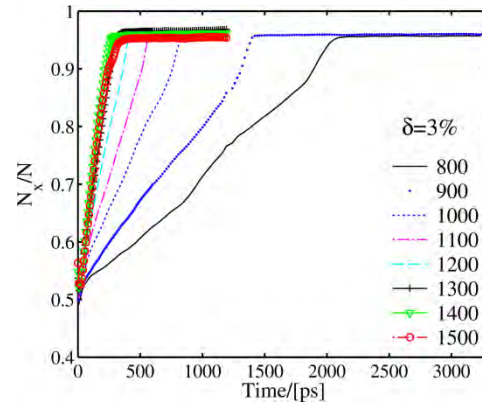


Figure 19. The same evolution of the crystalline atom ratio in the $\delta = 0.03$ quinary systems at various temperatures.

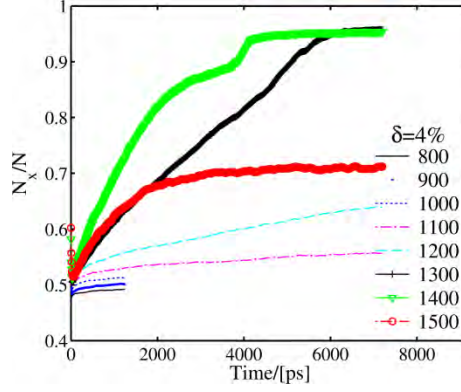


Figure 20. The same evolution of the crystalline atom ratio in the $\delta = 0.04$ quinary systems at various temperatures. Note that at temperatures below 1200 K, the recrystallization is very slow. At 1300 and 1400 K, the recrystallization finishes until 94% of the atoms are bcc. However, at 1500 K, it ceases when $N_x/N = 0.7$.

Figure 20 and Figure 21 show occasions which are different from the previous three systems. In the quinary system with $\delta = 0.04$, at lower temperatures below 1,200 K, the fraction of the crystalline atoms increases very slowly as indicated by the small slope of the curves. The fraction of the crystalline atoms never exceeds 0.65 below 1,200 K. This may due to the low kinetic driving force as the first term of Eq. 5 due to the low temperature and high viscosity. However, as T increases to 1,300 and 1,400 K, the recrystallization finishes until the fraction reaches 0.94 after 6,000 and 4,000 ps, respectively. Note that the amorphous regions are almost fully recrystallized as compared with the small δ systems. As T further increases to 1,500 K, recrystallization almost stagnates when the fraction reaches 0.7. This is suggestive that this temperature is too close to the melting temperature (~ 1600 K as shown in Figure 20) so that driving force is not enough to assist high rate of growth. This also explains the slight decrease in the growth rate at higher temperatures in small δ systems. In the $\delta = 0.05$ system as shown in Figure 21. It is obvious that at lower temperatures below 900 K, there is barely no recrystallization and the crystalline/amorphous interfaces are maintained. When the temperature increases to 1,000 K, the crystalline ratio slowly decreases with time, indicating that the crystalline region is slowly encroached by the supercooled liquid. At high temperatures such as 1,100 and 1,200 K, the ratio of crystalline atoms decreases to 32% and 24%, indicating that about 40% - 50% of the crystalline atoms transformed into glass (amorphization). At temperatures above 1,200 K (not shown here), the amorphization of the crystalline region is rather fast and the thermal vibration magnitude of the crystalline lattice is large due to the lower melting temperature.

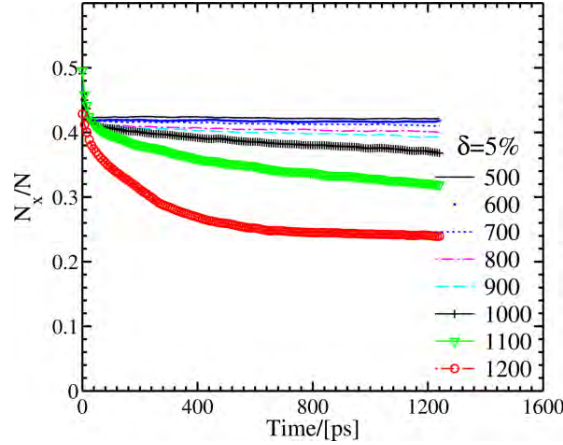


Figure 21. The evolution of the crystalline atom ratio in the $\delta = 0.05$ quinary systems at various temperatures. It is obvious that at lower temperature, there is practically no recrystallization and the crystalline/amorphous interfaces are maintained. When the temperature increases, the amorphous region encroached into the crystalline region slowly. At high temperatures such as 1100 and 1200 K, the ratio of crystalline atoms decreases to 32% and 24%, indicating that about 40% - 50% of the crystalline atoms transformed into glass.

Figure 22 shows the crystal growth rate calculated by the fraction of crystalline atoms per nano second in the five quinary systems simulated. For the atomic size mismatch factor δ smaller than 0.04, the trend is clear that generally by decreasing the atomic size mismatch and increasing the temperature, the recrystallization rate increases. Further increasing δ to 0.05, the recrystallization is impossible in this system and the amorphization takes over due to the instability of the crystalline structure.

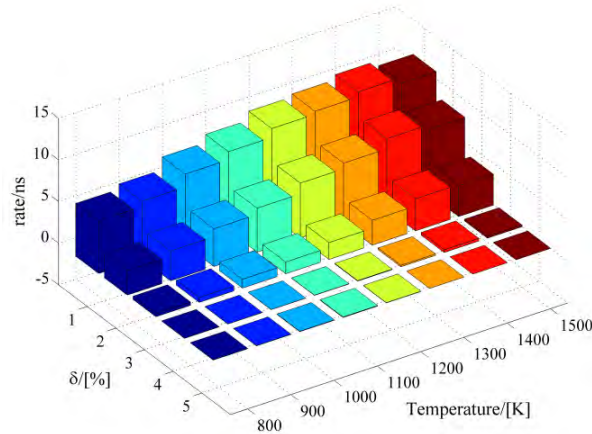


Figure 22. The crystal growth rate in the systems simulated. For atomic size mismatch factor δ smaller than 0.04, the trend is clear that generally by increasing the atomic size mismatch and the temperature, the recrystallization rate increases. Further increasing δ to 0.05, the recrystallization is impossible in this system and the reamorphization takes over due to the instability.

1.4.3. Discussion and Conclusions

Through the two phase coexistence equilibration simulations at difference temperatures below the melting temperature, we are able to determine the crystal growth rate in quinary systems. By combining the results from Figure 17 to Figure 22, we can have a general picture of the atomic size effect on the crystal-amorphous phase transformations as illustrated in the time - temperature - transformation diagram in Figure 23. For monatomic and quinary systems with small δ , the transformation starting and finishing lines of the C curves are close with each other at the upper left region of the plot. This reflects the fast crystal growth rate at higher temperatures. However, as δ increases, the melting temperature and the glass temperature decreases. The C curves move towards the lower right corner of the diagram and the starting and finishing lines are separated further apart from each other reflecting the slow growth rate. The nucleation times of the quinary systems are not studied by the current methods. However, the longer incubation time is safely presumed since the slow growth rate is due to the slow atomic transportation. We also assumed that the critical cooling rate for obtaining the glass structure is slower in large δ systems. This is also confirmed by the cascade results in the previous section that the close cooling rate in the $\delta = 0.05$ system results in having more amorphous atoms.

Through these studies, we now have a semi-quantitative understanding of the atomic size effect on the recrystallization behavior of the multicomponent systems. The TTT diagram can be used to determine the working condition of the multicomponent alloys under radiations. For example, for a given composition, we can estimate the optimal temperature and radiation flux which allow maximum recrystallization. This can also be applied vice versa. Under certain temperature and radiation flux, it suggests the proper atomic size mismatch factor for the composition of the structure alloy to have good rehabilitation after amorphization. Combined with the results of cascades study, we have demonstrated how the atomic size effect plays its role in the radiation damage in structural alloys.

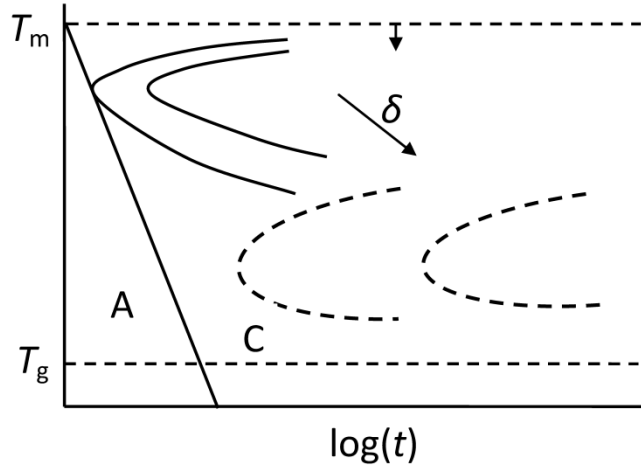


Figure 23. A schematic illustration of the temperature - time - transition (TTT) diagram. The position of the C curves indicating relationship of the waiting time, atomic size mismatch factor, and the critical cooling rate for recrystallization (C region) and stable glasses (A region) in quinary systems.

1.5. First-Principles Calculations of Atomic-Level Stresses

High-entropy alloys involve five or more elements, and it is extremely time-consuming to create interatomic potentials among these components accurate enough to reflect the chemical effects. The problem of interatomic potential can be circumvented by using the first-principles calculations based upon the density functional theory. However, such studies can be performed only for small systems (typically ~ 200 atoms) when the molecular dynamics simulation is required. For this reason in the majority of the research discussed above, we utilized a model potential (a pair-wise potential for iron) scaled to reflect the atomic size effect.

At the same time, we are calculating the atomic level stresses using the first-principles calculation on selected high entropy alloy systems, FeCoNi, FeCoNiCr, CoCrFeNi, and CoCrFeNiAl. The primary purpose of the present research is to separate the atomic size effect from the chemical effect. We already know that the charge transfer plays an effect as large as the atomic size effect in determining the atomic level stresses [39]. But the charge transfer effect can be estimated from the electro-negativity, allowing separation from the atomic size effect. We are using VASP code for generating relaxed structure of 264 atoms of each type. The Locally Self-Consistent Multiple Scattering (LSMS) code in the atomic sphere approximation (ASA), developed at the ORNL, is used to calculate atomic level stresses in these systems. The Jorvik cluster computer at ORNL is used for the computational work. The

results will set the stage for the next step of the research to be conducted in the future.

1.6. Summary and Conclusions

In this task, we have demonstrated the radiation damage and the recrystallization behaviors in multicomponent alloys through molecular dynamics simulations. It was found that by alloying with atoms of different sizes, the atomic level strain increases, and the propensity of radiation induced crystalline to amorphous transition increases as the defects cluster in the cascade body. Recrystallization of the radiation induced supercooled liquid or glass regions show that by tuning the composition and the equilibrium temperature, the multicomponent alloys can be healed. The crystalline-amorphous-crystalline transitions predict the potential high radiation resistance in multicomponent alloys. It is suggested that the development of potentials for multicomponent systems, studies on the radiation in polycrystals of high-entropy alloys are needed to improve the understanding of radiation damages for future structure material development using these alloys.

2. Task 2: Radiation Behavior of HEAs

The objective of the second task is to perform irradiation studies, which will provide the critical understanding and data to validate computational predictions in Task 1, of the HEA behavior under high irradiation doses, such as 100 dpa, at temperatures to 700 °C. The experimental validation is essential to the assessment and development of the materials to be used in next-generation nuclear reactors.

2.1. Introduction

High-entropy alloys (HEAs), proposed by J. W. Yeh in 1995 [56], are novel materials with unique compositions and tailored applications. In contrast to traditional alloy systems, the HEAs are defined as solid solution system with equal or nearly equal atomic-ratios upon five principal elements. The multicomponent HEAs have superior mechanical properties [57] and become potential candidates in extreme environments, which suits for next-generation nuclear systems. Advanced reactor materials are required to operate at higher temperature, more than 700 °C. It is believed that the HEAs are thermal-dynamically stable at elevated temperature due to the higher entropy of mixing that minimizing the driving force, lowering the tendency of oxidation and phase transformation. In addition, equimolar concentrations suppress the atomic diffusion of constituent elements.

HEAs also shows good high temperature strength and fatigue resistance [58, 59]. However, the radiation damages by energetic neutrons are not clear in HEAs. Egami et al. [6] recently discussed that various sizes of solute atoms leads severe lattice distortion and high atomic-level stresses, which can effectively reduce the formation of extended defects. The objective of this present study is to investigate micro-structural evolution under heavy ion irradiation of AlCoCrFeNi and AlCuCrFeNi quinary HEAs. Total three types of HEAs were fabricated and followed by mechanical property measurement. Scanning electron microscope, atomic force microscope, and transmission electron microscope are performed for post-irradiation characterization.

2.2. Experimental Procedure

2.2.1. Materials preparation

AlCoCrFeNi and AlCuCrFeNi quinary HEAs were arc-melted under vacuum and casted into a plate with dimension of 127 x 305 x 19 mm. Three types of as-cast HEAs are Al_{0.1}CoCrFeNi, Al_{0.3}CoCrFeNi, and Al_{0.5}CuCrFeNi₂. The density of the HEAs measured to be 7.11 g/cm³ using Archimedes method. Further heat-treatment were implemented with hot

isostatic pressing (HIP) at elevated temperature. Metal forging technique was also conducted compared to HIP process. The treated plates were then sectioned by electrical discharge machining (EDM) to 18 x 8 x 1.5 mm. Specimens are polished down to micro-meter size alumina till mirror quality prior to the irradiation.

2.2.2. Irradiation condition

The Stopping and Range of Ion in Matter (SRIM) software was used to acquire the damage profile and implanted ion concentration. 5 MeV nickel (Ni) and 10 MeV gold (Au) were selected to study radiation effected in three types of HEAs. Figure 24 shows the dpa vs depth with full-cascade calculation. The peak damage created by 5 MeV Ni and 10 MeV Au are 1.7 μm and 1 μm , respectively. The peak concentration of implanted ions are below 0.4 at%.

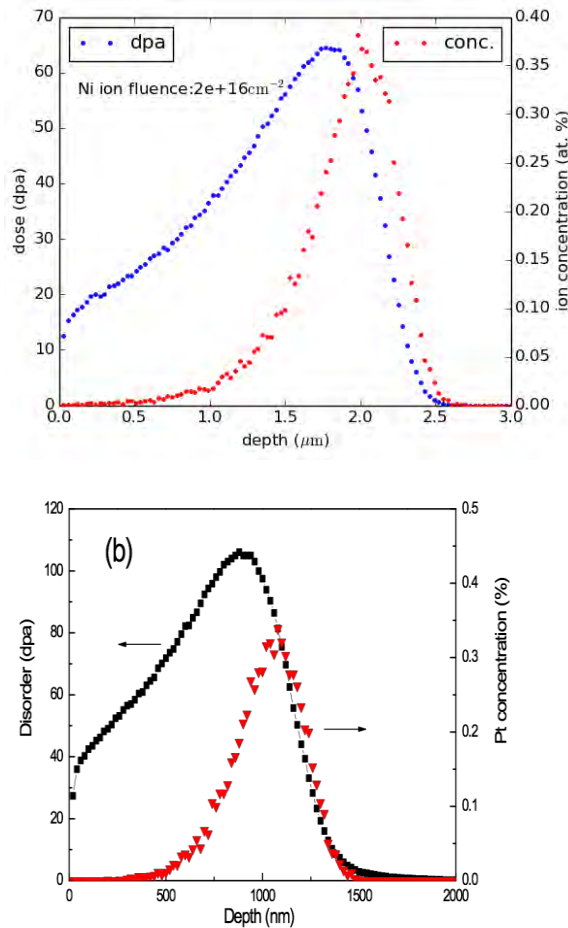


Figure 24. Damage profile of 5 MeV Ni and 10 MeV Au at fluence of $2 \times 10^{16} \text{ ions/cm}^2$.

As for the high temperature irradiation, the thermal couple was clamped onto sample surface and closely monitored throughout the experiment. The temperature fluctuation is less

than 1 °C. Figure 25 shows the experiment setup for the $\text{Al}_{0.3}\text{CoCrFeNi}$, including the irradiation areas of different fluences and temperature control. Each area is larger than 3 x 3 mm, which can be used for further mechanical properties characterization. The masked areas was denoted as reference, which is not irradiated.

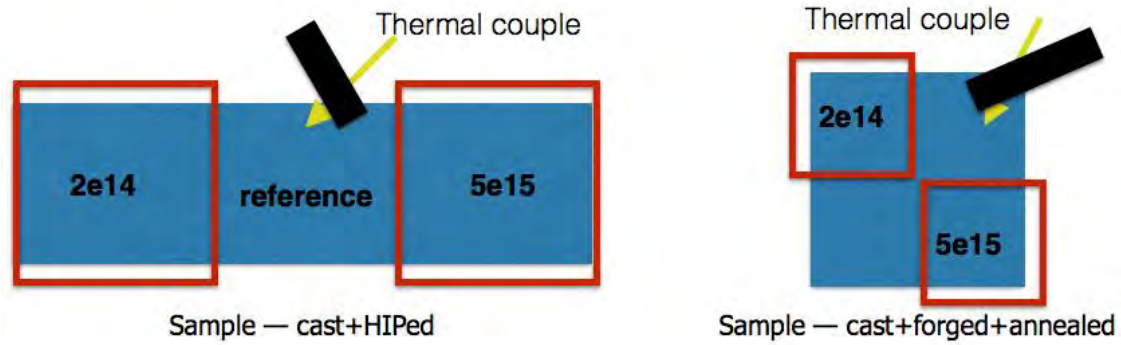


Figure 25. Illustration of irradiation setup and temperature feed-back.

2.3. Characterizations

2.3.1. $\text{Al}_{0.5}\text{CuCrFeNi}_2$

As-cast $\text{Al}_{0.5}\text{CrCuFeNi}_2$ specimens are examined with SEM. Two phases were observed from the polished surface. Figure 26 is the typical SEM image with backscattered detector and energy dispersive spectroscopy (EDS) mapping. The feature with lighter contrast in (a) indicates copper rich phase. In addition, Table 3 summarized the EDS spectra taken from 5 different spots across the matrix and lighter contrast phase. Spot A and B referred to the phase with lighter contrast, and EDS showed enriched copper and aluminum concentration. It suggests that the precipitation may form and separate from the matrix during processing.

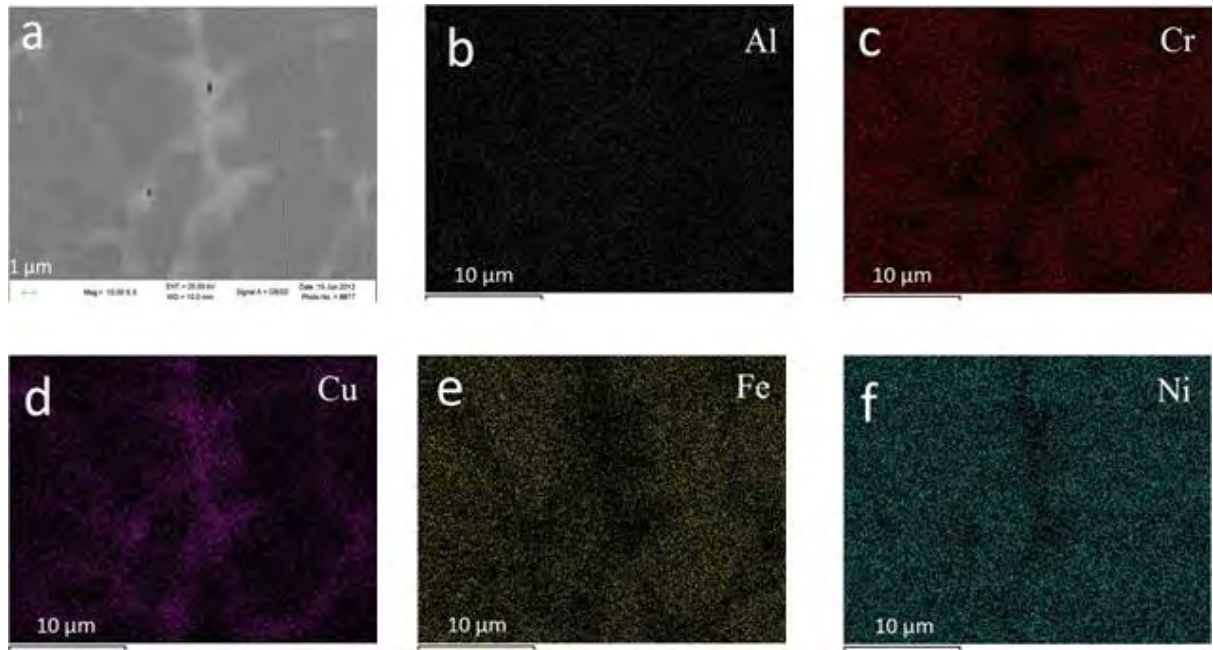


Figure 26. Elemental mapping of the $\text{Al}_{0.5}\text{CuCrFeNi}_2$

Table 3. EDS spectra of element concentration.

Element	Al (at.%)	Cr (at.%)	Cu (at.%)	Fe (at.%)	Ni (at.%)
A	11.22	7.93	55.41	5.79	19.65
B	12.22	7.02	51.20	6.12	23.44
C	9.03	19.41	15.10	18.44	38.02
D	7.57	20.67	12.91	21.21	37.64
E	6.38	20.95	12.19	22.23	38.25

The nanoindentation was performed on $\text{Al}_{0.5}\text{CrCuFeNi}_2$ to study the mechanical properties. The measurement is conducted with Hysitron TriboScope coupleed to a Quesant atomic force microscope (AFM). The indenter for the test is a non-conducting-diamond NorthStar cubic shape with 40 nm tip radius. During the test cycle, the max load is 9000 μN , and five indentation tests were performed to have better statistics. Figure 27 shows the typical graph of loading/unloading curve with penetration depth. For each max load, ten seconds holding time was applied.

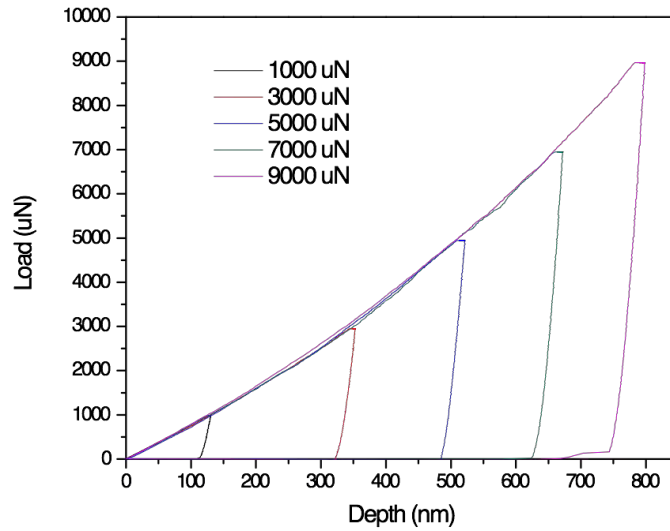


Figure 27. Load-Displacement curves of the Al_{0.5}CuCrFeNi₂

With the help of Oliver–Pharr approach, the reduced contact modulus (E_r) of the Al_{0.5}CrCuFeNi₂ can be calculated using the top portion of unloading curve. The modulus E_r is plotted in Figure 28 with applied loading. The decrease of the reduced contact stiffness with the indentation load was caused by the overall effect of the stress-assisted formation of the excessive free volume and the nucleation and formation of voids.

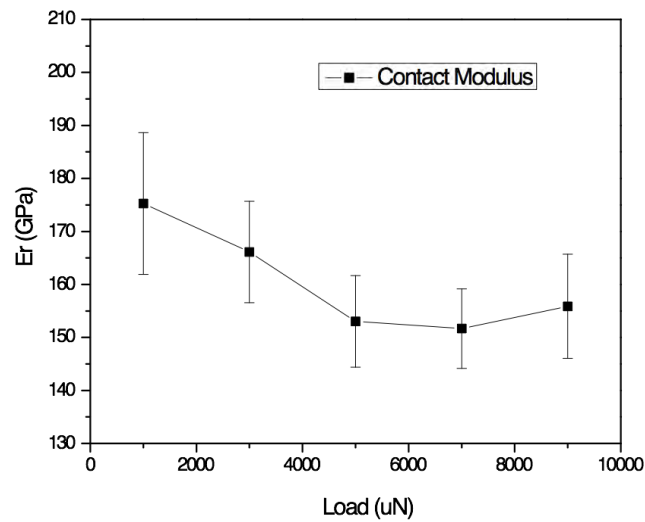


Figure 28. Effect of the indentation load on the reduced contact modulus

Furthermore, the hardness shows the same trend in Figure 29 which decreases with increasing applied load. The excessive free volume as generated during the indentation increases with an increase in the indentation load, and the plastic deformation zone increases with the indentation load. Even though more excessive free volume is

nucleated during the indentation, the specific growth rate of the plastic zone is higher than the specific nucleation rate of excessive free volume. This leads to a decrease in the average concentration of the excessive free volume.

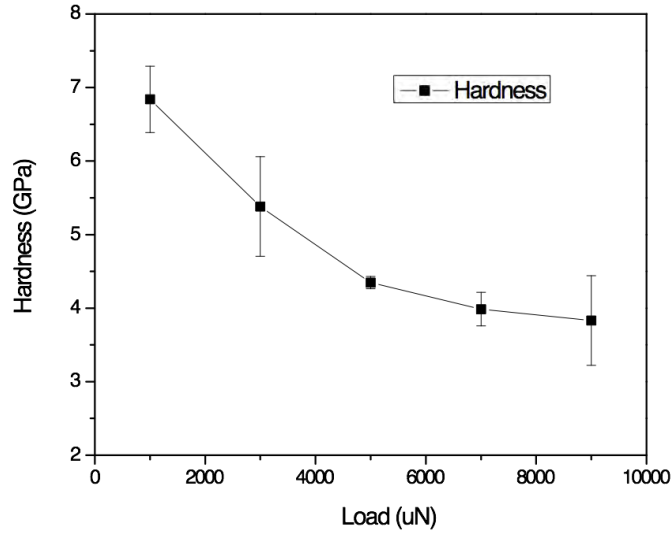


Figure 29. Dependence of the indentation hardness on applied load.

2.3.2. Al_{0.1}CoCrFeNi

As-cast Al_{0.1}CoCrFeNi specimen has undergone hot isostatic pressing (HIP) process at 1,477 K and 100 MPa for 4 hours. High purity argon was flowing during the heat treatment. After HIP process, the specimen was cool down to 615 K in 3 hours and further down to 500 K in 1 hour. X-ray diffraction (XRD) was performed on seven polished HIP specimen. Figure 30 shows the typical 2-theta scan spectra. It is worth noting that some of the HEAs possess nano-crystalline or even amorphous structure due to the size of the solute and possible nucleation rate differences. However, some distinguishable peaks can be identified as face-centered cubic (FCC) structure [(111) $2\theta = 43.8169^\circ$, (002) $2\theta = 51.0013^\circ$, (022) $2\theta = 75.0394^\circ$]. With known d-spacing, the lattice parameter $a = 3.57 \text{ \AA}$ can be calculated. In addition, SAD patterns were acquired from TEM analysis to confirm the crystal structure. Figure 31 shows typical electron diffraction patterns of the FCC crystal structure along the [110] zone axis.

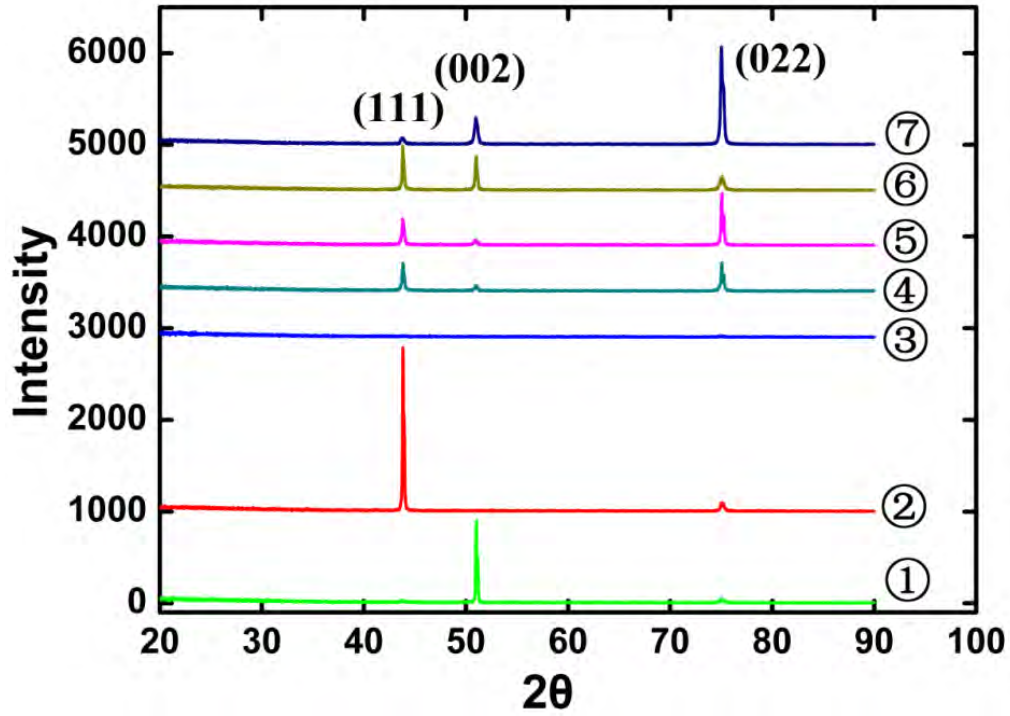


Figure 30. The XRD 2-theta scan of the Al_{0.1}CoCrFeNi HEA.

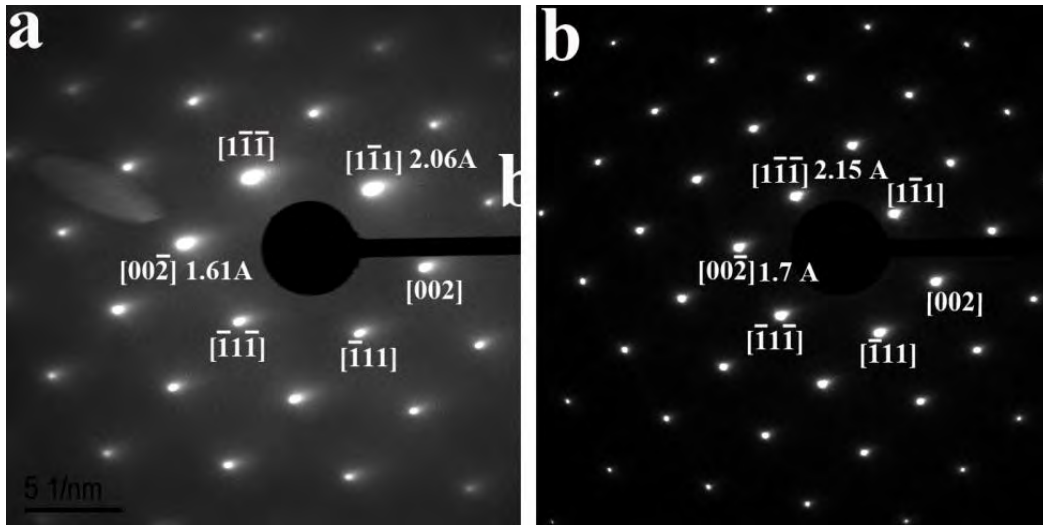


Figure 31. The electron diffraction of as-HIP Al_{0.1}CoCrFeNi taken with (a) selected area aperture and (b) condense aperture.

The first objective of the heavy ion irradiation is to study the swelling resistance by using AFM to measure the volume changes before and after irradiation. Each Al_{0.1}CoCrFeNi specimens were masked to have the reference as un-irradiated area. The as-HIP Al_{0.1}CoCrFeNi specimens were then irradiated with 10 MeV Au ions to the fluences of (1) 1

$\times 10^{14}$ ions/cm², (2) 1×10^{15} ions/cm², (3) 5×10^{15} ions/cm², and (4) 1×10^{16} ions/cm², and the corresponding peak damage level are 1.34 (H1), 13.4(H2), 67(H3) and 134(H4) dpa, respectively. The temperature during the irradiation was monitored and recored as 80 °C. The dose rate was 7.4×10^{10} Ion·cm⁻²·s⁻¹, and the peak Au concentration is 0.26 % based on SRIM calculation. Figure 32 shows the AFM images taken from the irradiated specimens, which half of the surface was masked as reference. The H1 with the lowest fluence is not shown here cause no difference was observed. There is a clear boundary and color contrast between irradiated region and masked region. In order to measure the height difference, multiple line scan across the boundary were performed to have better statistics.

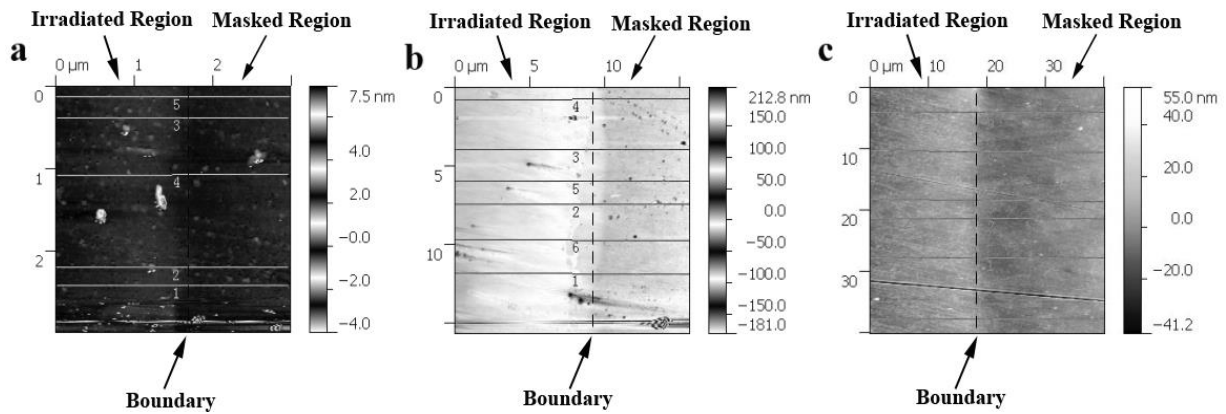


Figure 32. The AFM images of Al_{0.1}CoCrFeNi specimen after 10 MeV Au irradiation (a) H2, 13.4 dpa, (b) H3, 67 dpa and (c) H4, 134 dpa.

The height difference measurements are plotted in Figure 33. The red lines are drawn to fit the real surface and guide the height subtraction between irradiated and masked surface. The measured Δh of H2, H3, and H4 are 4.05 nm, 13.36 nm, and 23.45 nm, respectively. Furthermore, the volume swelling can be calculated with the ion projected range at approximately 2 μ m below the surface. Figure 34 shows the volume swelling changes as a function of dpa throughout the ion projected range, including peak dpa and average dpa. The peak swelling of Al_{0.1}CoCrFeNi HEAs is 1.2% at 70 dpa (average). The swelling rate is quite low compared to Austenitic steel which is 1% dpa.

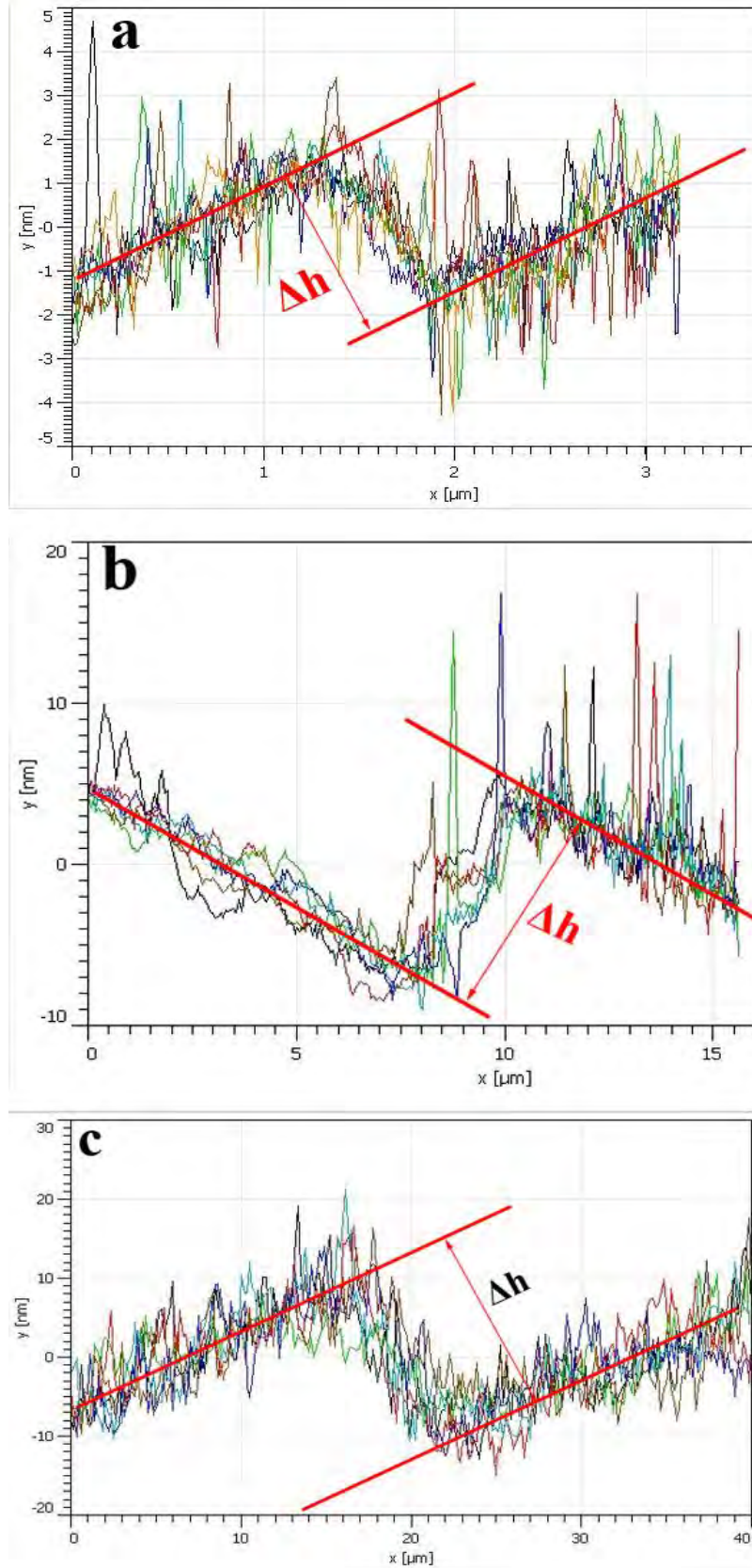


Figure 33. The depth profile of line scans across the boundary (a) H2, 13.4 dpa, (b) H3, 67 dpa and (c) H4, 134 dpa.

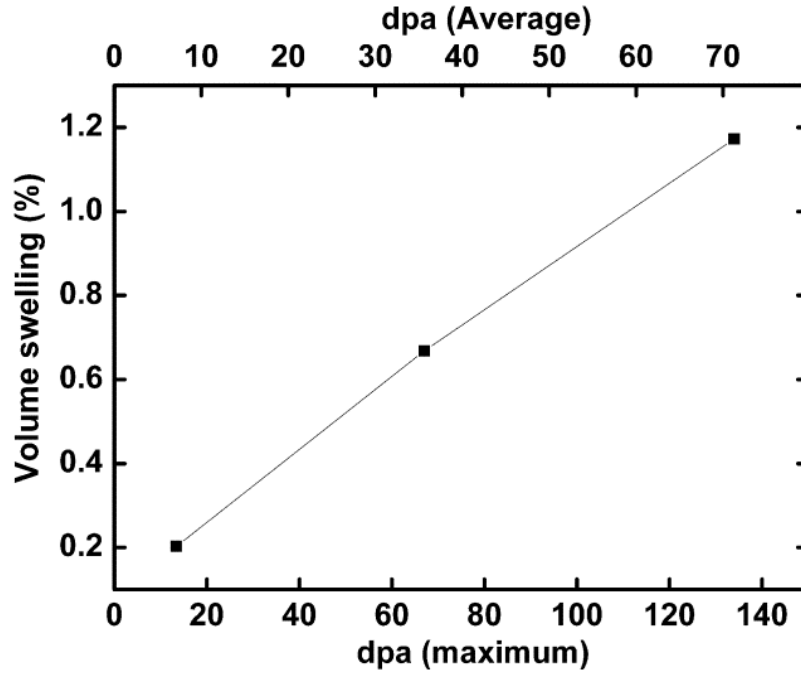


Figure 34. The evolution of volume swelling as a function of dpa

Cross-sectional TEM analysis were performed on the Au irradiated $\text{Al}_{0.1}\text{CoCrFeNi}$ specimen with fluence 1×10^{16} ions/cm². No clear evidence show the voids or dislocations due to the sample thickness. However, SAD patterns revealed the microstructural changes. Figure 35 is the typical BF TEM image with red line denoted to the true surface. Five SAD patterns were taken at different depth below the surface at (1) 500 nm, (2) 1000 nm, (3) 1500 nm, (4) 2000 nm, and (5) 2500 nm. Based on SRIM calculation the peak damage of 10 MeV Au locates at 1 μm and the SAD patterns shows the ring-like structure in Figure 36. The irradiation-induced amorphization was observed throughout ion projected range (including 1, 2, 3, and 4). Area 1 and 2 shows fully amorphized structure and mixed amorphous/ crystalline structure at deeper depth. Area 5 is beyond the ion projected range which remains FCC structure.

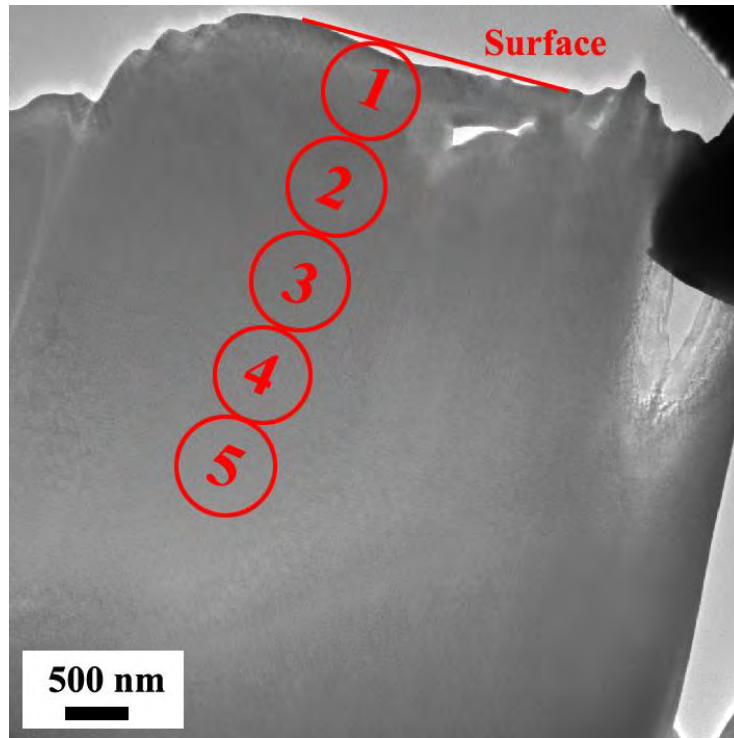


Figure 35. BF TEM of Au irradiated $\text{Al}_{0.1}\text{CoCrFeNi}$ specimen with fluence 1×10^{16} ions/cm². Five SAD patterns were taken as numbered.



Figure 36. The SAD patterns along [110] zone axis at different depth.

2.3.3. $\text{Al}_{0.3}\text{CoCrFeNi}$

Two sets of $\text{Al}_{0.3}\text{CoCrFeNi}$ HEAs samples are selected for the irradiation study. The first set of $\text{Al}_{0.3}\text{CoCrFeNi}$ HEAs has gone through hot isostatic pressing (HIP) after cast process. The second set of $\text{Al}_{0.3}\text{CoCrFeNi}$ HEAs is forged and followed by additional annealing. Both as-received samples possess single face-centered cubic (FCC) structure. According to Electron backscatter diffraction analysis (EBSD), the grain size of as-HIPed samples and as-forged samples are around 500 μm and 50 μm , respectively.

The experiments were carried out at University of Tennessee ion beam materials

laboratory (IBML). Two sets of samples (HIPed and forged) were irradiated with 5 MeV Ni ions at room temperature and 400 °C. Four different fluences of 2×10^{14} , 1×10^{15} , 2×10^{15} , 2×10^{16} ions/cm² were performed at both temperatures. The Stopping and Range of Ions in Matter (SRIM) is used to obtain damage accumulation in HEAs samples, and it is summarized in Table 4. Both Kinchin-Pease (KP) and full cascades models for displacements per atom (dpa) calculation are reported. Peak damage region is at around 1.7 μ m below the surface and peak concentration of implanted Ni ion is roughly 0.35 at. %. The damage rate was kept at 9×10^{-3} dpa/sec.

Table 4. Fluence, peak dpa, and experiment time used of 5 MeV nickel irradiation.

Fluence (ions/cm ²)	Peak dpa (KP model)	Peak dpa (full cascades)	Peak ion concentration (atomic%)	Implantation time
2e14	0.296	0.647	0.00382	1 min. 12 sec.
1e15	1.48	3.24	0.0191	6 min.
5e15	7.39	16.2	0.0955	30 min.
2e16	29.6	64.7	0.382	2 hr.

Total six samples were irradiated and summarized in Table 5. The first cross-sectional TEM specimen was made from F2, which covers the highest damage accumulation. Cross-sectional specimens for transmission electron microscope (TEM) are prepared using Zeiss Auriga duo-beam focused ion beam (FIB) system. Traditional patterns of lift-out technique were milled away from the point of interest, which covered by 2 μ m thick platinum (Pt) protection strip. Figure 37 shows the snapshot while the lamella before the lift-out. The manipulator will be inserted and transfer the specimen to TEM grid for final polish. Average thickness of TEM specimen is 50 nm. TEM was conducted via ZEISS LIBRA 200 with 200 kV acceleration voltage. Both bright field (BF) TEM and selected-area diffraction pattern (SAD) were carried out for microstructure characterization.

Table 5. Summary of irradiations performed on Al_{0.3}CoCrFeNi samples.

Sample	Processing method	Irradiation temperature (°C)	Fluences (ions/cm ²)
H1	HIP	25 (room temperature)	2e14, 5e15

H2	HIP	25	1e15, 2e16
F1	Forged	25	2e14, 5e15
F2	Forged	25	1e15, 2e16
H3	HIP	400	2e14, 5e15
F3	Forged	400	2e14, 5e15

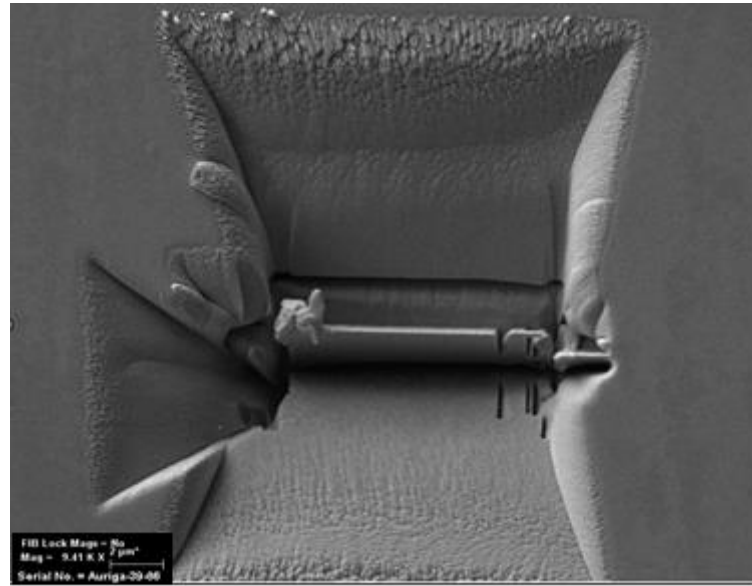


Figure 37. TEM cross-sectional specimen before lift-out

Figure 38(a) shows the traditional BF-TEM image of the F2 irradiated sample after lift-out. The specimen was prepared from the highest fluence area (2×10^{16} ions/cm²), corresponding to roughly 60 dpa at peak. The surface Pt protection layer was milled to achieve thickness of electron transparency. Depth was plotted for guidance. The peak damage region is 1.7 μ m below the surface, based on SRIM calculation. Traditional radiation damages are not observed in the Figure 38(b), including voids or dislocations. The irradiated region remains crystalline and shows no difference compared to bulk (un-irradiated) region. The region beyond the ion projected range is referred as un-irradiated (bulk). Figure 39 shows the close look at depth 1.7 μ m below the surface. The darker contrast is due to the nature of the thin metal foil prepared by FIB lift-out technique. The bending of the specimen can be expected after reach the critical thickness. Besides the stress cause by thinning process, the microstructures retain.

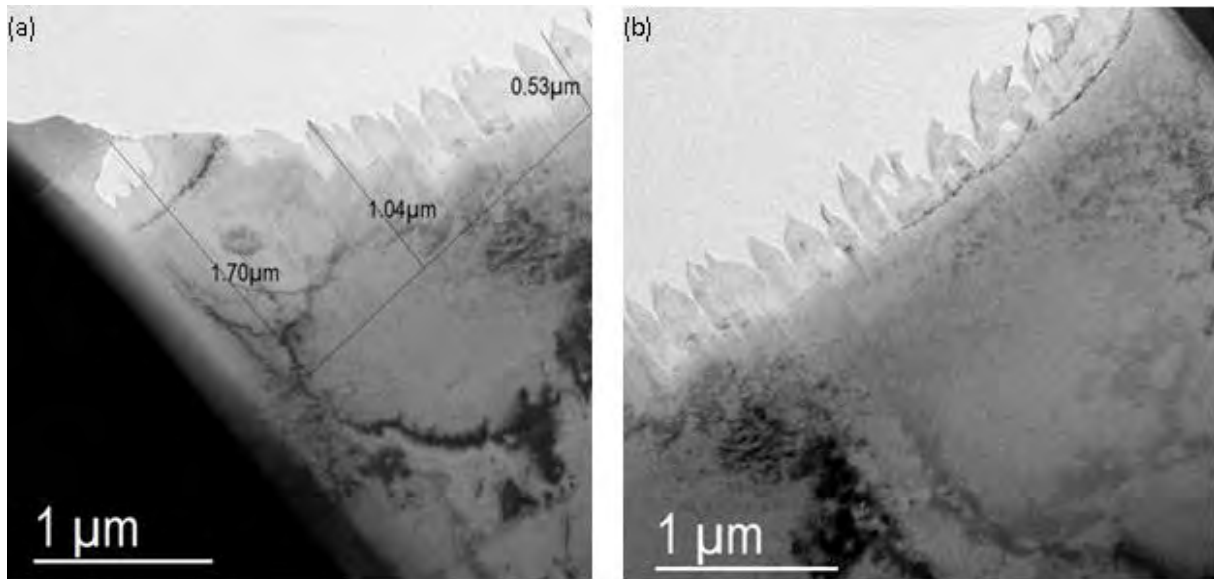


Figure 38. BF TEM images of F2, lift-out from the 2×10^{16} ions/cm². (a) Depth below the surface was marked to guide. (b) Peak damage region with 1.7 um below the surface.

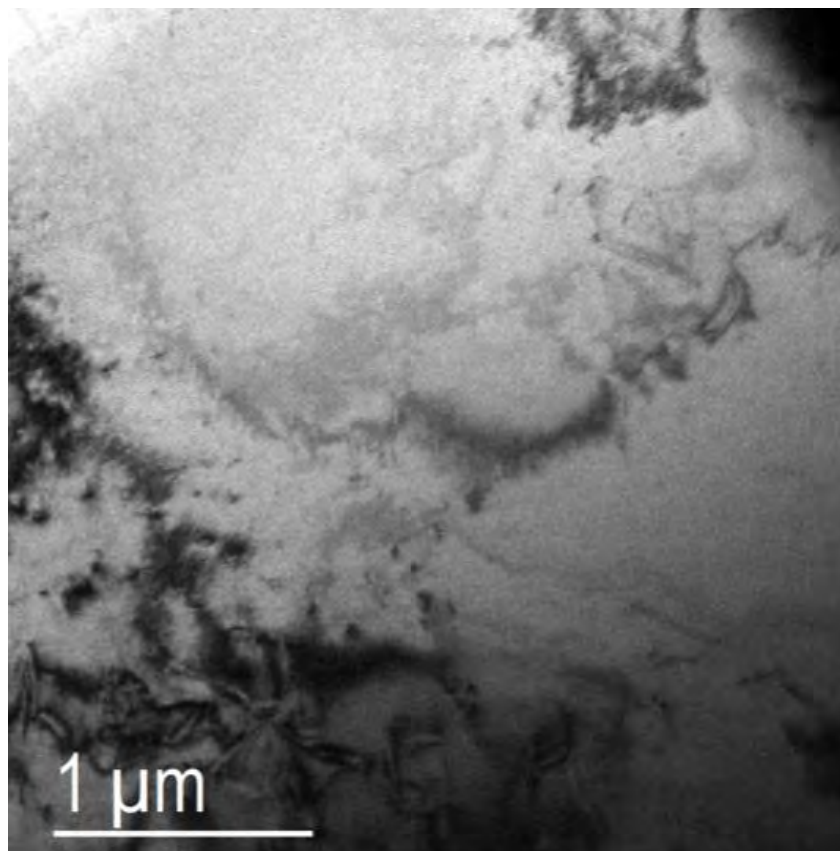


Figure 39. BF TEM images of F2, lift-out from the 2×10^{16} ions/cm².

Further investigation was conducted using SAD patterns to reveal the microstructures. Figure 40(a-b) shows single face-centered cubic crystal structure with [110] and [111] orientation, respectively. It matches with the result from EBSD analysis. In addition, with the help of SAD patterns, the lattice parameter 3.75\AA of the as-forged specimen was obtained. The lattice parameter remains the same in the irradiated region. Same characterization was done of the other fluence in F2. Specimen was lifted out from the 1×10^{15} ions/cm² area. The depth is marked as 1.7 μm for the peak damage region. Figure 41 shows the BF TEM images of F2 with fluence 1×10^{15} ions/cm². No voids or dislocations were observed. The crystal structures remain FCC (SAD patterns not shown here).

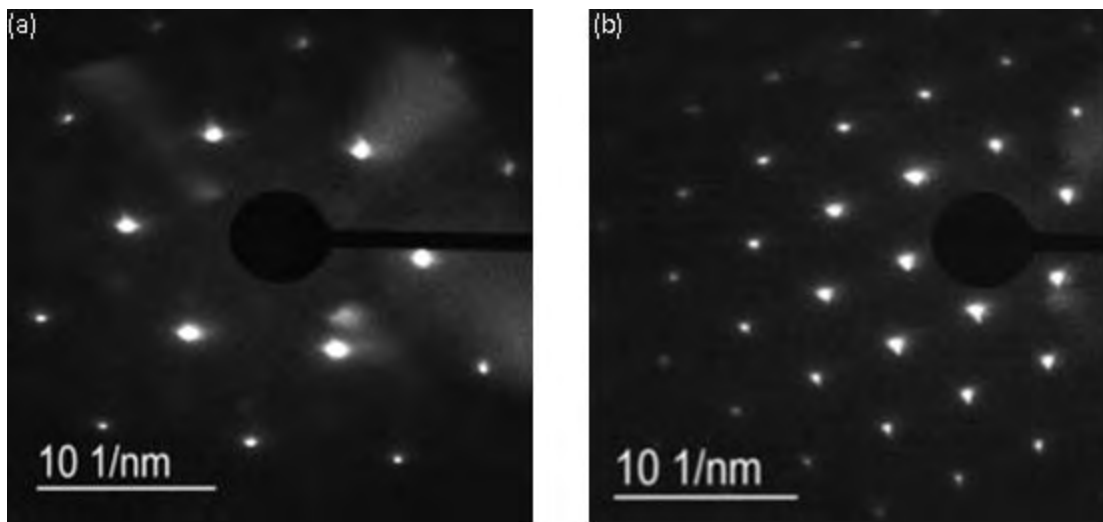


Figure 40. SAD images of F2, lift-out from the 2×10^{16} ions/cm². (a) [110] zone axis. (b) [111] zone axis

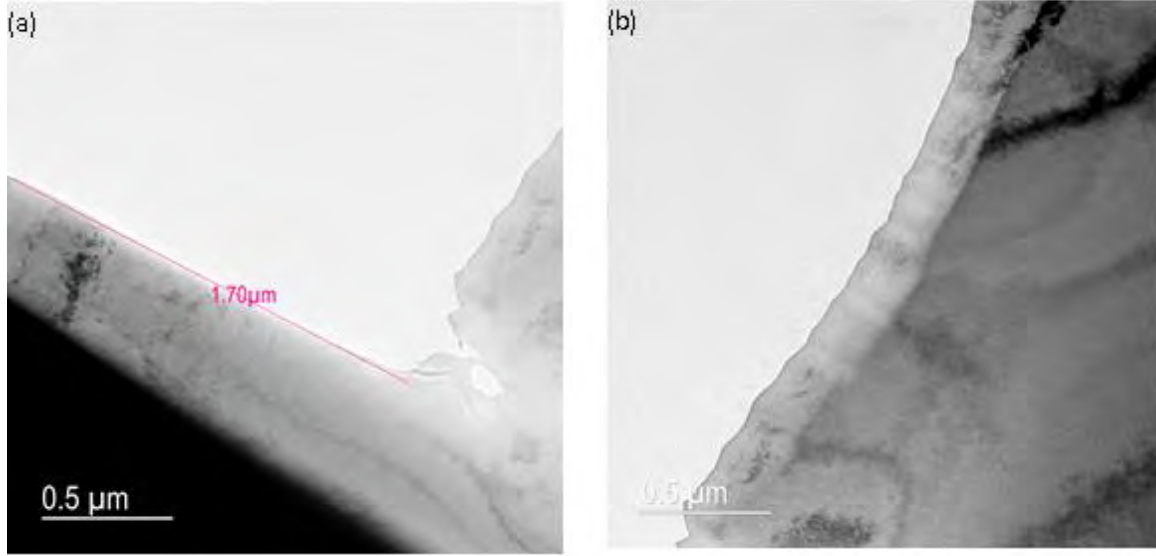


Figure 41. BF TEM images of F2, lift-out from the 1×10^{15} ions/cm². (a) Depth below the surface was marked to guide. (b) Peak damage region with 1.7 μm below the surface.

2.4. Summary and Conclusions

Three types of HEAs were fabricated from AlCoCrFeNi and AlCuCrFeNi quinary alloys. Heat treatment, such as hot isostatic pressing (HIP) process, metal forging and annealing, were applied to strengthen the HEAs. Hardness and reduced contact modulus were measured using nano-indentation test. Heavy ion irradiation were performed using 10 MeV gold and 5 MeV nickel to study radiation effects. Scanning electron microscope (SEM) was conducted for checking the composition and uniformity. Crystal structures of HEAs specimen were identified using X-ray diffraction (XRD) and electron diffraction patterns. Post irradiation analysis were carried out on atomic force microscope (AFM) and transmission electron microscope (TEM).

1. Al_{0.5}CrCuFeNi₂ shows phase separation upon the presence of copper. SEM confirmed the copper-aluminum rich precipitation from the matrix. Nano-indentation was performed to measure reduced contact modulus and hardness. Both hardness and contact modulus show the same trend as increasing applied load, and it indicates that excessive free volume may alter the growth rate of the plastic zone.

2. As-cast Al_{0.1}CoCrFeNi specimen undergone hot isostatic pressing (HIP) process and steady cooling rate which mitigate the quenching effect. X-ray diffraction (XRD) and TEM electron diffraction pattern confirmed the crystal structure to be face-centered cubic (FCC) with lattice parameter 3.57 Å. The heat-treated Al_{0.1}CoCrFeNi was irradiated with 10 MeV Au from 1×10^{14} ions/cm² to 1×10^{16} ions/cm². The swelling behavior was characterized by atomic force microscope (AFM) and swelling rate is approximately

0.02%/ dpa. Cross-sectional TEM reveals the microstructure evolution after Au irradiation. Selected area diffraction (SAD) patterns show irradiation-induced amorphization throughout the ion projected range. Within the peak damage region, amorphous ring is observed and a mixture of amorphous/ crystalline structure at deeper depth.

3. The $\text{Al}_{0.3}\text{CoCrFeNi}$ HEAs shows good radiation resistance up to 60 peak dpa. No voids or dislocations are observed. The crystal structures remain FCC before and after 5 MeV Ni irradiation. Higher dpa might be required to study defects formation mechanism.

3. Task 3: Thermodynamic Calculations and Modeling of HEAs

The objective of the proposed work is to gain critical knowledge of HEAs with potential applications in nuclear reactors and related elevated-temperature and high-pressure systems by combining both theoretical-modeling and focused-experimental endeavors. CompuTherm focused on Task 3 to work on thermodynamic modeling of the Al-Co-Cr-Fe-Ni HEA quinary system using the CALculation of PHase Diagrams (CALPHAD) approach, and the available literature experimental data were used for comparison. It enables us to calculate phase diagrams, which are useful guidelines for the development and processing control of HEAs.

3.1. The CALPHAD Approach

The CALPHAD approach [60] is a phenomenological thermodynamic methodology to obtain a thermodynamic description of a multicomponent system as shown in Figure 42. The term thermodynamic description means that the parameters for the Gibbs energies of all the phases in a system are known. The first step in developing a thermodynamic description of a multicomponent system is to collect thermodynamic and phase equilibrium data of the systems of interest from the literature for the lower-order systems, normally binaries and ternaries. However, if such data are not available, it becomes necessary to first obtain experimentally determined and/or first principles calculated enthalpies as well as experimentally measured phase equilibria for the binaries. The model parameters of the phases involved are obtained in terms of the available data of interest. Care is always taken to be sure that the parameters of these Gibbs energies are physically realistic instead of relying purely on the optimization [61]. This is particularly true when limited data are available. It is noteworthy to point out, once we have the binary descriptions, we can minimize the amount of experimental effort involved for the ternaries. In other words, a preliminary thermodynamic description of this ternary can be obtained from those of its constituent binaries [61]. A preliminary ternary phase diagram of the system in question can be calculated using the estimated thermodynamic description; this calculated phase diagram can be used to identify few key alloys for experimental investigation. In addition, extensive experience has shown that a reliable description of a quaternary system can be obtained from those of the lower order systems except for the cases when a new quaternary phase forms or the range of homogeneity of a particular phase extends to the quaternary compositional space. The CALPHAD approach makes it possible to obtain multi-component phase diagrams not only for basic materials research in related areas such as solidification and solid state transformation but also for alloy design and processing development and improvement. This is especially useful for commercial alloy systems, which are normally multi-component systems and lack of experimental data. Key experiments aiming at giving the maximum amount information can be provided with the aid of the calculated phase diagrams. Thus the

experimental effort is minimized comparing with the approach based on try and error.

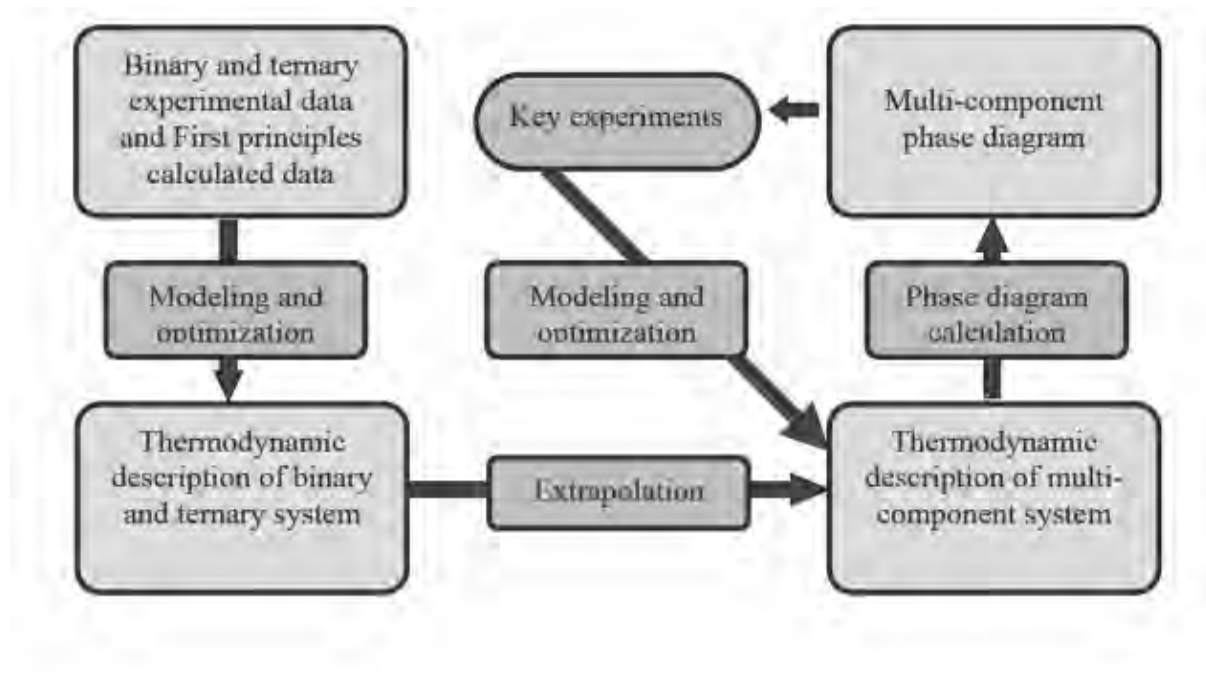


Figure 42. The CALPHAD or phenomenological approach used to obtain a thermodynamic description of a multi-component system.

In order to describe the Gibbs energy of the alloying components and different phases involving in the system, several thermodynamic models are needed:

3.1.1 Elements

The Gibbs energy of the pure element i , with a certain structure, ϕ , referred to the enthalpy of its standard state at 298.15K, is described as a function of temperature by the following equation:

$${}^{\circ}G_i^{\phi}(T) = a + bT + cT \ln T + dT^2 + eT^3 + fT^{-1} + gT^7 + hT^{-9} \quad (3.1)$$

The values of the coefficients $a \dots h$ are taken from Dinsdale [62].

For elements that display a magnetic ordering, such as Ni, an additional term ${}^{mag}G$ is added to the molar Gibbs energy on the right hand side of the formula:

$${}^{mag}G = RT \ln(\beta + 1) f\left(\frac{T}{T^*}\right) \quad (3.2)$$

where T^* is the critical temperature for magnetic ordering, and β the average magnetic moment per atom of the alloy expressed in bohr magnetons. values of the coefficient β and the expression of function f are also taken from Dinsdale [62].

3.1.2. Substitutional Solution Model

The liquid, Fcc_A1 and Bcc_A2 phase were all modeled as substitutional solutions and the molar Gibbs energy is described as:

$$G_m^\varphi = {}^{ref}G_m^\varphi + {}^{id}G_m^\varphi + {}^{ex}G_m^\varphi \quad (3.3)$$

The term ${}^{ref}G_m^\varphi$ defines a surface of reference, which is

$${}^{ref}G_m^\varphi = \sum_i x_i \cdot {}^0G_i^\varphi \quad (3.4)$$

where x_i is the mole fraction of element i , and the quantity ${}^0G_i^\varphi$, molar Gibbs energy of the element i with the structure φ .

The term ${}^{id}G_m^\varphi$ is related to the molar configurational entropy, which is

$${}^{id}G_m^\varphi = RT \sum_i x_i \ln x_i \quad (3.5)$$

and the excess ternary Gibbs energy ${}^{ex}G_m^\varphi$ is

$${}^{ex}G_m^\varphi = x_i x_j L_{i,j}^\varphi + x_i x_k L_{i,k}^\varphi + x_j x_k L_{j,k}^\varphi + x_i x_j x_k L_{i,j,k}^\varphi \quad (3.6)$$

where $L_{i,j}^\varphi$, $L_{i,k}^\varphi$ and $L_{j,k}^\varphi$ are the interaction parameters from the constituent binaries respectively, which can be described by the Redlich-Kister polynomial [63] with temperature dependent coefficients. the ternary interaction parameter $L_{i,j,k}^\varphi$ is:

$$L_{i,j,k}^\varphi = x_i L_i^\varphi + x_j L_j^\varphi + x_k L_k^\varphi \quad (3.7)$$

where L_i^φ , L_j^φ and L_k^φ represent the interaction on the liquidus surface in the three corners of the ternary system, respectively.

3.1.3. Stoichiometric Compound Model

The Gibbs energy of a binary stoichiometric compound $A_p B_q$, G_m^φ , is described as a function of temperature only:

$$G_m^\varphi = \sum_i x_i G_i^{\varphi,0} + \Delta_f G(A_p B_q) \quad (3.8)$$

where x_i is the mole fraction of component i , and $G_i^{\varphi,0}$ represents the Gibbs energy of component i with the φ structure; $\Delta_f G(A_p B_q)$, which is normally a function of temperature, represents the Gibbs energy of formation of the stoichiometric compound. If $\Delta_f G(A_p B_q)$ is a linear function of temperature:

$$\Delta_f G(A_p B_q) = \Delta_f H(A_p B_q) - T \cdot \Delta_f S(A_p B_q) \quad (3.9)$$

then $\Delta_f H(A_p B_q)$, and $\Delta_f S(A_p B_q)$ are the enthalpy and entropy of formation of the stoichiometric compound. Equation (3.8) can be readily extended to a multi-component stoichiometric compound phase.

3.1.4. Compound Energy Formalism (CEF)

An ordered intermediate phase can be described by a variety of sublattice models, such as the compound energy formalism [64-66] and the bond energy model [67, 68]. In these models the Gibbs energy is a function of the sublattice species concentrations and temperature. The Gibbs energy of a binary ordered phase described by a two-sublattice compound energy formalism $(A, B)_p : (A, B)_q$ can be written as:

$$\begin{aligned} G_m^\varphi = & \sum_{i=A,B} \sum_{j=A,B} y_i^I y_j^{II} G_{i,j}^\varphi + RT \left[p \sum_{i=A,B} y_i^I \ln y_i^I + q \sum_{i=A,B} y_i^{II} \ln y_i^{II} \right] \\ & + \sum_{j=A,B} y_A^I y_B^I y_j^{II} \sum_v (y_A^I - y_B^I)^v L_{A,B;j}^v + \sum_{i=A,B} y_i^I y_A^{II} y_B^{II} \sum_v (y_A^{II} - y_B^{II})^v L_{i,A,B}^v \\ & + y_A^I y_B^I y_A^{II} y_B^{II} L_{A,B;A,B} \end{aligned} \quad (3.10)$$

where y_i^I and y_i^{II} are the species concentrations of component i in the first and second sublattices, respectively. The first term on the right hand of the equation represents the reference state with the mechanical mixture of the stable or hypothetical compounds: $A_p B_q$, $B_p A_q$ and B. $G_{i,j}^\varphi$ is the Gibbs energy of the stoichiometric compound $i_p j_q$ with the φ structure. The value of $G_{i,j}^\varphi$ can be obtained experimentally if $i_p j_q$ is a stable compound, or it can be a model parameter obtained by optimization using experimental data related to this phase. Recently, first-principles calculations have also been used to obtain such a value for an unstable $i_p j_q$ compound. The second term is the ideal mixing Gibbs energy which corresponds to the random mixing of species on the first and second sublattice. The last three terms are the excess Gibbs energies of mixing. The “ L ” parameters in these terms are model

parameters whose values are optimized using the experimental phase equilibrium and thermodynamic data. These parameters can be temperature dependent. In this equation, a comma is used to separate species in the same sublattice, whilst a colon is used to separate species belonging to different sublattices. The compound energy formalism can be applied to phases in a multi-component system by considering the interactions from all the constituent binaries. Additional ternary and higher-order interaction terms may also be added to the excess Gibbs energy term.

In order to obtain reasonable and reliable model parameters of the above models, optimization is necessary. The optimization is the processing to ultimately obtain the parameters of the Gibbs energy function of each phase, which will make the thermodynamic description to account for the known experimental data but also able to extrapolate beyond the ranges of temperature and composition where data are available. This is achieved when proper thermodynamic models are used for the phases in question. Needless to say, the broad thermodynamic knowledge of the person who uses the optimization tools also matters. In this study, the optimization was performed using PanOptimizer [69] and all phase diagram calculations were carried out using Pandat [69]. Usually, the following steps were adopted during thermodynamic optimization [70]:

- (a) Collecting and categorizing the thermodynamic and phase equilibrium data. In principle any kind of experimental datum that is explicitly or implicitly linked to Gibbs energy can be used as input for optimization.
- (b) Evaluating the collected data critically for essentially eliminating bad and contradictory data. Critical evaluation requires considerable expertise and some familiarity with different experimental techniques. It is important that one must make a record of details such as the technique used, the phases present, the purity of the samples, the experimental conditions, the quantities measured and their reliability, etc. Frequently, difficulties occur during the optimization primarily due to poorly evaluated experimental data such as contradicting data, theoretically unacceptable data as the inputs!
- (c) Assigning the proper starting values in the computerized thermodynamic optimization of phase diagrams is highly critical. If bad starting values are used for the optimizing variables, the nonlinear equations may not yield any solution. Accordingly, it is more practical to begin the optimization with a 'minimal' data set, comprising only a few vital experimental data. Including too many experimental data in the beginning stage of the optimization may prove unwieldy. In the case of binary systems, for example, it is often sufficient to use a well-defined three-phase invariant phase equilibrium, a congruent transformation, and the enthalpy of formation of the compound undergoing the congruent transformation.

3.2. Thermodynamic Database Development Overview

CompuTherm focused on Task 3 to work on thermodynamic modeling of the Al-Co-Cr-Fe-Ni quinary system using the CALPHAD approach. There are 20 binaries and ternaries constituent sub-systems in total need to be modeled in this work (as listed in Table 6 and Table 7). All 20 constituent lower-order systems have been thermodynamically modeled in this work. The preliminary thermodynamic database of the Al-Co-Cr-Fe-Ni quinary system was then obtained via extrapolation, which enables us to calculate phase diagrams, which are useful guidelines for the development and processing control of the Al-Co-Cr-Fe-Ni HEAs.

Table 6. Constituent binary systems of the Al-Co-Cr-Fe-Ni system

Binary Systems				
Al-Co	Al-Cr	Al-Fe	Al-Ni	Co-Cr
Co-Fe	Co-Ni	Cr-Fe	Cr-Ni	Fe-Ni

Table 7. Constituent ternary systems of the Al-Co-Cr-Fe-Ni system

Ternary Systems				
Al-Co-Cr	Al-Co-Fe	Al-Co-Ni	Al-Cr-Fe	Al-Cr-Ni
Al-Fe-Ni	Co-Cr-Fe	Co-Cr-Ni	Co-Fe-Ni	Cr-Fe-Ni

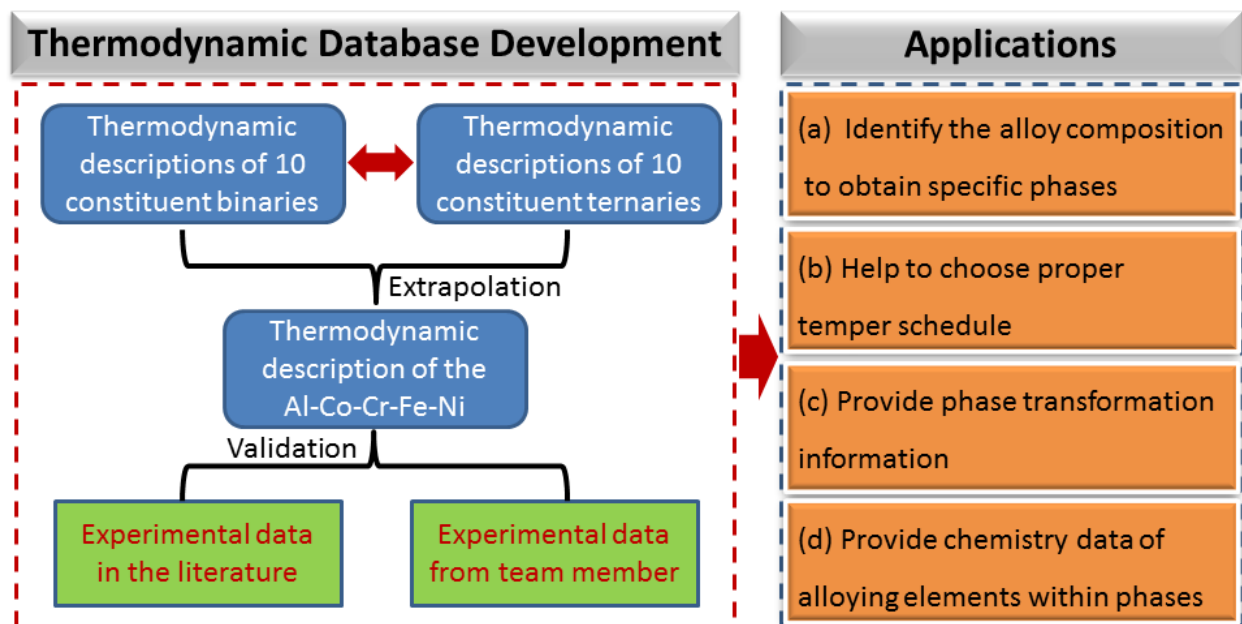


Figure 43. Schematic diagram shows the overview picture of task 3

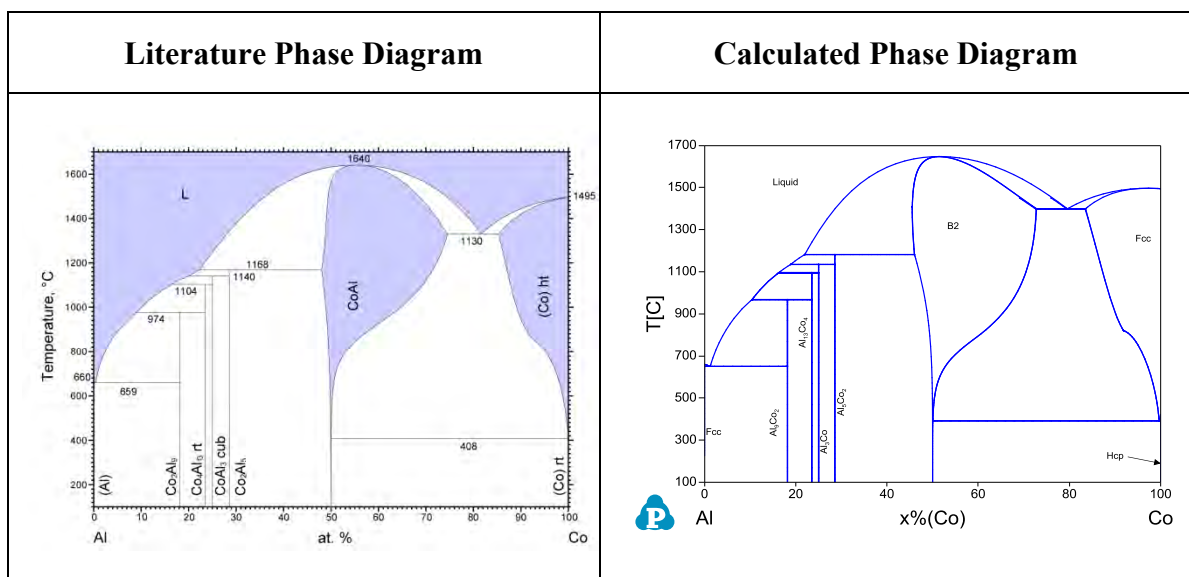
The above diagram shows the overview picture of our task 3. First of all, thermodynamic database of Al-Co-Cr-Fe-Ni quinary system needs to be developed. There are 10 constituent binaries and 10 constituent ternary systems need to be thermodynamically modeled. In order to make the thermodynamic database reliable, experimental data, such as thermo-chemical data, phase-equilibrium data etc., are necessary to validate the developed thermodynamic database. Once the thermodynamic database of the Al-Co-Cr-Fe-Ni quinary system has been developed, we can carry out thermodynamic calculations using the PandatTM software. The following information can be obtained through our thermodynamic calculations: (a) identify the alloy composition in order to obtain specific phases; (b) help to select popper heat-treatment temperatures; (c) provide phase-transformation information during solidification or heat-treatment; (d) provide the alloying element distribution within phases in equilibrium. Currently, the preliminary description of this quinary system has been obtained. Validations using the available experimental data in the literature are in progress. On the basis of the thermodynamic calculations using our current preliminary thermodynamic database, a few HEAs of the Al-Co-Cr-Fe-Ni system were selected for experimental investigation by our team members.

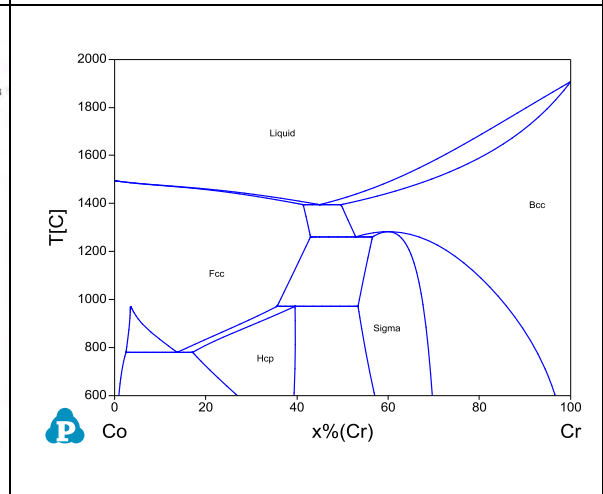
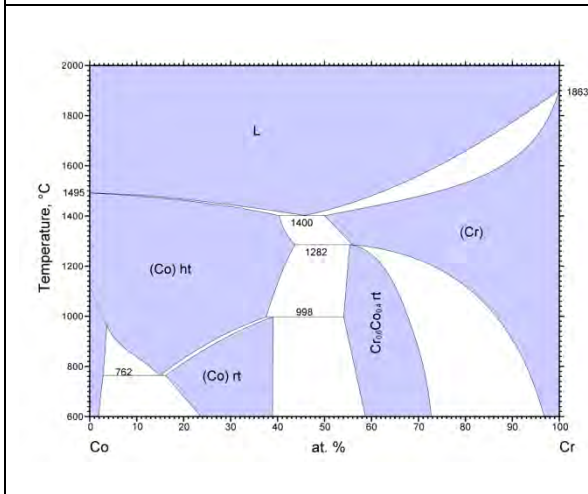
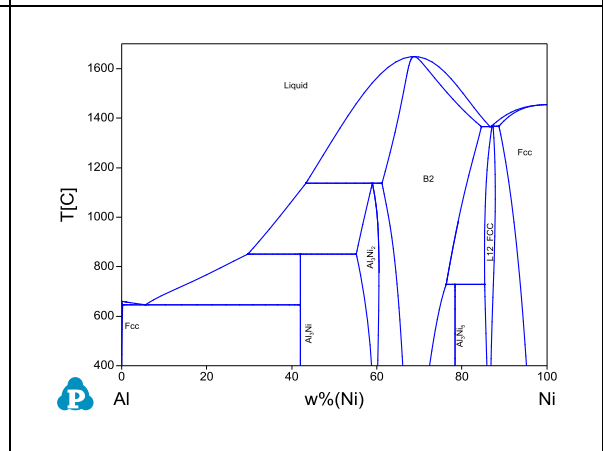
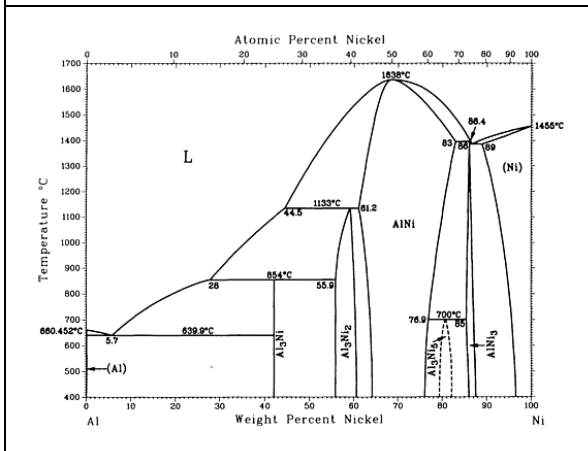
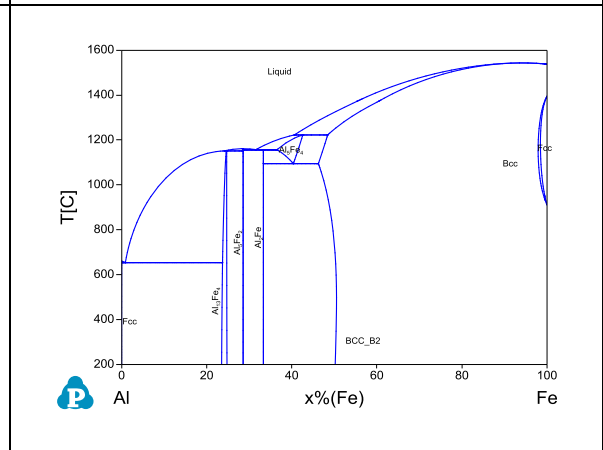
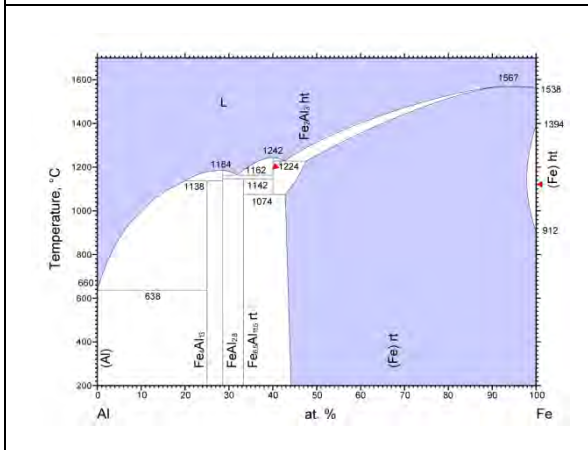
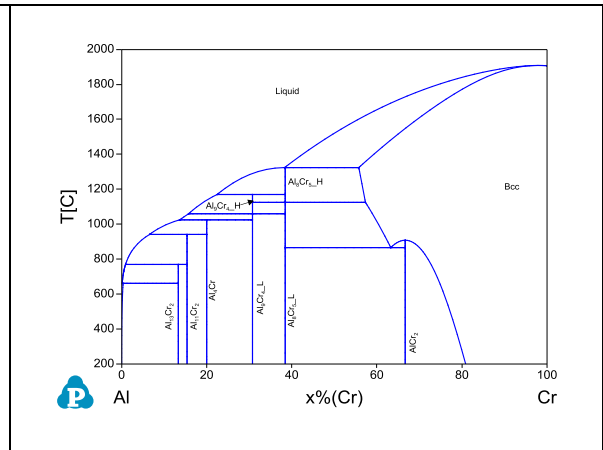
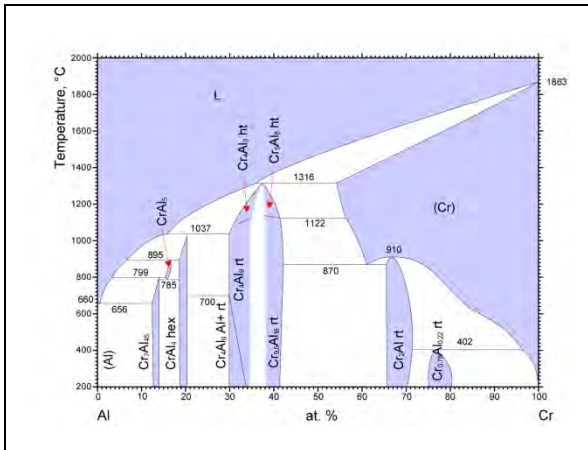
3.3. Experiment and Discussion

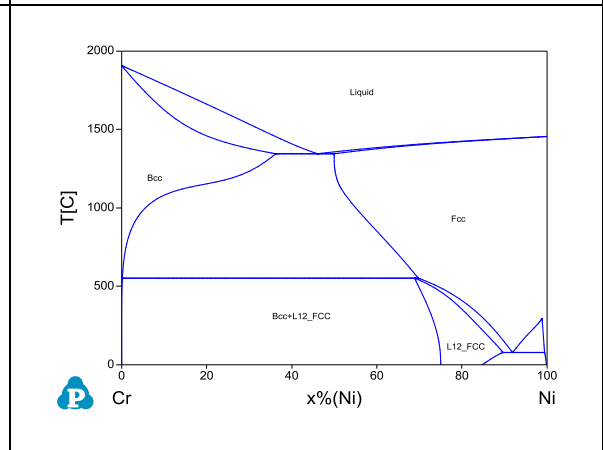
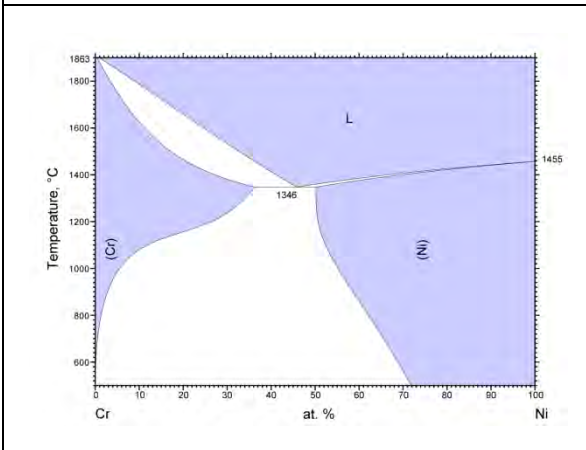
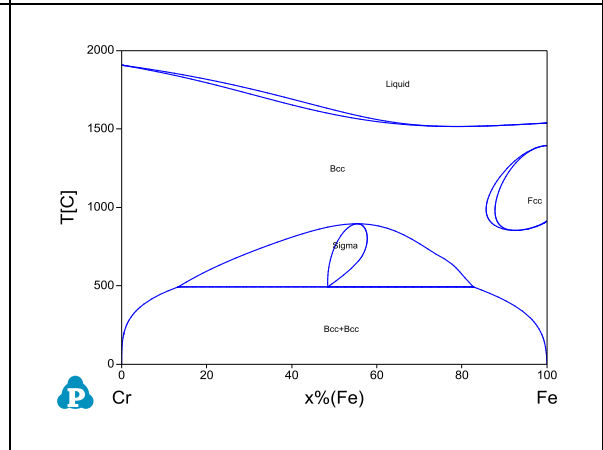
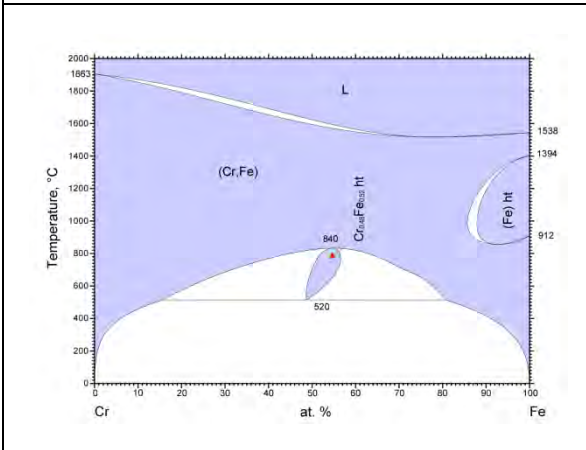
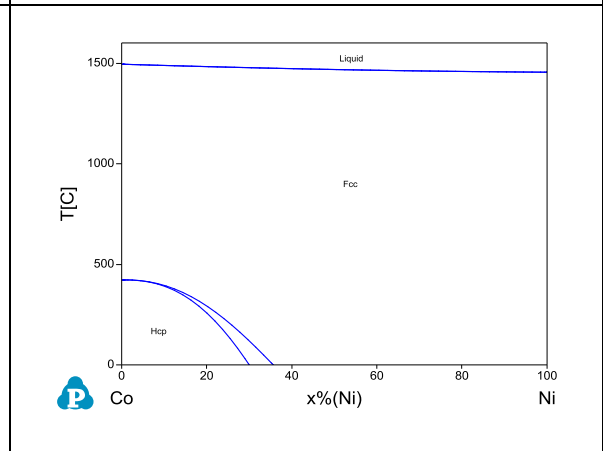
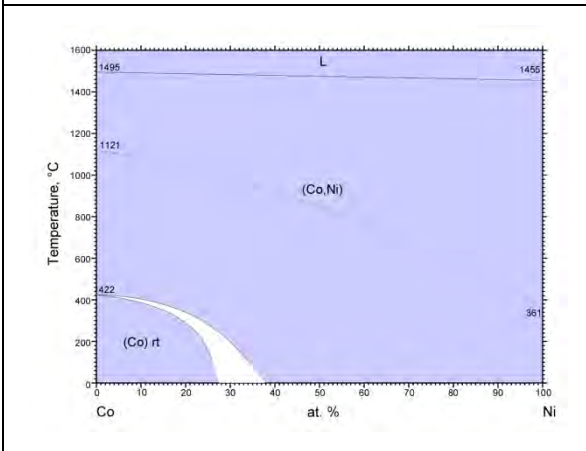
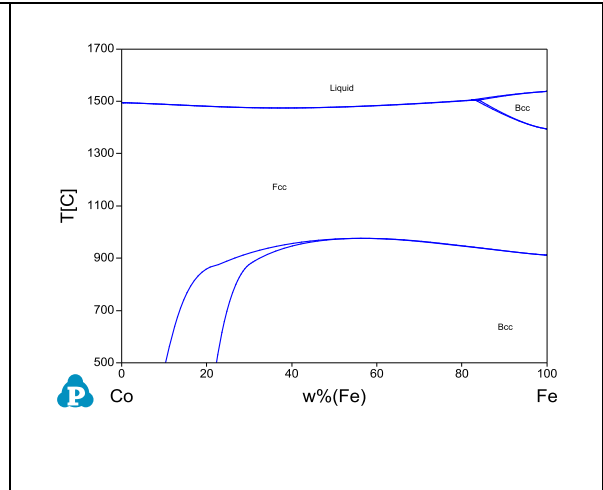
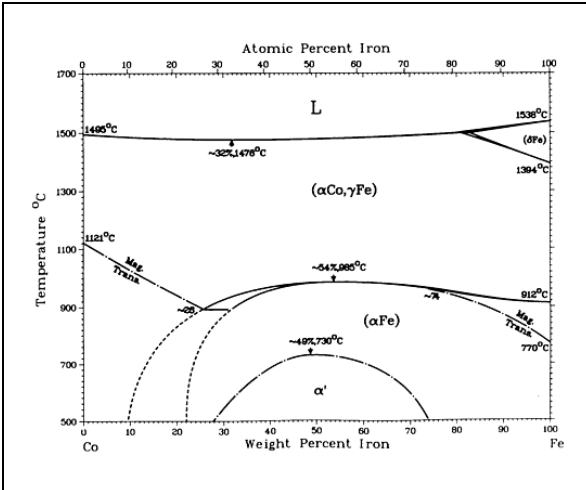
3.3.1. Thermodynamic database validation

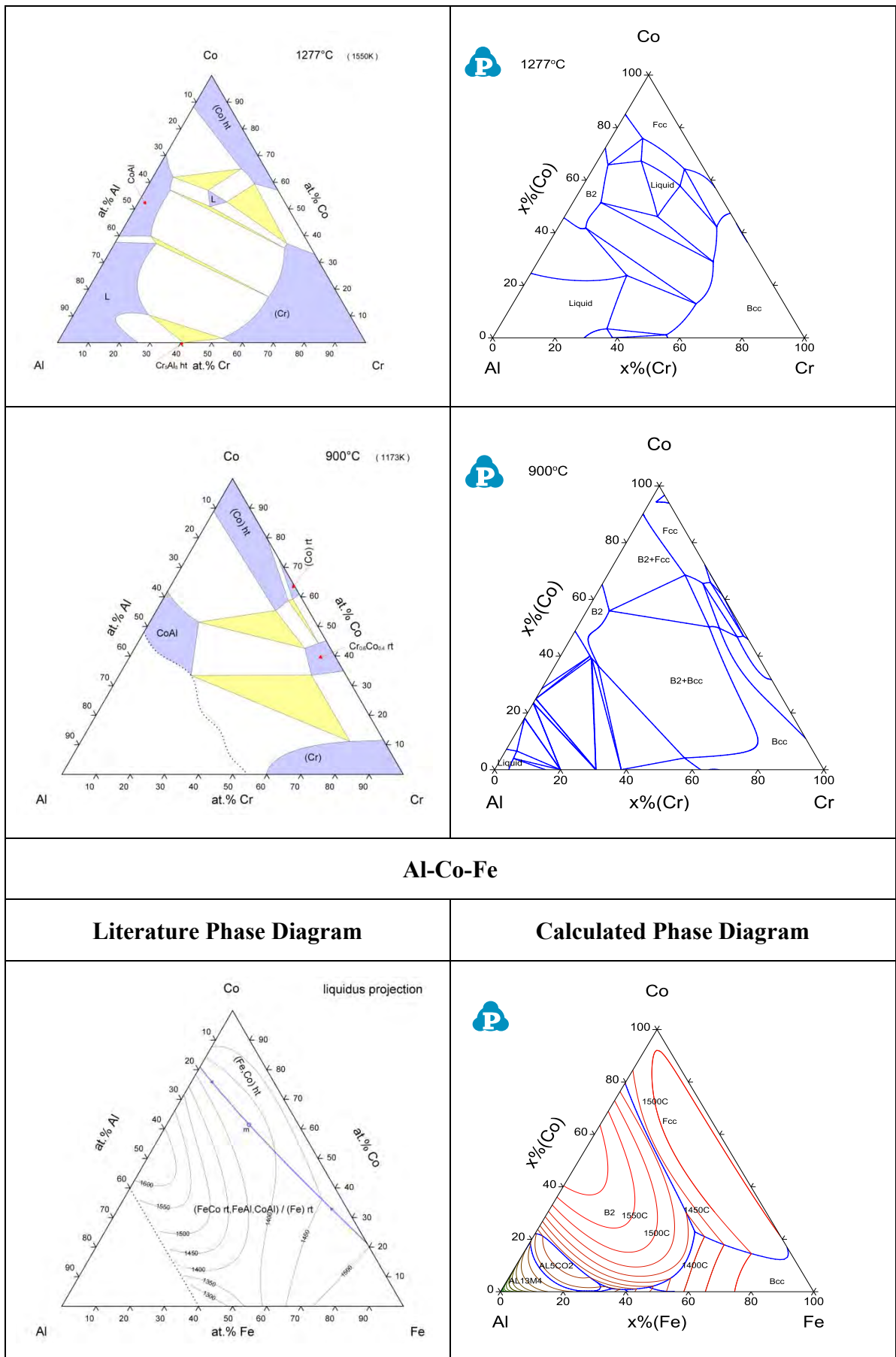
As discussed before, the CALPHAD approach is a semi-empirical method. Careful validations and improvements are needed in order to carry out reliable thermodynamic predictions. All the constituent binaries and ternaries of the Al-Co-Cr-Fe-Ni system (as listed in Table 6 and Table 7 above) were critically validated in this work. (as shown in Table 8 and Table 9 below)

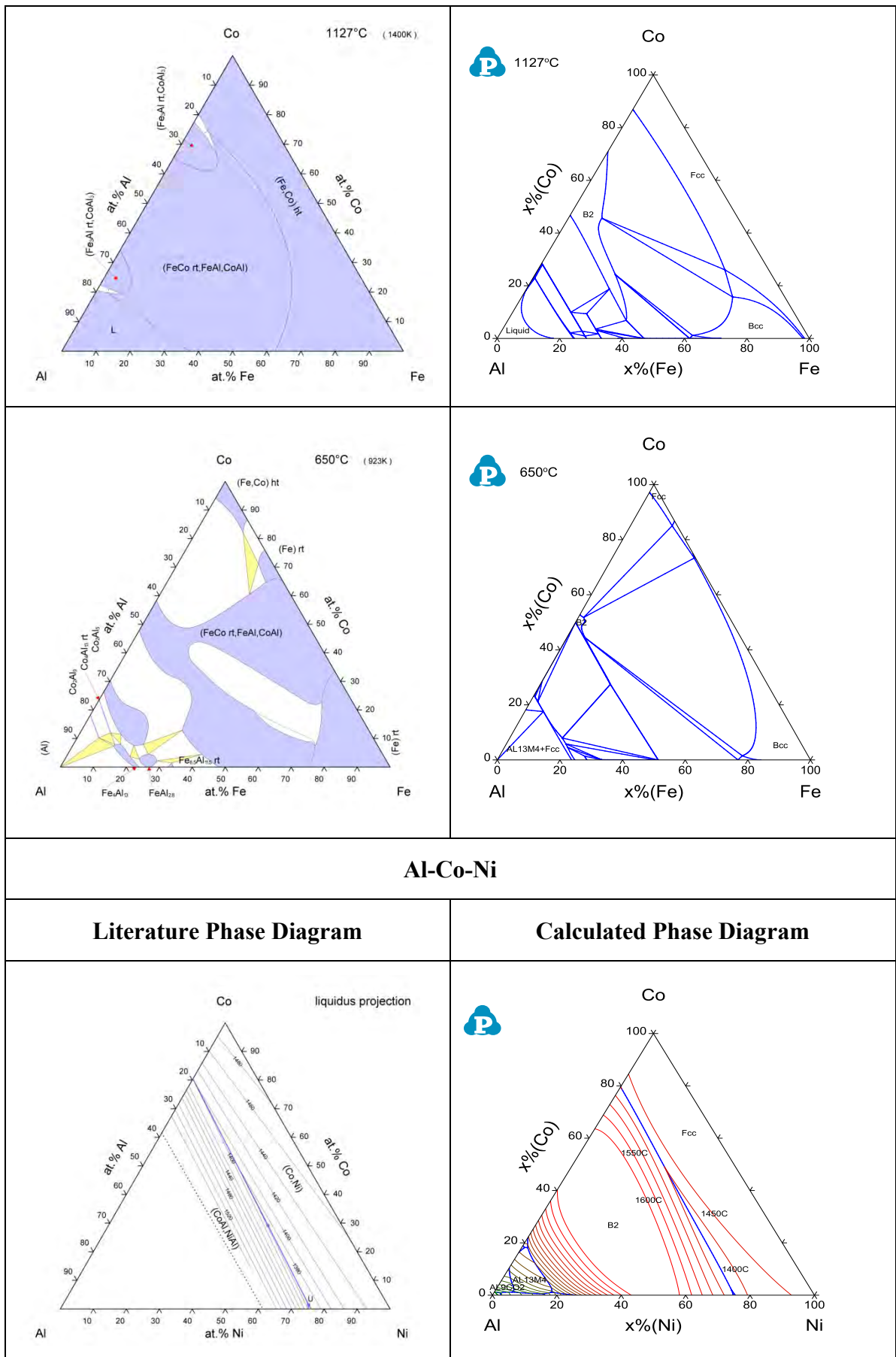
Table 8. Validation of constituent binary systems of the Al-Co-Cr-Fe-Ni system

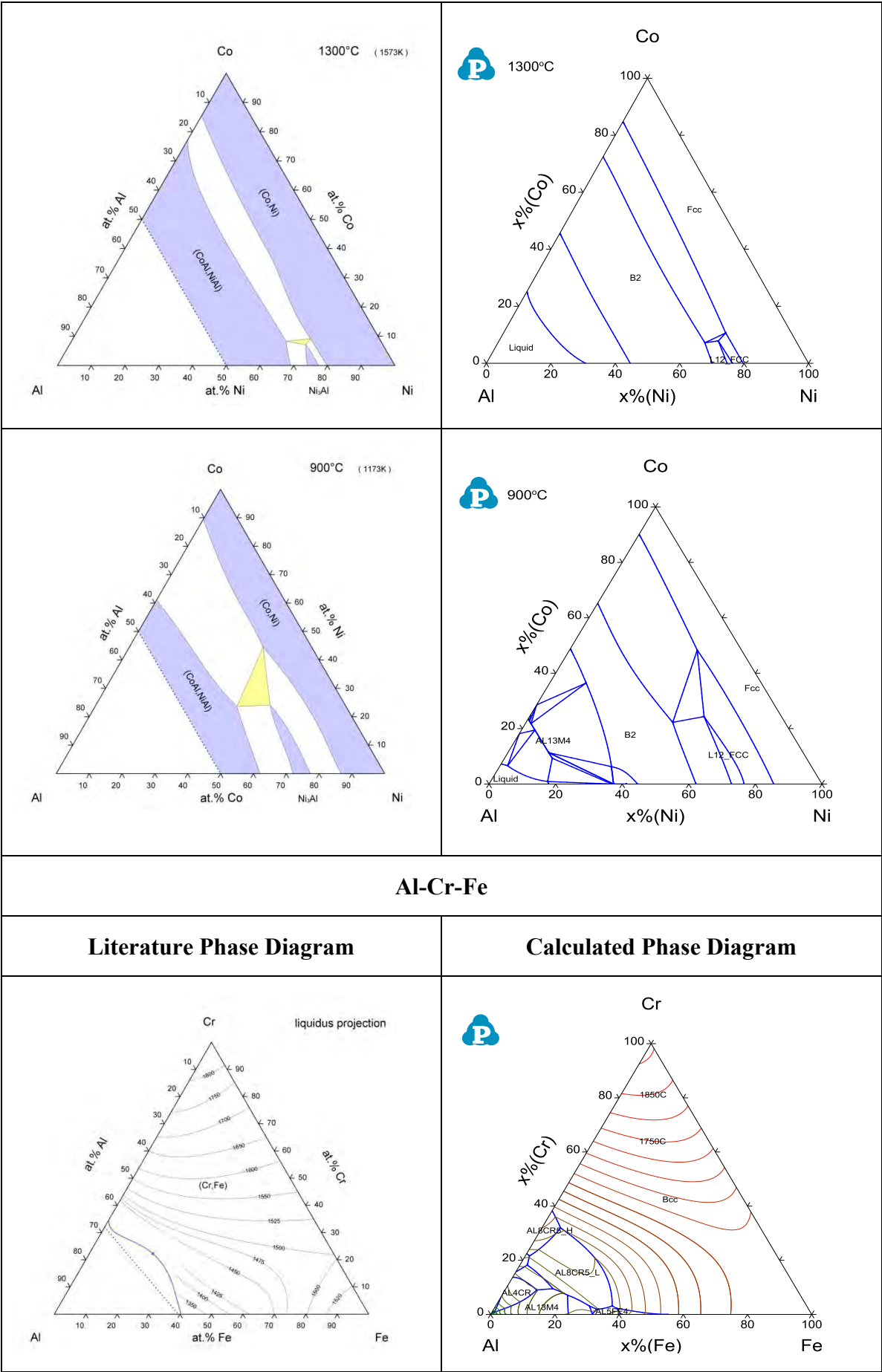


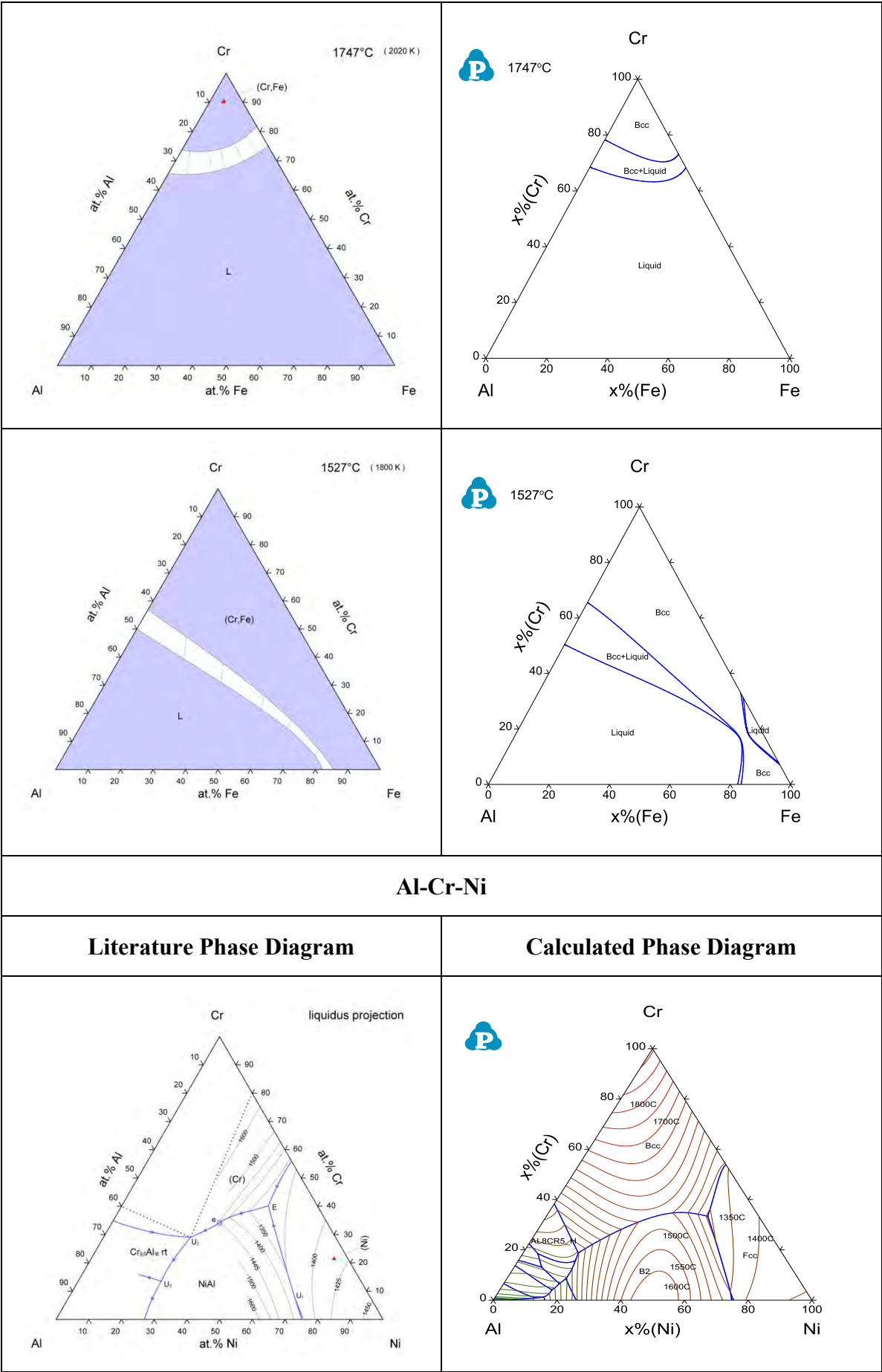


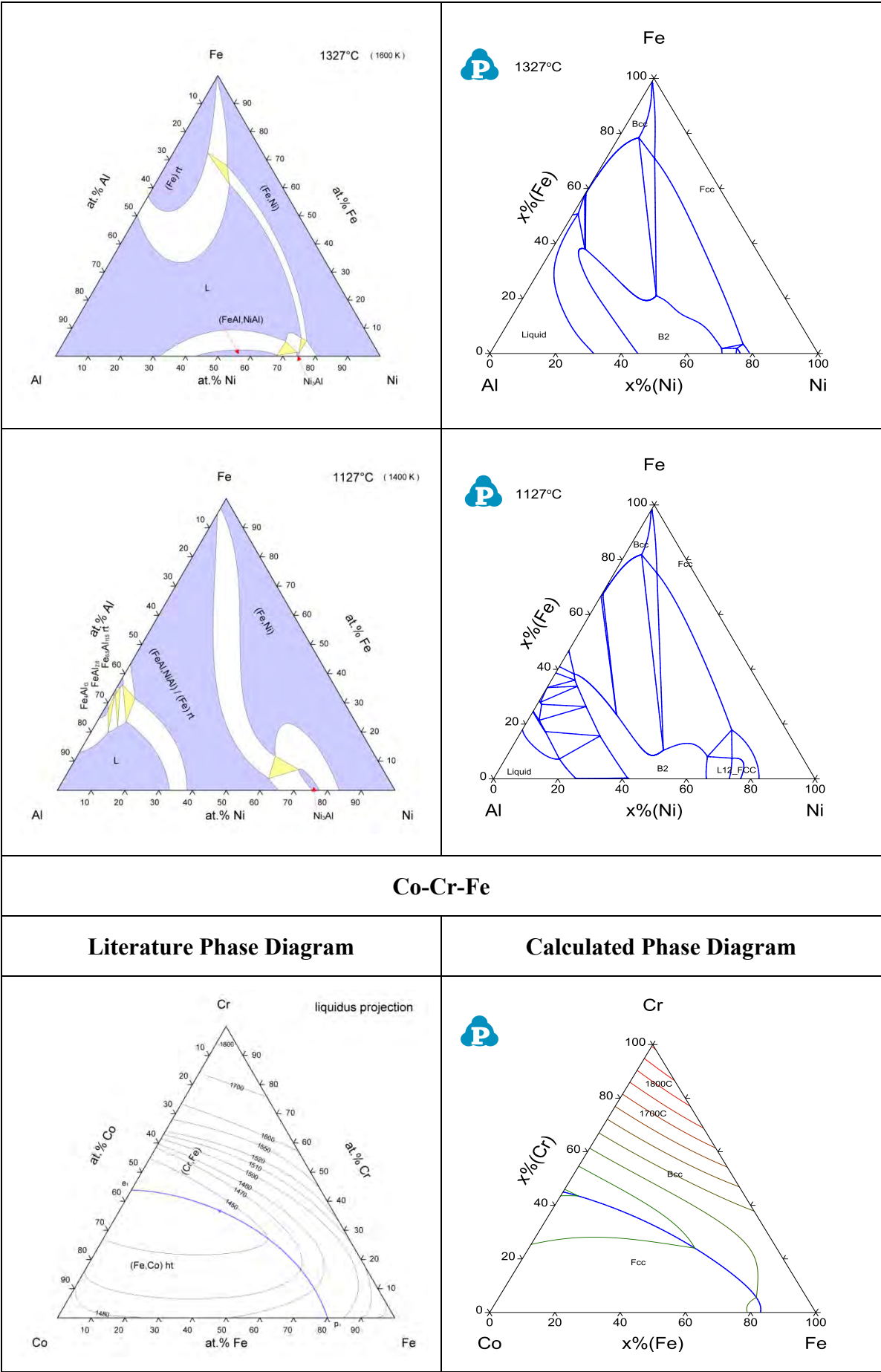


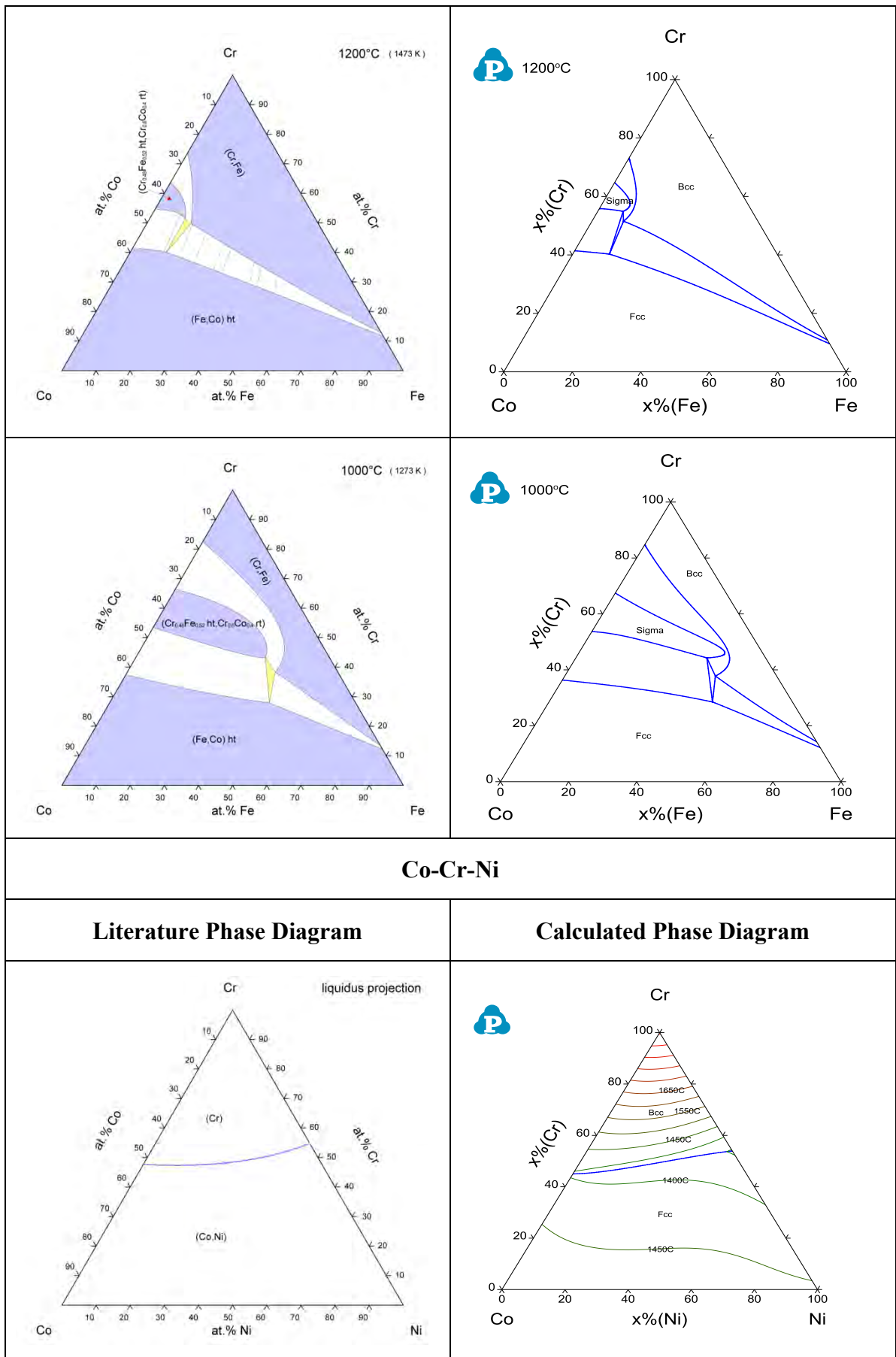


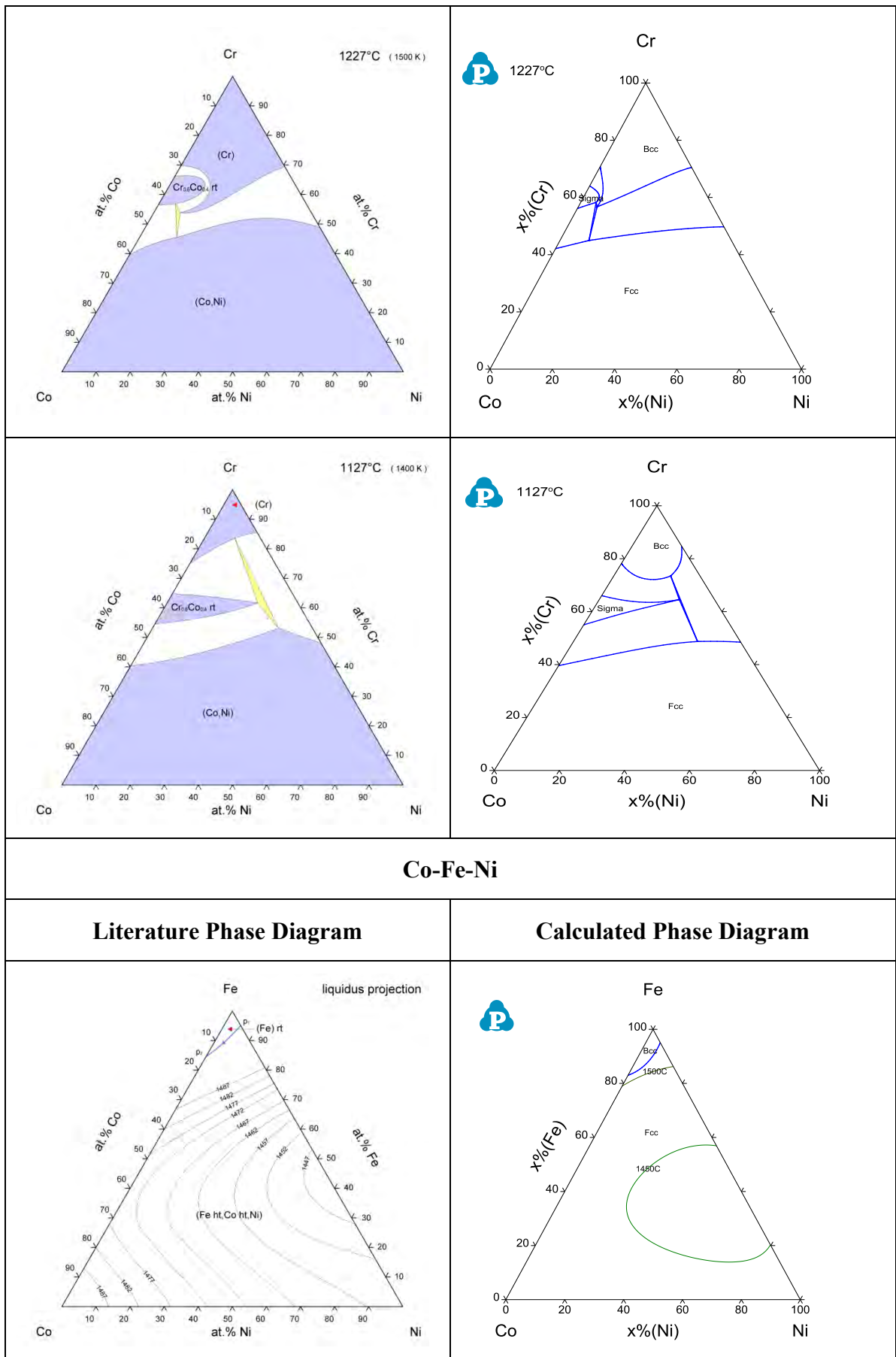


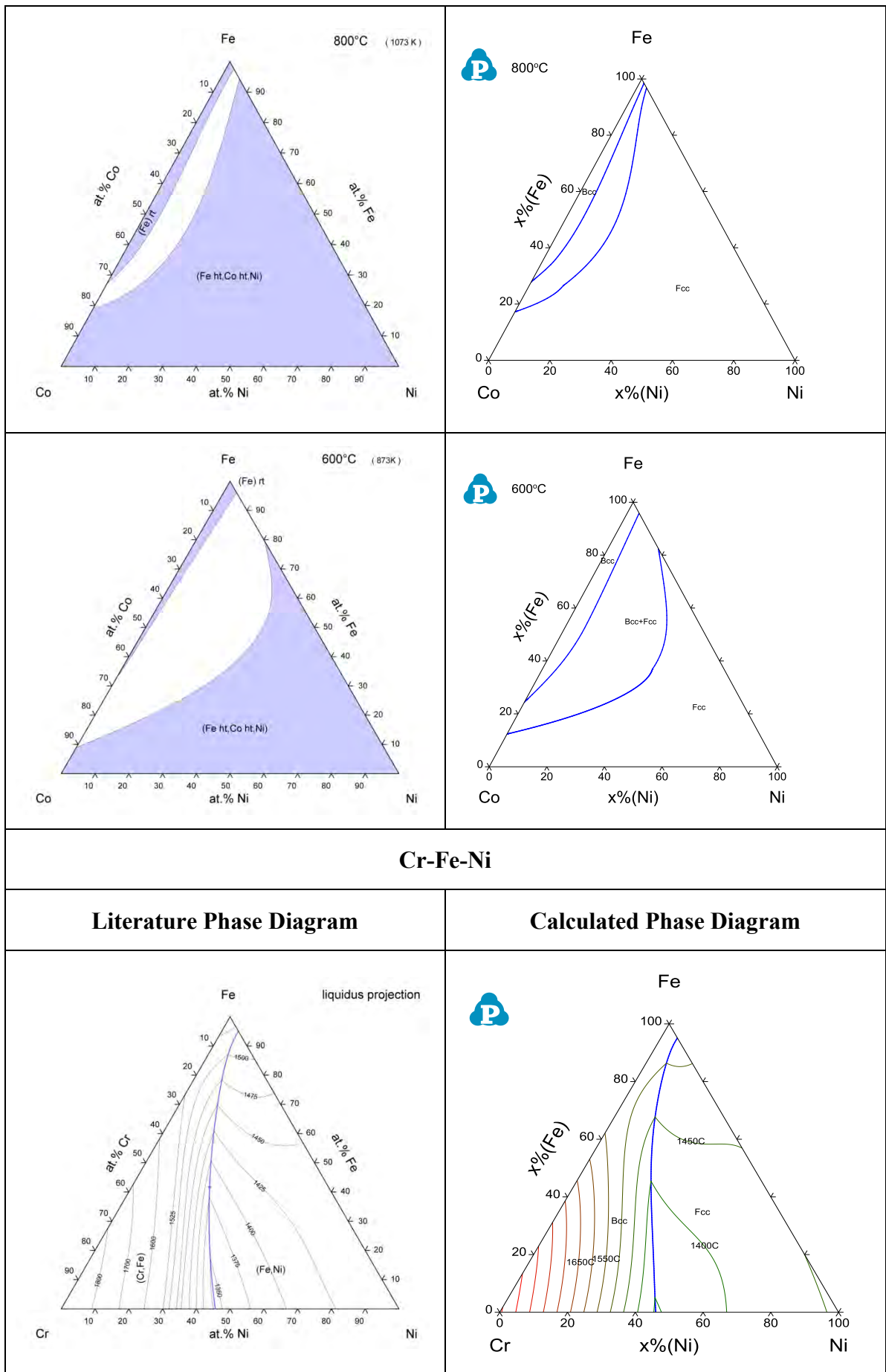


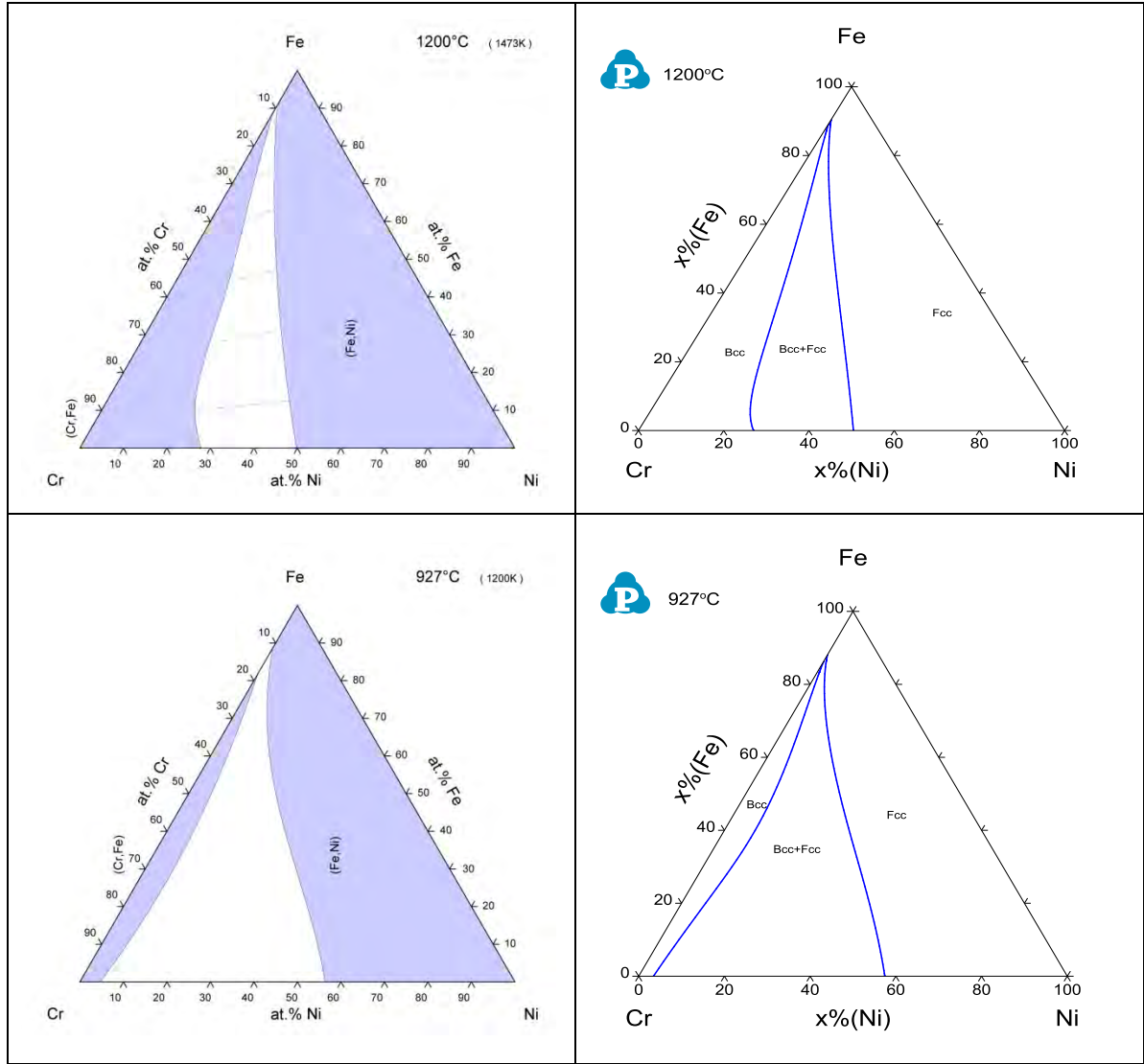












The comparison between the calculated constituent binaries and ternaries of the Al-Co-Cr-Fe-Ni system are in good agreement with the literature phase diagrams. Then the thermodynamic database of the Al-Co-Cr-Fe-Ni quinary system was obtained via extrapolation, which enables us to carry out the phase diagrams of this system within the whole composition range. The calculated phase diagrams can be used as guidelines for the development of Al-Co-Cr-Fe-Ni HEAs.

3.3.2. Application of thermodynamic calculation

Kao et al [71] did the investigation on the $\text{Al}_x\text{CoCrFeNi}$ alloys. For the as-cast structure of the $\text{Al}_x\text{CoCrFeNi}$ HEAs, it is *fcc* structure when $x < 0.45$ and *bcc* structure when $x > 0.88$. The *fcc*+*bcc* duplex structure was seen when the Al ratio is in the mid-range, i.e., $0.45 < x < 0.88$. Figure 44 shows the calculated isopleth of $\text{Al}_x\text{CoCrFeNi}$ and it is in good agreement with the experimental observation [71]. Isopleths with various ratios of Co, Fe and Ni are also calculated in order to fully understand the effect of each element on the *fcc*/*bcc* phase

transition of the AlCoCrFeNi-based HEAs. Figure 45(a) is the vertical section of AlCrFeNi–AlCo_xCrFeNi, Figure 45(b) is the vertical section of AlCoCrNi–AlCoCrFe_xNi, and Figure 45(c) is that for the AlCoCrFe–AlCoCrFeNi_x. As is seen from Figure 45, the Co, Fe and Ni all act as *fcc* stabilizers. On the other hand, it is hard to get *fcc* structure as the primary phase in all three vertical sections. This is because high Al ratio (Al=1) is used in the calculation of these diagrams.

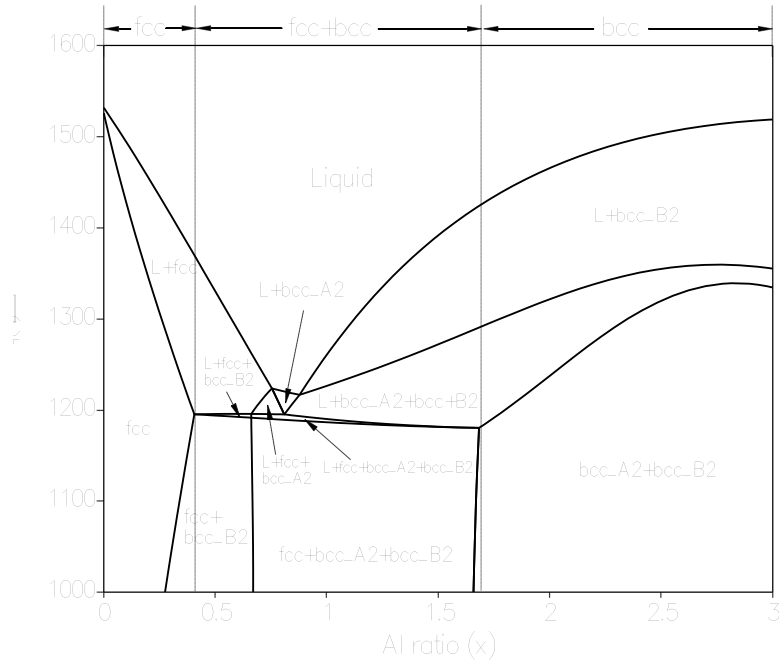
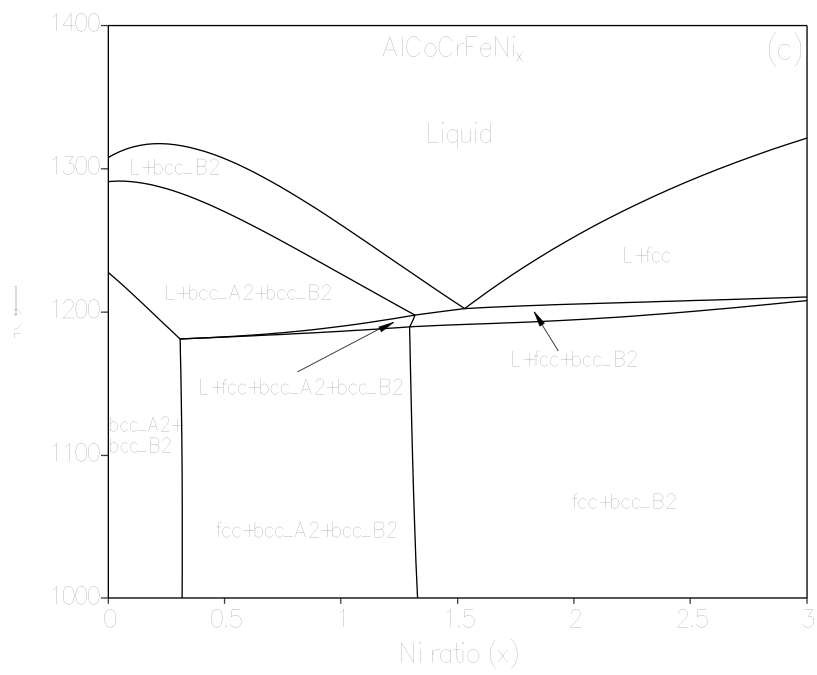
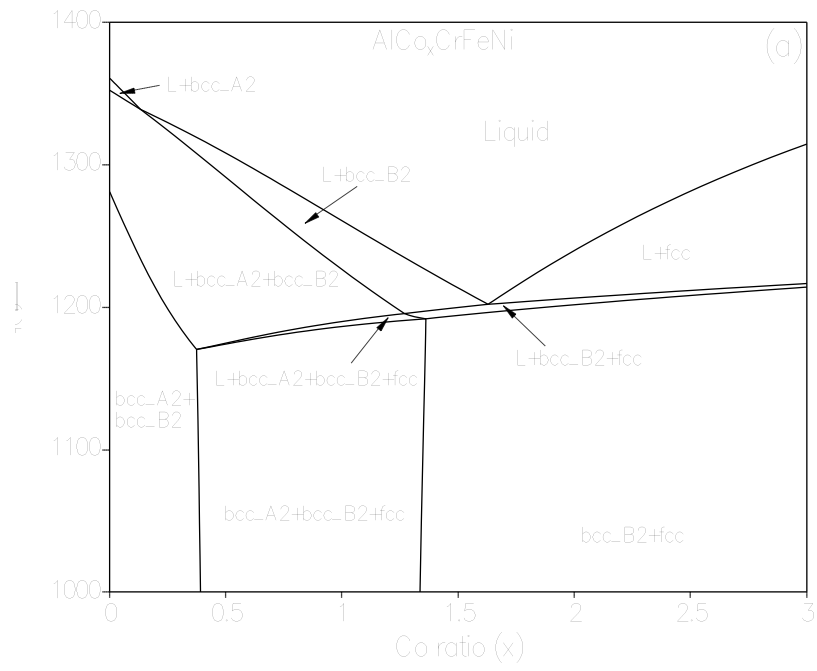


Figure 44. The calculated isopleth of the Al_xCoCrFeNi alloys with x=0~3 using our current thermodynamic description



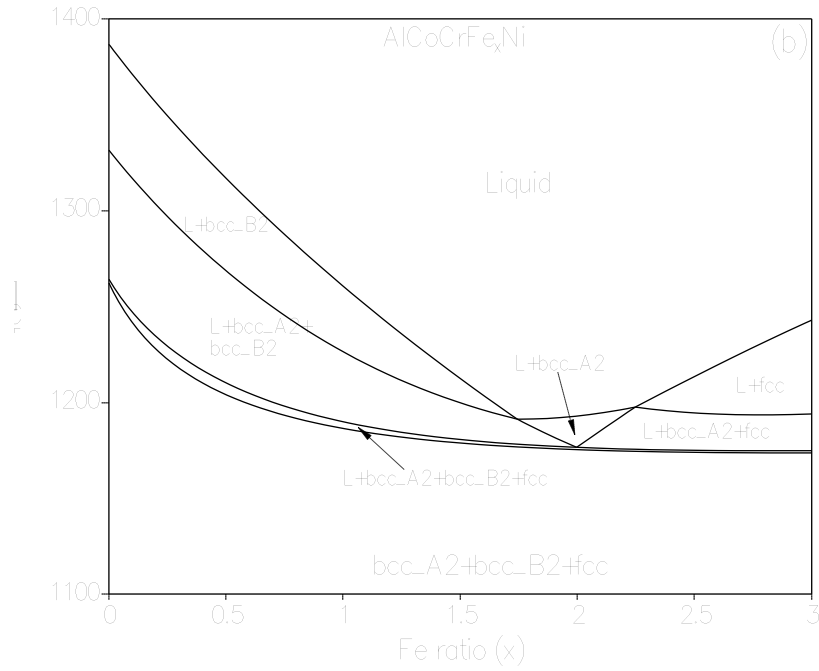


Figure 45. The calculated isopleths of the Al-Co-Cr-Fe-Ni alloys using our current thermodynamic description with different Co, Fe and Ni ratios, respectively.

The above examples show one of the valuable applications of thermodynamic calculations for this project. Based on the above calculated phased diagrams, we can also identify proper alloy composition and heat-treatment schedule to obtain the HEAs with desirable microstructure. For example, the single fcc HEA will be obtained for the $\text{Al}_{0.1}\text{CoCrFeNi}$ alloy when heat-treated at 1000°C on the basis of Figure 44, which has been confirmed by the experimental study of our team member of this project.

3.4. Summary and Conclusions

- a. All the constituent binary and ternary systems of the Al-Co-Cr-Fe-Ni system were thermodynamically modeled within the whole composition range. Comparisons between the calculated phase diagrams and literature data are in good agreement. The multi-component thermodynamic database of the Al-Co-Cr-Fe-Ni system was then obtained via extrapolation.
- b. The current Al-Co-Cr-Fe-Ni thermodynamic database enables us to carry out phase diagrams, which can be used as useful guidelines to identify the Al-Co-Cr-Fe-Ni HEAs with desirable microstructures.

4. Task 4: Mechanical Behavior and Microstructural Characterization

The objective of this task is to study the mechanical behavior and microstructural stability of the various phases formed at elevated temperatures in HEAs and compare with thermodynamic calculations in Task 3. Limited mechanical and microstructural behavior of HEAs at high temperatures have been studied previously and shows tremendous potential for elevated-temperature applications by exhibiting high hardness and yield strength at temperatures greater than 1,100 °C

4.1. Introduction

Nuclear, turbine, and aerospace industries currently place high demands on high-temperature structural-alloy properties [72], and look for materials that could be superior to conventional nickel-based superalloys. In the last decade, a new class of materials, called high-entropy alloys (HEAs) or multi-principal-element alloys (MPEAs), has been proposed and developed [56, 57, 59, 73-87]. These alloys contain 5 or more elements at near equiatomic concentrations and may favor the formation of disordered solid-solution phases

with high mixing entropy, $\Delta S_{mix} = -R \sum_{i=1}^N x_i \ln x_i$, in place of ordered intermetallic phases that have a much smaller entropy of mixing [56, 73, 75, 87-89]. Here x_i is the atomic fraction of element, i , and R is the gas constant. The Gibbs free energy of mixing, ΔG_{mix} , of a given phase can be expressed as:

$$\Delta G_{mix} = \Delta H_{mix} - T \Delta S_{mix} \quad (4.1)$$

Here ΔH_{mix} and ΔS_{mix} are, respectively, the enthalpy and entropy of mixing, and T is the absolute temperature. In disordered solid solutions (i.e., ideal or regular solid solutions), ΔS_{mix}

$= -R \sum_{i=1}^N x_i \ln x_i$, and in ordered intermetallic phases, $\Delta S_{mix} \approx 0$. From Equation (4.1),

increasing ΔS_{mix} will reduce the Gibbs free energy and may stabilize the solid-solution phase. This trend will be more pronounced at elevated temperatures. Controlled by solid-solution-strengthening, the yield strength of HEAs can be very high, and may be comparable to bulk metallic glasses (BMGs) [74]. While BMGs have high strength only at relatively low temperatures (below the glass-transition/crystallization temperatures), crystalline HEAs may retain their high strength at higher temperatures [81, 83, 90].

Alloy microstructures must be stable for elevated-temperature applications, because

phase transformations occurring during use could deteriorate properties and lead to failure. High ΔS_{mix} stabilizes disordered solid solutions at elevated temperatures. The entropy product, $T\Delta S_{\text{mix}}$, decreases with temperature and ordered intermetallic phases with large, negative enthalpies of formation can become thermodynamically preferable. On the other hand, phase transformation kinetics decrease with decreasing temperature, and the formation of the intermetallic phases may require long annealing times. At the same time, suppressed kinetics may lead to the precipitation of exceptionally fine, nanometer-sized particles and considerably improved properties of these alloys at ambient temperatures. Therefore, studying the phase and microstructure stability in HEAs is important for candidate high-temperature structural materials.

In the as-cast condition through the rapid quenching process, HEAs studied to date tend to have a single-phase body-centered-cubic (BCC), face-centered-cubic (FCC), and/or hexagonal-close-packed (HCP) crystal structures [83, 85, 91-93]. Many of them may have precipitations of B2 in BCC and/or L1₂ in FCC phases [94, 95]. After processing at elevated temperatures, e.g., by forging, annealing, and aging, additional phases, including intermetallic phases, can form and make HEAs more complex [96-98]. For example, after thermo-mechanical treatments, the intermetallic σ phase was found in Al_xCoCrFeNi and Al_xCoCrCuFeNi HEA systems [99-101], and unidentified phases also appeared [102, 103]. Unfortunately, thermodynamics and kinetics of phase transformations in HEAs are still unclear, making phase evolution difficult to predict.

The present work focuses on one of the earliest quinary HEAs, AlCoCrFeNi, first reported in 2007 [74]. It belongs to the Al_xCoCrFeNi system, which is one of the most well-developed and refined HEA systems [74, 83, 84, 95, 96, 100, 104-112]. The AlCoCrFeNi alloy shows a high compressive yield strength ($\sigma_Y = 990$ MPa) with a reasonable compressive ductility ($\varepsilon = \sim 63$ %) at 500 °C [113]. This high strength at elevated temperatures makes it a promising structural material. A single-phase BCC crystal structure has been reported for the as-cast AlCoCrFeNi [96, 107]. Others, however, report the presence of B2 [105, 111] and A1 or L1₂ structures in the as-cast condition [95]. There are no publications in the open literature on the homogenized phase stability and high-temperature tensile properties of this important HEA system. In this paper, the effect of the homogenization heat treatment on the as-cast microstructure is studied, and the influence of this substantial change in microstructures on tensile properties is investigated. Comparison between the predicted phase equilibria and phases observed after homogenization heat treatment is made.

4.2. Thermodynamic Modeling

The as-cast HEAs may have different phases than the homogenized HEAs, since rapid cooling can suppress equilibrium phases, which often require a significant elemental

redistribution. An effective approach is necessary to determine and/or predict multi-component phase diagrams for HEA systems. Traditionally, binary and ternary phase diagrams have relied upon experimental methods. The first-principles alloy theory was applied to predict the structures of the $\text{Al}_x\text{CoCrFeNi}$ HEA system, and it was concluded that alloys around the equimolar AlCoCrFeNi composition have superior mechanical performance, as compared to the single-phase regions [84]. Meanwhile, Widom et al. applied a hybrid Monte Carlo and molecular-dynamics (MD) method to study the temperature-dependent chemical order for the refractory MoNbTaW HEA [114]. They found that the Monte Carlo species swaps allow for the equilibration of the structure, which cannot be achieved by conventional MD simulations [114]. In addition, the phenomenological CALculation of PHase Diagrams (CALPHAD) approach [60] is proved to be an effective aid in materials design [115-118], and has recently been successfully used in the AlCoCrFeNi HEA system [119].

The essence of the CALPHAD approach is to obtain self-consistent thermodynamic descriptions (Gibbs energy functions) of lower-order (binary and ternary) systems by fitting to known thermodynamic and phase-equilibrium data. A thermodynamic description represents a set of Gibbs-energy functions with optimized thermodynamic-model parameters for all the phases in a system. The thermodynamic description for higher-order systems can be obtained via an extrapolation method [120]. This description enables estimates of phase diagrams and thermodynamic properties of multi-component systems that are experimentally unavailable.

A thermodynamic database for the Al-Co-Cr-Fe-Ni system was developed [119]. Different from traditional alloys, which usually focus at one key element corner, the HEAs have multiple key elements. This trend requires the database to be valid in the entire composition region. The current database was developed, using the available experimental information for the 10 constituent binaries and 10 constituent ternaries. In this database, the disordered solution phases, such as A1 and A2, are described by the substitutional solution model; the ordered intermetallic phases, such as sigma and B2, are described by the compound-energy formalism, and the line compounds are described by the stoichiometric model. Details of these thermodynamic models can be found in References [121, 122], and will not be repeated here. It should also be pointed out that the Gibbs energy of all the phases in the 5-component system were obtained from those of binaries and ternaries [119], and no thermodynamic model parameters were optimized using the experimental data of the present work for the 5-component system. All the calculations in this work were performed by the *PANDAT* software.

4.3. Results

4.3.1. Microstructures of the Alloy in the As-cast Condition

The microstructure of the AlCoCrFeNi-AC alloy is shown in Figure 46. The microstructure consists of equiaxed grains (Figure 46a). Flowery, branched dendrites are seen inside the grains at higher magnification (Figure 46b). The dendrites span is $\sim 40\ \mu\text{m}$, and the arm thickness is $\sim 20\ \mu\text{m}$. Figure 47 presents the image quality, inverse pole-figure and phase-identification maps of grains and dendrites, as well as the elemental maps. The data were collected simultaneously with the EBSD and EDS techniques. Randomly-oriented equiaxed matrix grains are clearly recognized on the image quality and inverse pole figure maps (Figure 47a-b). The phase map (Figure 47c) and EDS element mapping (Figure 47d-h) reveal two distinct compositions. The dendrites with the volume fraction of 45 % are enriched with Al and Ni (called NiAl-rich dendrites), and the interdendritic regions with the volume fraction of 55 % are enriched with Cr and Fe (called NiAl-poor interdendrites), while Co is uniformly distributed inside these phases. The chemical compositions of both NiAl-rich dendrites and NiAl-poor interdendrites are shown in Table 10.

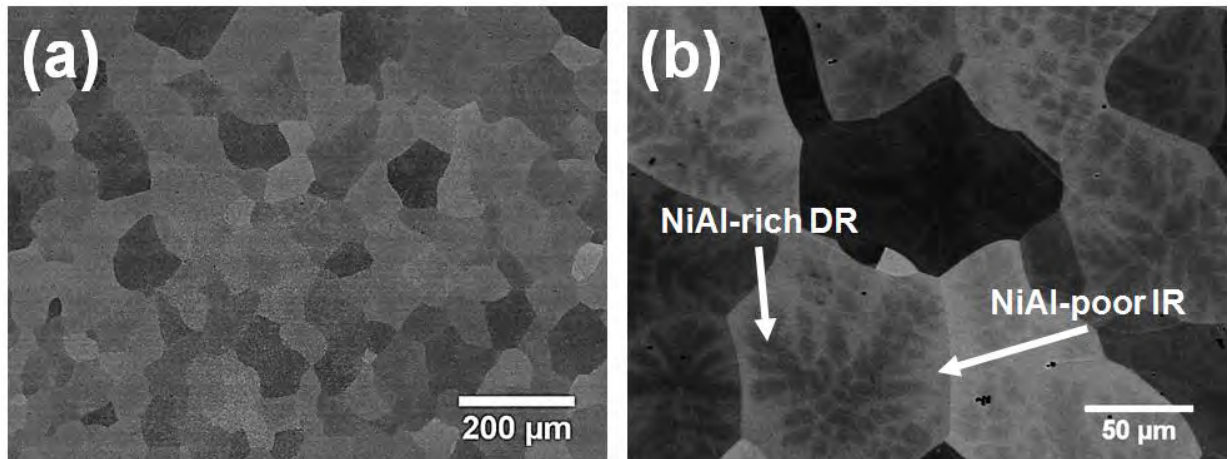


Figure 46. Back-scatter-electron (BSE) images of the as-cast alloy at two magnifications showing NiAl-rich dendrites (DR) and NiAl-poor interdendrites (IR)

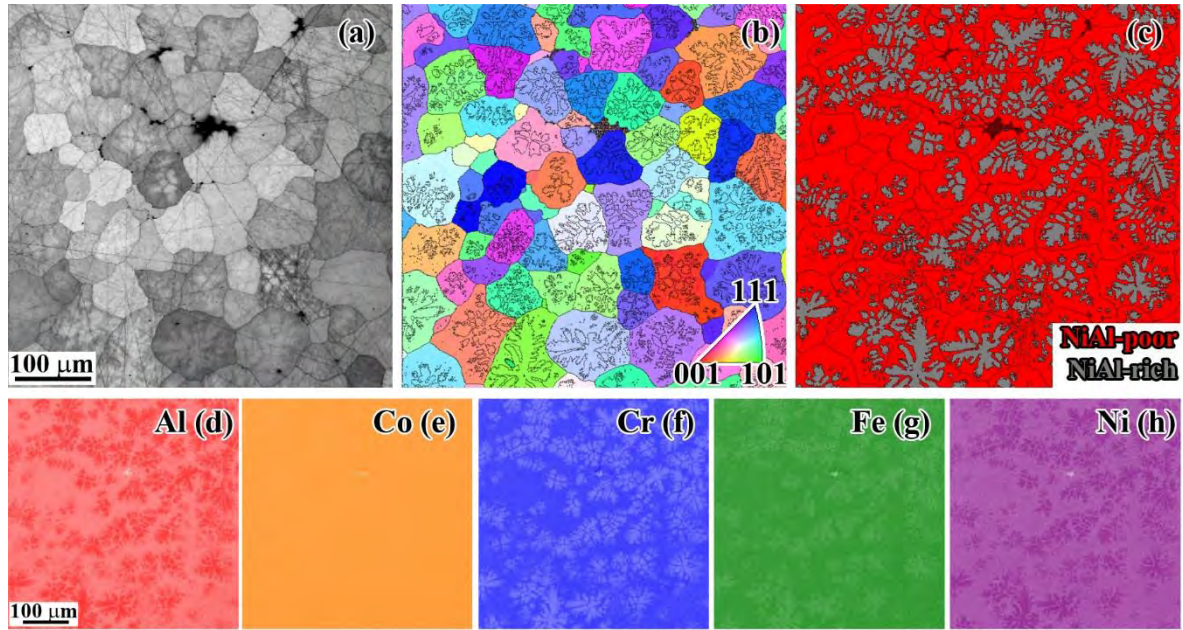


Figure 47. The EBSD (a) image-quality map, (b) inverse pole-figure map, and (c) phase map. Black lines in (b-c) are phase or grain boundaries. Simultaneously-acquired EDS (d-h) X-ray maps of the microstructures of the AlCoCrFeNi-AC alloy.

Table 10. Chemical compositions (at. %) of NiAl-rich dendrites (DR) and NiAl-poor interdendrites (ID) in the as-cast condition, by SEM-EDS (more than 3 different locations and less than 2 at. % standard deviation).

AlCoCrFeNi-AC					
Element Region	Al	Co	Cr	Fe	Ni
NiAl-rich DR	26	21	14	16	22
NiAl-poor ID	18	19	22	21	19

To further investigate phase structures of NiAl-rich dendrites and NiAl-poor interdendrites, bright-field and dark-field TEM images of the interior of the matrix grains are exhibited in Figure 48. Note that the origin of the TEM sample came from either NiAl-rich or NiAl-poor region due to the sample preparation limitation. The dark-field TEM images were produced using a fundamental spot of the A2 and B2 phases [Figure 48(b)] and a superlattice spot of the B2 phase [Figure 48(c)]. They reveal a lamellar structure of the matrix grains consisting of fine, nanometer-sized lamellae of A2 and B2 phases. Figure 48(d) is a false-color scanning transmission electron microscopy (STEM) EDS map showing the distribution of Al (red), Co (green), and Cr (blue) in the phases. It can be clearly identified

that the A2 phase is enriched with Cr, and the B2 phase is enriched with Al. A bright-field and high-angle-annular-dark-field (BF-HAADF) pair of aberration-corrected STEM (AC-STEM) images also confirms its A2+B2 structures (Figure 49). The semiquantitative analyses by STEM-EDS spectra of A2 and B2 phases are shown in Table 11. In addition, a very small amount (volume fraction is less than 1-2 %) of fine precipitates of an additional phase, which has an A1 (disordered FCC) structure and is enriched with Co, is also identified inside grains (Figure 48d). This phase is anticipated from the solidification simulation conducted in the following section by the Scheil model [123], while the chemical compositions by the STEM-EDS spectra quantification of this A1 phase are not reliable due to its thickness less than a full foil. The reason is when we place a beam on the particle, we are measuring X-rays (chemistry) from both the particle and the matrix. In reality, we don't know how thick the particle is, relative to the matrix. Thus, we don't know how much contribution is coming from each. Therefore, STEM-EDS spectra quantification of the A1 phase is not reliable and not presented in Table 11. The nano-lamellar A2+B2 structure seems to co-exist in both NiAl-rich dendrites and NiAl-poor interdendrites, while the A1 phase might only exist in the interdendritic region, and the reasons are discussed in the following sections.

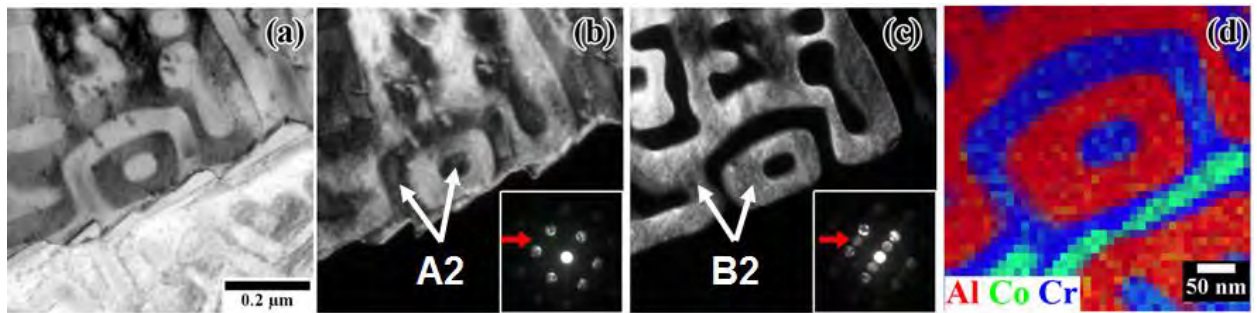


Figure 48. Bright-field and dark-field TEM images of the interior of the matrix grains: (a) is bright-field TEM, (b) fundamental A2 dark-field TEM, and (c) superlattice B2 dark-field TEM images. Insets to (b-c) are convergent beam electron diffraction patterns from A2 and B2, respectively. Arrows denote the superlattice position of B2. (d) is a false-color STEM-EDS map showing Al (red), Co (green), and Cr (blue).

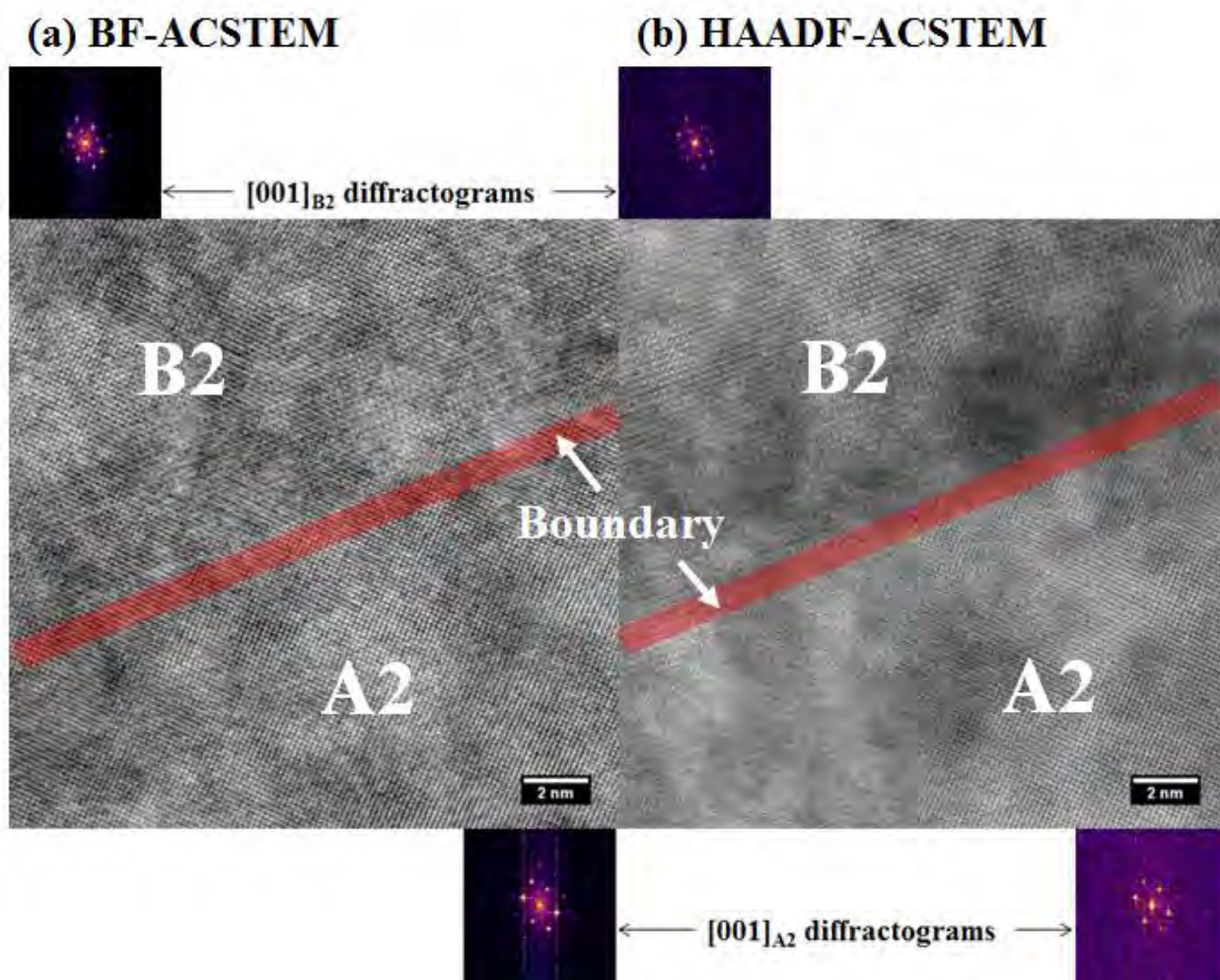


Figure 49. A BF-HAADF pair of AC-STEM images for the as-cast alloy showing A2+B2 structures

Table 11. Chemical compositions (at. %) of each phase in AlCoCrFeNi-AC (A2+B2+A1) by STEM-EDS (semi-quantitative analyses) and AlCoCrFeNi-HP (A2+B2+A1+σ) by SEM-EDS (more than 3 different locations and less than 2 at. % standard deviation).

AlCoCrFeNi-AC					
Element Phase	Al	Co	Cr	Fe	Ni
A2 *	trace	20	~ 50	25	5
B2 *	~ 40	15	trace	10	30
A1 **	-	-	-	-	-

AlCoCrFeNi-HP					
Phase \ Element	Al	Co	Cr	Fe	Ni
A2	3	19	43	30	6
B2	30	19	9	14	27
A1	8	23	27	27	15
σ	5	24	28	31	11

* Semiquantitative analyses from STEM-EDS spectra

** The A1 phase is not of a full-foil-thickness, so that STEM-EDS spectra quantification is not reliable.

To sum up, based on the electron-microscopy study, the AlCoCrFeNi-AC primarily consists of a nano-lamellar mixture of the A2 and B2 phases, as well as a very small amount of A1 nanoprecipitates. The NiAl-rich dendrite regions are enriched with the B2 phase, in addition to the A2 phase. The NiAl-poor interdendrite regions are enriched with the A2 phase, beside a large amount of B2 phases and a small amount of A1 nanoprecipitates. The volume fraction of each phase presented in the as-cast condition is shown in Table 12.

Table 12. Volume fraction of each phase in as-cast (A2+B2+A1) and homogenized (A2+B2+A1+ σ) conditions by the EBSD analysis.

AlCoCrFeNi-AC		
Phase		Volume fraction
NiAl-rich DR	A2	29 %
	B2	71 %
	Total	100 %
NiAl-poor ID	A2	58 %
	B2	40 %
	A1	2 %
	Total	100 %
Overall	A2	46 %
	B2	53 %
	A1	1 %
	Total	100 %

AlCoCrFeNi-HP		
Phase	Experiment	Modeling
A2	24 %	13 %
B2	46 %	38 %
A1	16 %	49 %
σ	14 %	-
Total	100 %	100 %

4.3.2. Microstructures of the Alloy after the Homogenization Treatment

The homogenization treatment led to dramatic changes in the alloy microstructure (Figure 50). The homogenized alloy is called AlCoCrFeNi-HP. Instead of dark dendrites (NiAl-rich) in a bright matrix (NiAl-poor) (Figure 46), light-color precipitates are now recognized inside of the grey-color matrix and along grain boundaries. The different grey levels of the constituents in the backscattered-electron (BSE) images result from different compositions, e.g., brighter contrasts correspond to higher concentrations of heavier elements. The combined EBSD/EDS analysis reveals the presence of four phases in the homogenized alloy (Figure 51). The matrix grains have a B2 crystal structure. Two other phases, one with an A2 crystal structure and another with a tetragonal crystal structure (σ phase), precipitate inside the large B2 grains. The fourth phase, with the A1 crystal structure, mainly precipitates along grain boundaries, although some particles are also present inside the grains. The elemental analysis of these phases reveals that the B2 phase is rich in Ni and Al, the A2 and σ phases are rich in Cr and Fe, and the A1 phase is slightly enriched with Al, Co, and Cr. The chemical compositions of four phases (A2, B2, A1, and σ) determined by SEM-EDS are shown in Table 11, and the volume fractions of these four phases determined through the EBSD analysis, and calculations are shown in Table 12. Bright-field TEM images of the AlCoCrFeNi-HP alloy are shown in Figure 52. Nanoprecipitates with an A2 structure (indicated by red arrows) inside the B2 matrix are easily recognized. As shown in Figure 52(c-g), STEM-EDS X-ray maps of the microstructures of the AlCoCrFeNi-HP alloy (in a homogenized condition) confirm that the A2 nanoprecipitates is enriched with Co, Cr, and Fe, while the B2 matrix are enriched with Ni and Al. The chemical compositions of these phases are consistent with those in the homogenized condition (Table 11), showing that A2 has 19 at. % Co, 43 at. % Cr, and 30 at. % Fe. In all, based on the electron microscopic investigation, the AlCoCrFeNi-HP is confirmed to be composed of four major phases: A2, B2, A1, and σ .

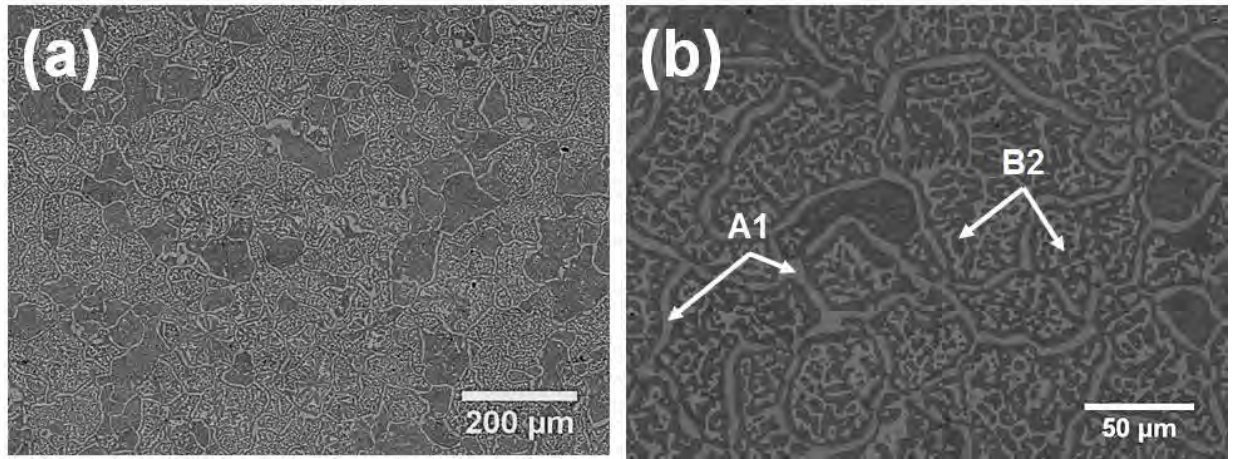


Figure 50. Back-scattered-electron (BSE) images of the homogenized alloy at two different magnifications.

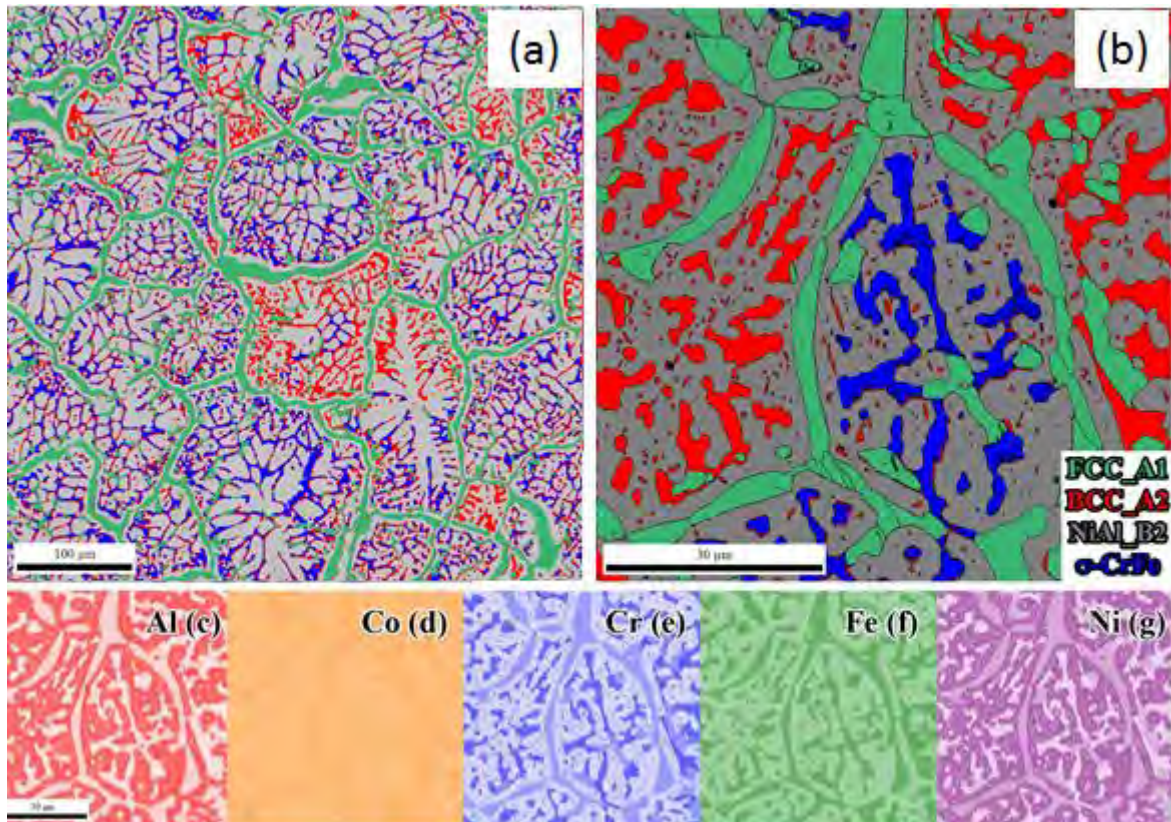


Figure 51. The phase-map microstructures of the AlCoCrFeNi-HP alloy. EBSD + EDS-derived phase map (a) low magnification and (b) high magnification. The EDS maps are presented in (c-g): B2 [(grey color in (a))], A2 [(red color in (a))], σ phase [(blue color in (a))], and A1 [(green color in (a))].

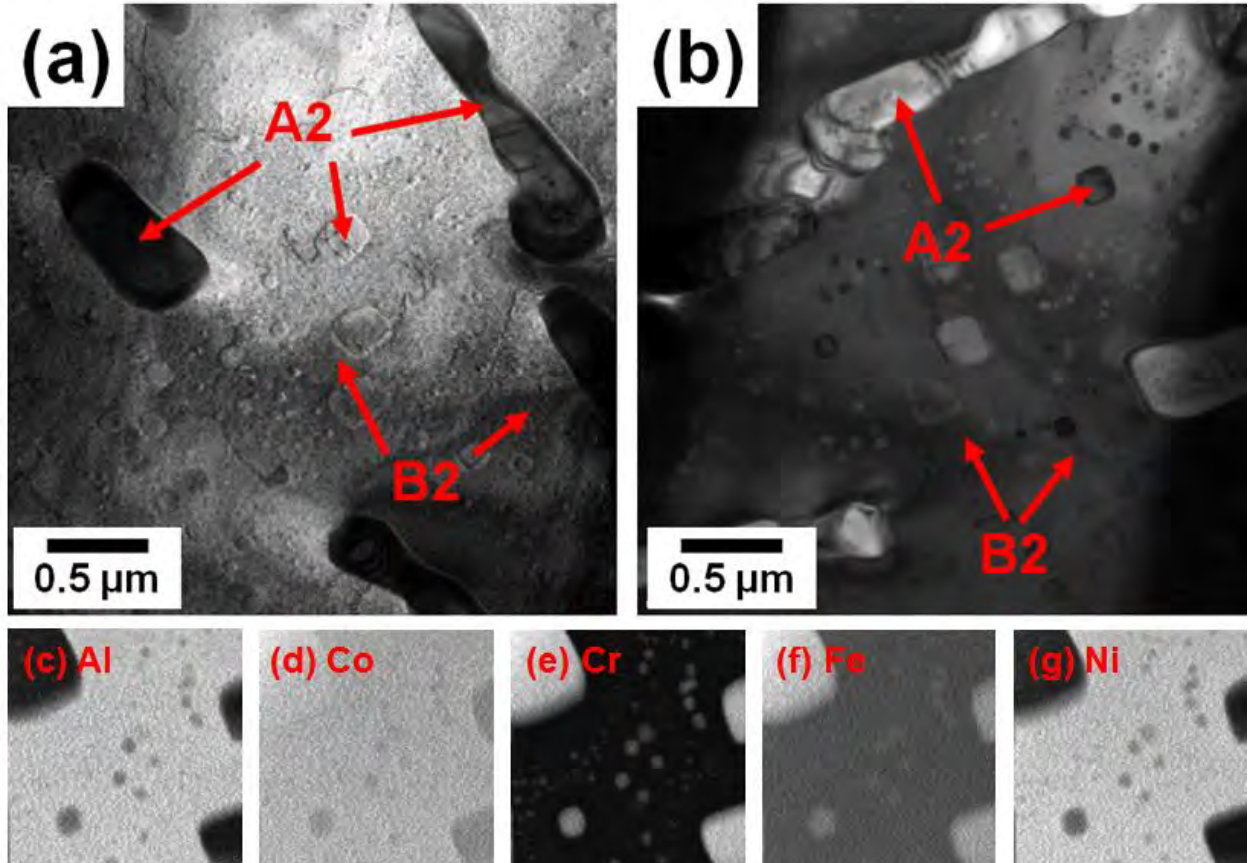


Figure 52. Bright-field (a) and dark-field (b) TEM images of the AlCoCrFeNi-HP alloy. Simultaneously-acquired STEM-EDS (c-g) X-ray maps of the microstructures of the AlCoCrFeNi-HP alloy confirm that the nanoprecipitates are enriched with Co, Cr, and Fe, while the matrix are enriched with Ni and Al.

4.3.3. Characterizations Using Synchrotron X-ray Diffraction

High-energy synchrotron X-ray diffraction shows that the as-cast alloy contains two phases: the A2 phase with a lattice parameter of $a = 2.875(1) \text{ \AA}$, and the B2 phase having a very similar lattice constant and crystal structure with respect to the A2 (Figure 53). The presence of the B2 phase was confirmed by a (100) superlattice peak. The A2+B2 structures were consistent with previous publications [74, 105]. This trend is also very common in other HEA systems, where Tsai et al. found that the lattice constants among the three phases in $\text{Al}_{0.3}\text{CoCrCu}_{0.5}\text{FeNi}$, measured using the TEM images, were very similar [124]. The Co-rich A1 phase found on TEM pictures (Figure 48d) was not identified by synchrotron diffraction, which may be due to its very small amount (volume fraction is less than 1-2 %) presented in the as-cast condition.

Four phases were identified in the AlCoCrFeNi-HP: A2 and B2 having the same lattice parameter $a = 2.869(1) \text{ \AA}$, A1 with $a = 3.596(9) \text{ \AA}$, and σ with $a = 8.800 \text{ \AA}$ and $c =$

4.544 Å. The heat treatment slightly alters the lattice parameter of the A2 and B2 phases from 2.875(1) Å to 2.869(1) Å. This trend may be caused by the diffusion of solute atoms and then creation of vacancies among A2+B2 phases in order to form another two new phases (A1 and σ). Such diffusion will also lead to chemical-composition changes, possibly contributing to the slight change of lattice parameters. The σ phase is an ordered intermetallic compound with $P4_2/mnm$ (#136) [125]. The three strongest peaks belonging to this phase, (410), (411), and (331), as well as (002), are found in the synchrotron pattern. Three other σ peaks, (330), (202), and (212), are shielded by peaks from other phases. In sum, phase identification for both the as-cast (A2+B2) and homogenized (A2+B2+A1+ σ) conditions using synchrotron X-ray diffraction well agrees with the electron microscopic results.

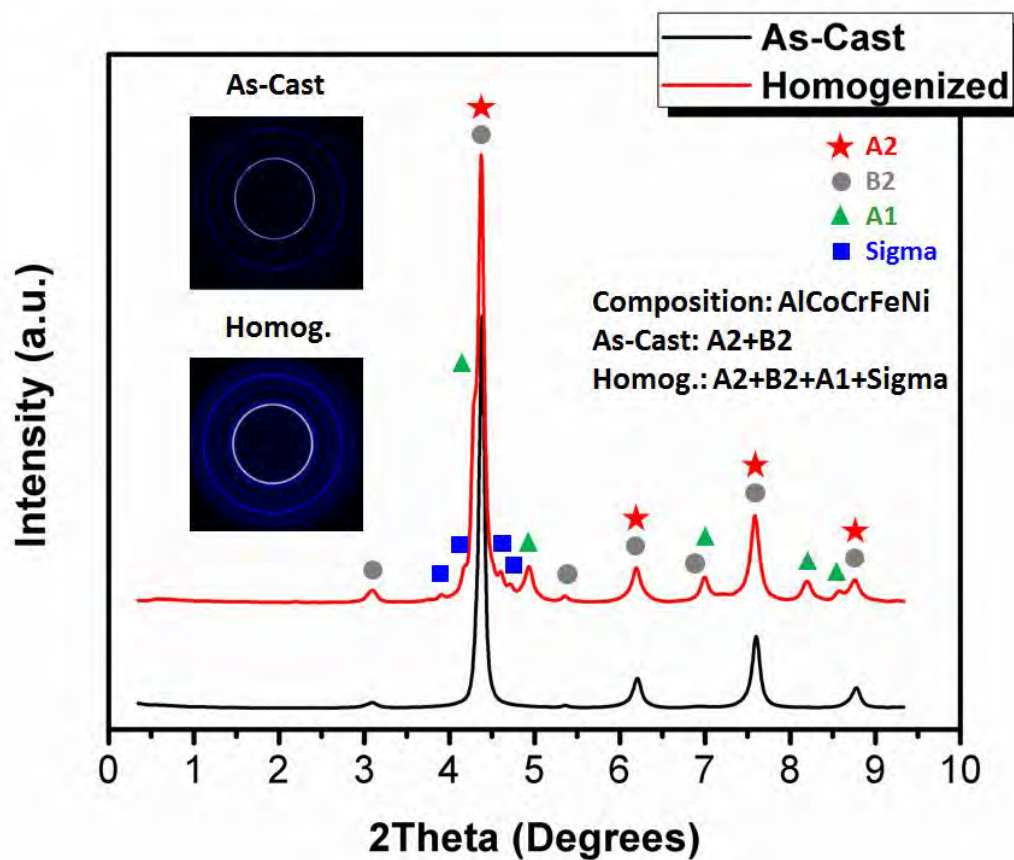


Figure 53. The high-energy synchrotron X-ray diffraction patterns of as-cast and homogenized conditions. The identified phases are shown in the legend. For the Sigma (σ) phase, the following lattice parameters were used: $a = 8.800$ Å, $c = 4.544$ Å. Two insets show the diffraction rings for as-cast and homogenized conditions, corresponding to the synchrotron X-ray diffraction pattern.

4.3.4. Mechanical Behavior

Figure 54 shows the engineering stress-strain curves of the AlCoCrFeNi alloy in both the as-cast (AlCoCrFeNi-AC) and homogenized (AlCoCrFeNi-HP) conditions for tensile testing at 700 °C. The values of the elongation to fracture (ε), yield strength (σ_y), ultimate tensile strength (σ_{UTS}), and specific strength (σ_{UTS}/ρ) of the samples are given in

Table 13. The value of σ_y for the as-cast and heat-treated alloy are 395 MPa and 295 MPa, respectively. A noticeable increase in tensile elongation occurs after the heat treatment: the elongation increases from 1.0 % for as-cast samples to 11.7 % for heat-treated samples. The values of σ_{UTS} for as-cast (400 MPa) and homogenized (393 MPa) conditions are comparable and may remain within the experimental error. For comparison, the tensile properties of the reported HEAs and conventional structural materials at 700 °C are also listed in

Table 13. Compared to others, the present alloy exhibits the relatively high σ_y , σ_{UTS} , and plastic deformation.

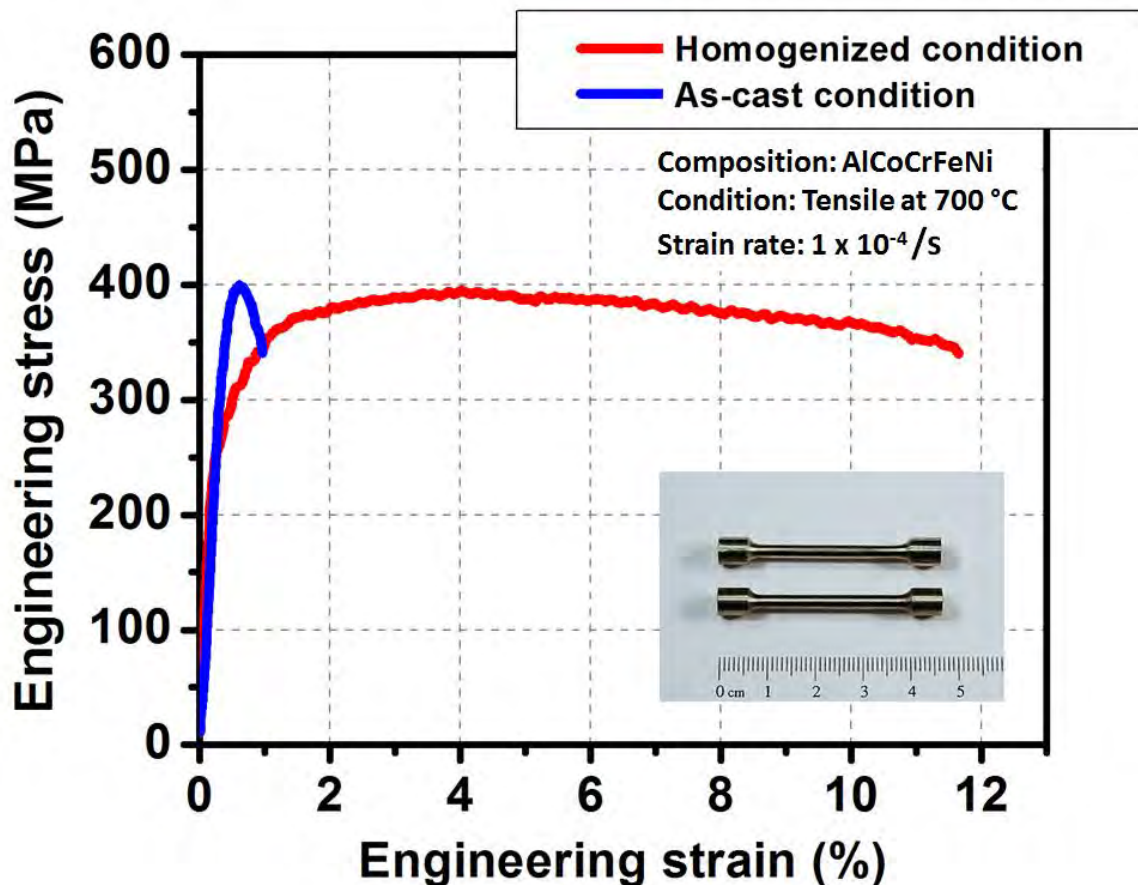


Figure 54. The tensile engineering stress-strain curves of the AlCoCrFeNi alloy, both in as-cast (AlCoCrFeNi-AC) and homogenized (AlCoCrFeNi-HP) conditions, at the temperature of 700 °C. The inserted figure illustrates the cylindrical dog-boned sub-size specimens for tensile tests.

Table 13. Tensile properties at 700 °C for AlCoCrFeNi-AC, AlCoCrFeNi-HP, and some other high-temperature structural materials (all of these data were tested in tension at 700 °C): elongation to fracture (ε), yield strength (σ_y), ultimate tensile strength (σ_{UTS}), and specific strength (σ_{UTS}/ρ). Densities of all materials are also listed. Note that density (ρ) values of the present work (AlCoCrFeNi-AC and AlCoCrFeNi-HP) were measured with a helium pycnometer, while density values of other HEAs are calculated by the theoretical density of a disordered solid solution [75].

Materials	ε (%)	σ_y (MPa)	σ_{UTS} (MPa)	σ_{UTS}/ρ [MPa/(g/cm³)]	ρ (g/cm³)
AlCoCrFeNi-AC (This Work)	1.0	395	400	57.1	7.0
AlCoCrFeNi-HP (This Work)	11.7	295	393	56.1	7.0
AlCoCrCuFeNi As-Cast [99]	4.7	350	360	50.7	7.1
AlCoCrCuFeNi Forged [99]	63	63	91	12.8	7.1
Al _{0.5} CoCrCuFeNi As-Rolled [103]	5.0	180	185	24.3	7.6
Al _{0.5} CoCrCuFeNi As-Annealed [103]	12	160	180	23.7	7.6
Duplex Stainless Steel [126]	2.4	329	366	46.9	7.8
304 Stainless Steel [126]	9.1	179	248	31.8	7.8
Ni-Based Inconel 690 [127]	26	150	478	53.7	8.9
ODS Steel 0.3 % Yttria [128]	11	210	272	34.9	7.8
Intermetallics FeAl 787 [129]	18	345	350	64.8	5.4

4.3.5. Thermodynamic Properties and Phase Equilibrium

Figure 55a presents the calculated solidification path for the AlCoCrFeNi alloy by the Scheil model [123], which indicates that the primary solidified phase is B2. Then the A2+B2 phase will form with decreasing temperature. According to the simulation shown in Figure 55a, only 7 % volume fraction of the liquid is consumed to form the primary B2, and the next

20 % volume fraction of the liquid forms A2+B2 mixture phases. Then, the rest of the liquid solidifies into A2+B2+A1 structures. Furthermore, the temperature drops less than 15 °C (1,189 °C to 1,175 °C) for the A2+B2+A1 mixture to finish solidification. The calculated results (Figure 55a) are very consistent with the experimental ones: primary-solidified dendrites consist of A2+B2 phases, while secondary-solidified interdendrites are composed of A2+B2+A1 phases.

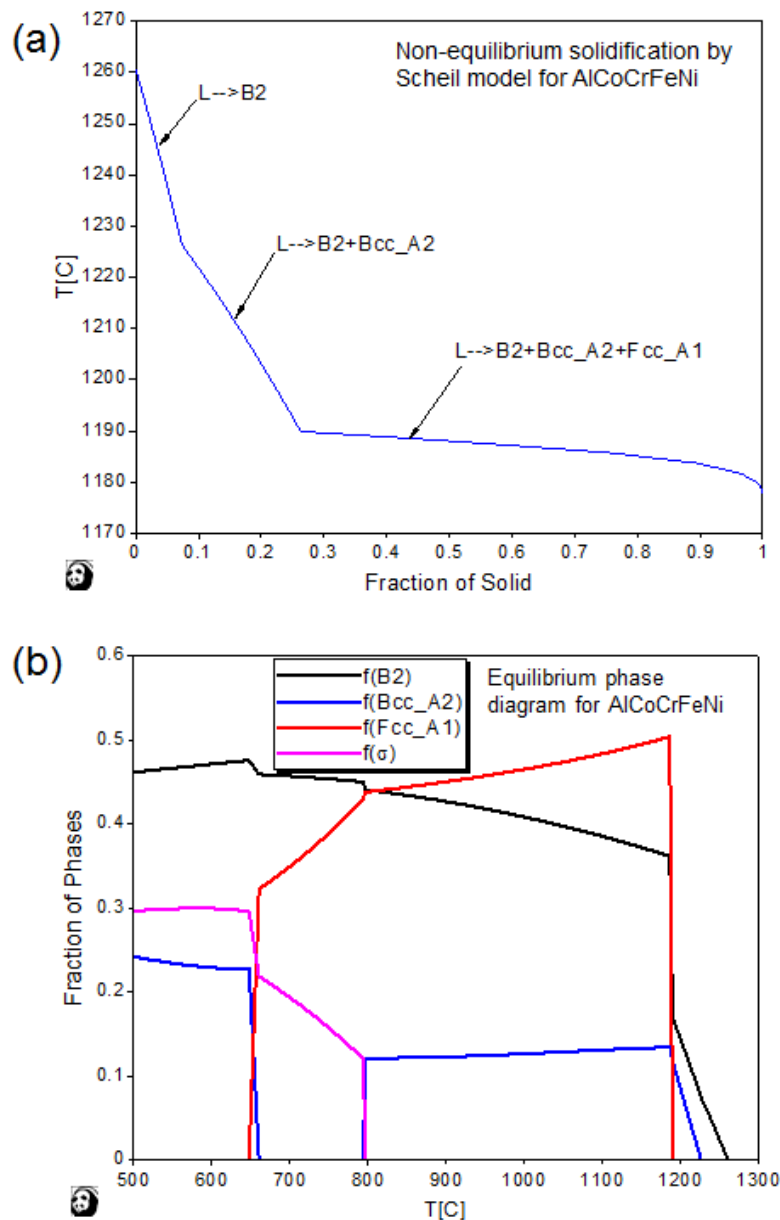


Figure 55. Thermodynamics modeling of (a) non-equilibrium solidification (fast cooling) by Scheil model [123] and (b) an equilibrium phase diagram

An equilibrium line calculation is also performed for the AlCoCrFeNi alloy, as shown in Figure 55b. All four phases, A2+B2+A1+ σ , are all presented in the equilibrium phase

diagram. As exhibited in the calculation, the A1 phase is in equilibrium with the A2 phase after the heat treatment, which is consistent with the experimental data in the present work and those in the literature [96, 100]. The calculated volume fractions of A2 and B2 are similar to the experimental results, while those of A1 and σ are different from the experimental results (Figure 55b and Table 12). Note that the σ phase does form in the temperature range of 460 - 800 °C (Figure 55b), and it is also observed in the AlCoCrFeNi-HP microstructure (Figure 51). However, AlCoCrFeNi-HP was annealed beyond the thermodynamically-predicted temperature range (460 - 800 °C). Several possible reasons are proposed in Section 5.2.

Overall, the thermodynamics prediction, presented in Figure 55, agree qualitatively with the experimental observation in this investigation. The validity of thermodynamic modeling and differences between modeling and experimental results are discussed in Section 5.2.

4.4. Discussion

4.4.1. Reasons for the Improvement of Ductility

The present work shows a significant effect of homogenization heat treatment on the microstructure and tensile properties of the AlCoCrFeNi HEA. Most importantly, the number and amount of phases increase and the tensile elongation at 700 °C increases from 1.0 % to 11.7 %. How the high-temperature properties of HEAs relate to those of other structural materials and how they depend on heat-treatment conditions and compositions are shown in

Table 13 and Figure 56. For example, the tensile behavior of AlCoCrCuFeNi HEA in as-cast and forged conditions are very different: from high strength with limited elongation to low strength with decent elongation. The tensile behavior of Al_{0.5}CoCrCuFeNi HEA in rolled and annealed condition have similar phenomenon. This trend indicates that proper heat treatments can be applied to HEA system by changing microstructures and tailoring properties. This is also exactly the same situation in the present study. Compared to the AlCoCrFeNi-AC alloy, the AlCoCrFeNi-HP alloy exhibits higher combined properties, such as elongation and plastic deformation.

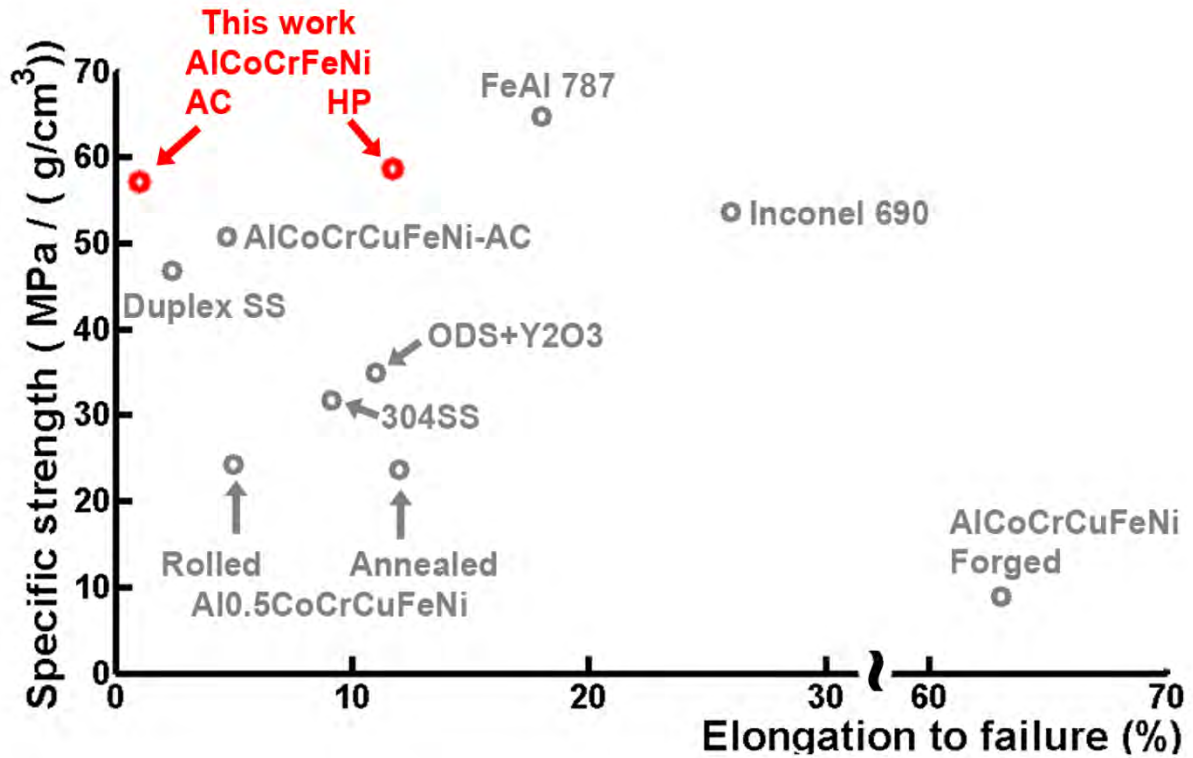


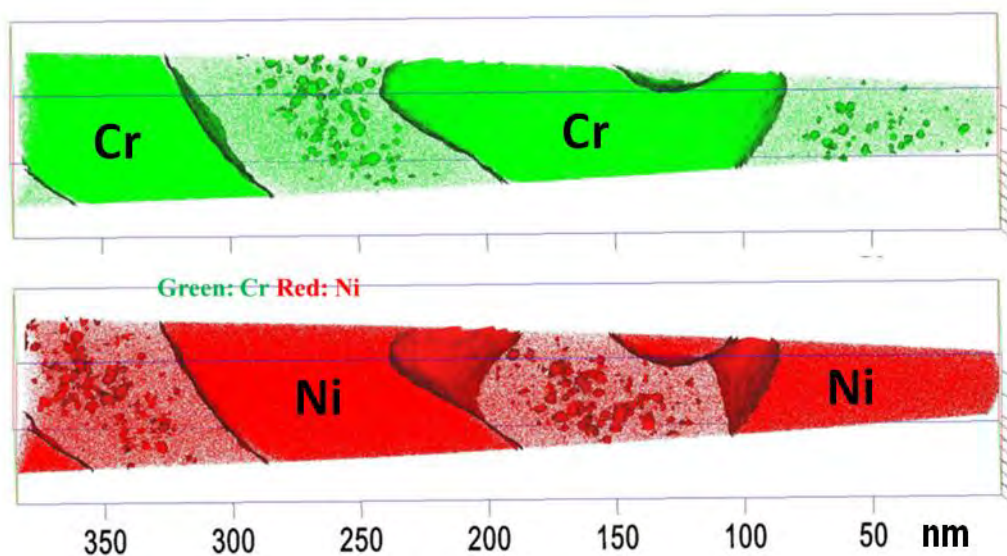
Figure 56. A scatter plot showing the specific strengths and elongations to failure of the AlCoCrFeNi-AC and AlCoCrFeNi-HP, and other high-temperature structural materials at 700 °C [99, 103, 126-134]. Compared to conventional structural alloys, the AlCoCrFeNi-HP has a comparable combination of mechanical properties at elevated temperatures

The size scales of the microstructures are very different in two conditions (as-cast and homogenized). The AlCoCrFeNi-AC alloy shows 50 - 100 nm lamella of A2+B2 phases. Dislocation motion through these finely-spaced interfaces is very difficult. Similarly, TiAl-based alloys also have very limited tensile ductility at room temperature because of their fully-lamellar structures ($\alpha_2+\gamma$) generally observed in cast conditions [135]. However, the brittleness even up to 700 °C in the AlCoCrFeNi-AC material is probably due to the difficulty of forcing dislocation motion through the alternating thin lamella of different crystal structures.

The lamellar structure explains the poor ductility. Our TEM results indicate that the boundary planes between the A2 and B2 lamellas are often of 100 plane with $\langle 010 \rangle$ in the long directions of the lamella. The slip systems active in these highly alloyed phases are unknown, but based upon extrapolations from the knowledge of B2-NiAl and A2-Fe, the dominant slip planes are likely 110-type. Burger's vectors are similarly unknown, but a $\langle 110 \rangle$ in B2 and $a/2\langle 111 \rangle$ in A2 are likely and assumed here. Atom probe tomography (Figure 57a) indicates that the lamellas contain high densities of fine precipitates of the opposite phase. A HAADF image from STEM with a sketch of AlCoCrFeNi-AC specimen shows an A2+B2 lamellar structure at the atomic level (Figure 57b). Both the lamella boundaries and the fine

precipitates likely act as strengthening obstacles to reduce the ductility of the material. For example, if a lamella is 50 nm wide and oriented with $\langle 100 \rangle$ in its long direction, then 110-plane dislocation will have only ~ 50 or ~ 70 nm of the distance from one edge of the lamella to the other (Figure 57c). This distance will be further interrupted by the fine particles, which will require dislocation climb, cross slip, cutting, or bowing, to bypass. The assumed $a\langle 110 \rangle$ B2 dislocations will not easily transfer into the assumed $a/2\langle 111 \rangle$ burger's vector in A2, and vice-versa. Thus, dislocations will probably have to climb, cross-slip, or bow around the nanoparticles, rather than cut the particles. Those dislocations that do pass through the particle forest will then probably pileup at the lamellar interface, again due to the difficulty of the shear transfer from the $a\langle 110 \rangle_{B2}$ to $a/2\langle 111 \rangle_{A2}$ burger's vectors. All of these factors together will result in the increased shear stress required to drive dislocations through the structure, and, therefore, reduced ductility.

(a)



(b)

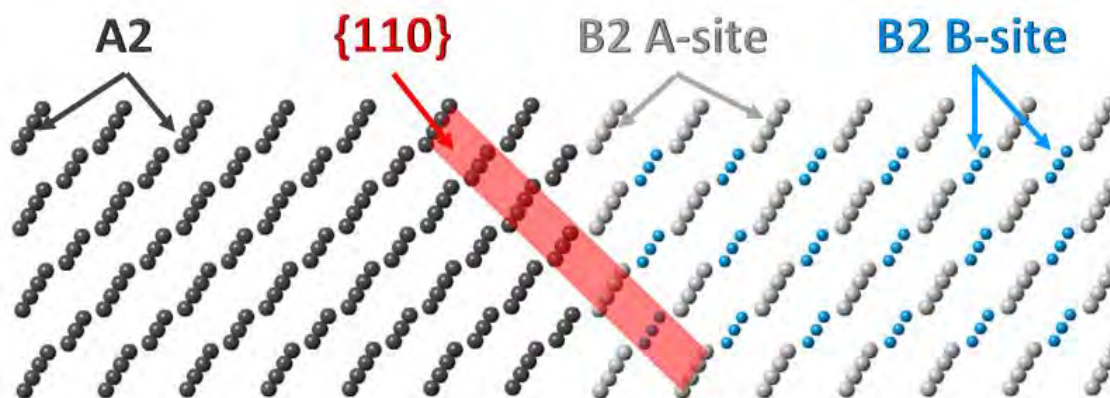


Figure 57. (a) Atom probe tomography (APT) of the AlCoCrFeNi-AC alloy, and (b) corresponding sketch of different atom clusters, such as A2 and B2

In the homogenized condition instead, due to breaking up the A2+B2 lamella into larger domains (Figure 52), giving the dislocations longer glide-lengths before hitting an obstacle may be the main reason for the improvement of ductility but lower yield strength (Figure 54 and

Table 13). Furthermore, the other important reason may be the occurrence of the relatively-ductile A1 phase free of precipitates. Our nanoindentation results revealed that the A1 phase has a hardness of 4.3 ± 0.2 GPa, which is less than half of the B2 phase with a hardness of 8.9 ± 0.4 GPa at room temperature. Liu et al. also confirmed that the A1 phase has a lower yield strength than the B2 matrix in the $\text{Al}_{0.8}\text{CoCrCuFeNi}$ HEA at room temperature [136]. Generally, a phase with a lower hardness and a lower yield strength will possess a higher ductility, even more at elevated temperatures. This trend may also happen in our case, which means that the appearance of a large amount of a relatively ductile A1 phase along grain boundaries in the homogenized condition contributes to the improvement of the ductility, compared with the as-cast condition with a very few amount of A1 nanoprecipitates. In addition, the thermal treatment (HIP+homogenization) after casting may reduce defects produced by casting and relieve residual stresses during fast-cooling drop-casting.

4.4.2. Validity of Thermodynamic Modeling

Based on the thermodynamic modeling for the as-cast condition, the A1 phase only forms over less than a 15 °C interval (1,189 °C to 1,175 °C in Figure 55a). Thus, the A1 phase may not be able to form or only a very small amount of A1 forms due to the high cooling rate (non-equilibrium) of the alloy preparation using the drop-casting method. There is a very small amount (less than 1-2 %) of fine precipitates of an additional phase, which has an A1 structure and is enriched with Co (Figure 48d), which is consistent with our Scheil modeling. Also, the simulation shows that the structure is a mixture of the A2+B2 owing to this special

solidification (note that NiAl-rich dendrites solidified first, and then NiAl-poor interdendritic regions formed), which is consistent with the experimental observation for the microstructures of AlCoCrFeNi-AC alloy in the present work. Note that the volume fraction of the A1 phase is $\sim 50\%$ (Figure 55b), and we may not be able to obtain this amount, since the AlCoCrFeNi-HP alloy may not yet reach equilibrium due to the sluggish diffusion of elements in HEAs and the short annealing period (only 50 hours in the present study).

There is one main difference between thermodynamic-modeling predictions and microstructural characterizations. It is the presence of σ phases in the homogenized condition. As mentioned previously, the σ phase is observed in the microstructure of the AlCoCrFeNi-HP alloy, which was annealed at 1,150 °C for 50 hours, beyond the thermodynamically-predicted existing temperature range (460 - 800 °C). There are two possible reasons for this discrepancy. One reason may be due to unreasonable thermodynamic parameters for the σ phase in the present thermodynamic model. The other reason may result from the localization of certain alloying elements within this alloy forming the σ phase. For example, a certain amount of Co can improve the stability of the σ phase at higher temperatures, up to 1,283 °C (such as the binary Co-Cr σ phase [137, 138]), which is higher than the annealing temperature of 1,150 °C. Indeed, some amounts (24 at. %) of Co are observed in the σ phase, as presented in Figure 51(d) and shown in Table 11. Of course, it is also likely that the σ phase precipitated during slow furnace cooling (10 °C/min). Chou et al. [100] did not observe the σ phase at 500 °C and 550 °C, which is not surprising, since the precipitation is a diffusion-controlled process, and a certain amount of phases are necessary for the phase identification by the regular lab X-ray diffraction.

Further experimental and thermodynamical investigations on these issues will be carried out in future studies. Specifically, systematic phase-transformation studies for the AlCoCrFeNi alloy will be necessary, especially in the solid state, for the quantitative comparison. As mentioned previously, the current Al-Co-Cr-Fe-Ni database was developed using the available experimental data of the 10 constituent binaries and 10 constituent ternaries. This database needs further validation by the 5-component alloys.

4.4.3. A2+B2 Nano-lamellar Structure in HEA Systems

If we define BCC HEA as a single-phase A2 (a disordered BCC solid solution) structure with no elemental segregation, many reported single-BCC HEAs with one lattice parameter may fail to meet this criterion. They are usually elemental-segregation dendritical structures (dendrites and interdendrites) [74, 75, 139, 140], and people tend to call them as element-rich, such as NiAl-rich in 3d-transition-metal-based HEAs, and TaW-rich in refractory HEAs. Actually, those alloys may be composed of A2 and B2 phases. NiAl-type B2 structure in HEA systems are usually very stable due to its very negative enthalpy [57]. Once B2 phases formed during cast processing, solidified microstructures were difficult to be

homogenized through regular heat treatments (compare Figure 47 with Figure 51). If a single-phase A2 HEA is going to be identified, only an X-ray diffraction pattern with no (100) superlattice peak is not enough. Formed by the eutectic reaction during solidification (Figure 55a), A2 and B2 could have very small lattice parameter mismatch [57]. This trend may be the reason why only one lattice parameter can be found via X-ray diffraction pattern [74, 75, 139, 140]. This feature is also very common in the Ni-based superalloy (γ and γ') and FCC HEA systems [73, 94, 124]. To the current authors' knowledge, single-phase FCC or BCC HEAs can only be found in a few publications [141-144].

In the present study, the A2+B2 nano-lamellar structures also coexist in both NiAl-rich dendrites and NiAl-poor interdendritic regions in the as-cast condition, even though only one lattice parameter can be found via synchrotron X-ray diffraction pattern (as-cast in Figure 53). Furthermore, the NiAl-rich dendrite regions are enriched with the B2 phase, and the NiAl-poor interdendrite regions are enriched with the A2 phase. This trend has been confirmed by SEM with EDS/EBSD and TEM studies, as shown in Section 4.1. To further investigate this trend, the selective etching technique [145-147] was applied. As shown in Figure 58, nanoprecipitates with 50-100 nm were etched away both in NiAl-rich dendrital and NiAl-poor interdendrital regions, and yet another kind of line-shape nanoprecipitates might be only found in NiAl-poor regions. The selectively-etched morphology (Figure 58) quite agrees with the previous TEM results (Figure 48): etched-away nanoprecipitates are the Cr-rich phase with an A2 structure; etched-away line-shape nanoprecipitates are the Co-rich phase with an A1 structure; and remaining are the NiAl-rich matrix with a B2 structure. This trend also agrees the original function of the selective etchant (Kalling's No.2) in steel which does attack ferrite (A2 structure) and slightly attack the austenite (A1 structure) [148]. Furthermore, based on our thermodynamic calculation (Figure 55a), A2+B2 tend to be firstly solidified together to form dendrites (NiAl-rich regions in this study), and then A2+B2+A1 are solidified to form interdendritically (NiAl-poor regions in this study) during fast cooling. This feature may be the reason why line-shape nanoprecipitates with an A1 structure can only be found in NiAl-poor interdendritic regions (Figure 58). Thus, we have many indications that both dendrites and interdendritic regions are fine A2+B2 nano-lamellar structure (NiAl-rich dendrites enriched in B2, and NiAl-poor interdendrites enriched in A2), while another kind of line-shape nanoprecipitates with A1 structure only exist in NiAl-poor interdendritic regions.

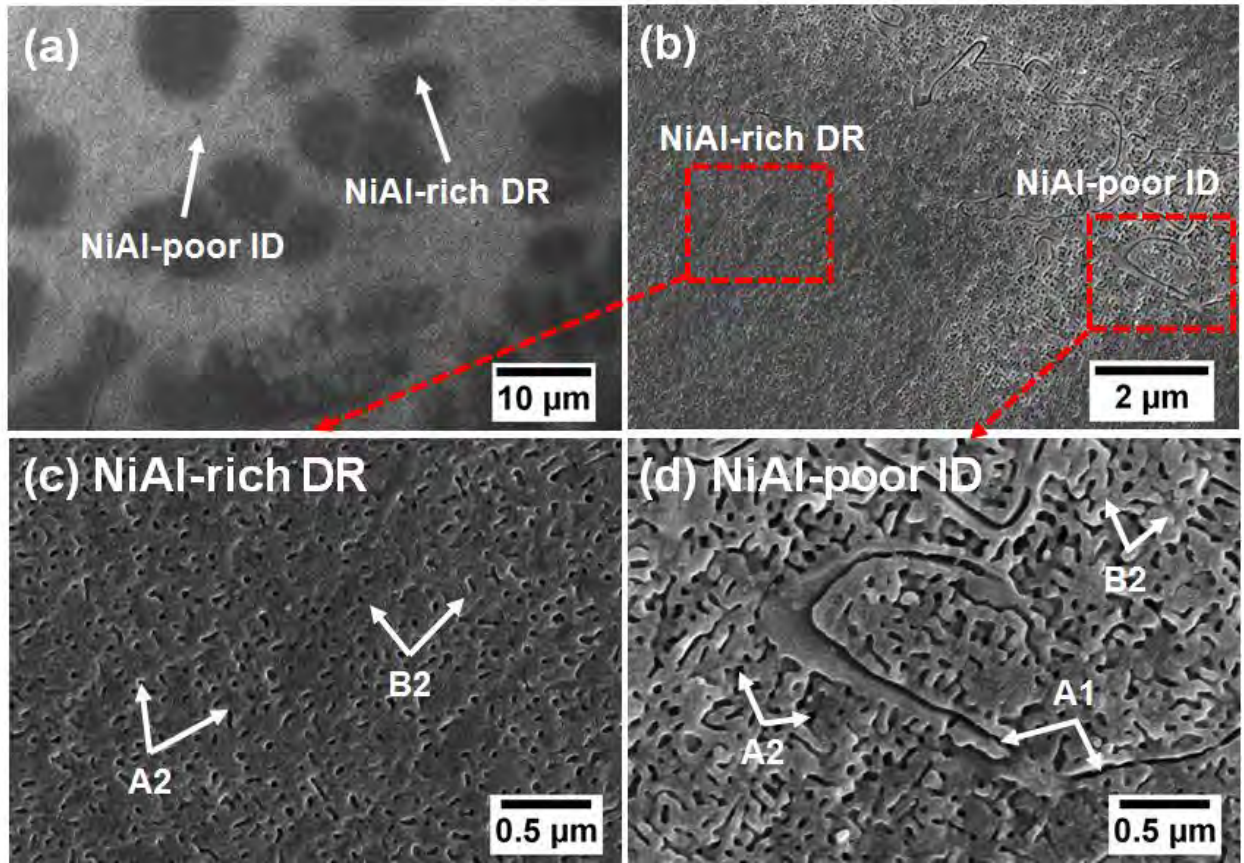


Figure 58. SEM images of the AlCoCrFeNi-AC alloy after applying selected etching using Kalling's No. 2.

Similar phenomena are also found in AlCoCrFeNi-HP. As presented in Figure 59, Cr-rich nanoprecipitates with an A2 structure are embedded in the NiAl-rich B2 matrix, while CoCrFe-rich A1 phases are free of precipitates. Note that the structure type of a pure Cr element is A2, which further confirm our hypothesis.

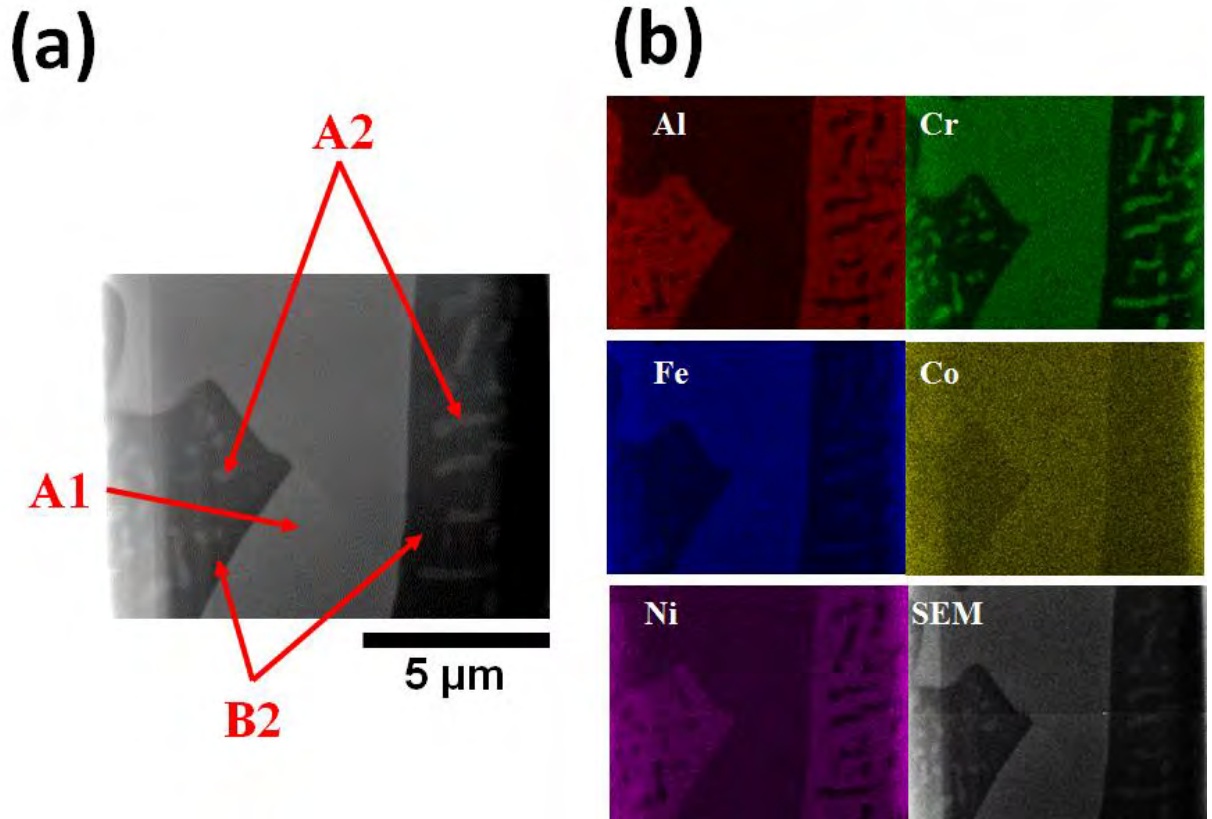


Figure 59. A high-resolution SEM image of a focused ion beam (FIB) sample in the AlCoCrFeNi-HP alloy. The EDS maps are presented in (b).

Above all, the microstructures and mechanical behavior of one alloy, AlCoCrFeNi, have been carefully studied in two conditions (as-cast and homogenized), as summarized in Figure 60. As confirmed by both experiments (SEM/EDS, EBSD, TEM/STEM, APT, and Synchrotron) and simulations (CALPHAD), the homogenization treatment results in phase evolution: from two major phases (A2+B2) in the as-cast condition to four major phases (A2+B2+A1+ σ) in the homogenized condition. Moreover, both NiAl-rich dendrites and NiAl-poor interdendrites have a fine A2+B2 nano-lamellar structure, but different volume fractions of A2 and B2. The very different microstructures in the two conditions exhibits similar σ_{UTS} but a noticeable increase in the tensile ductility after the heat treatment (HIP and homogenized).

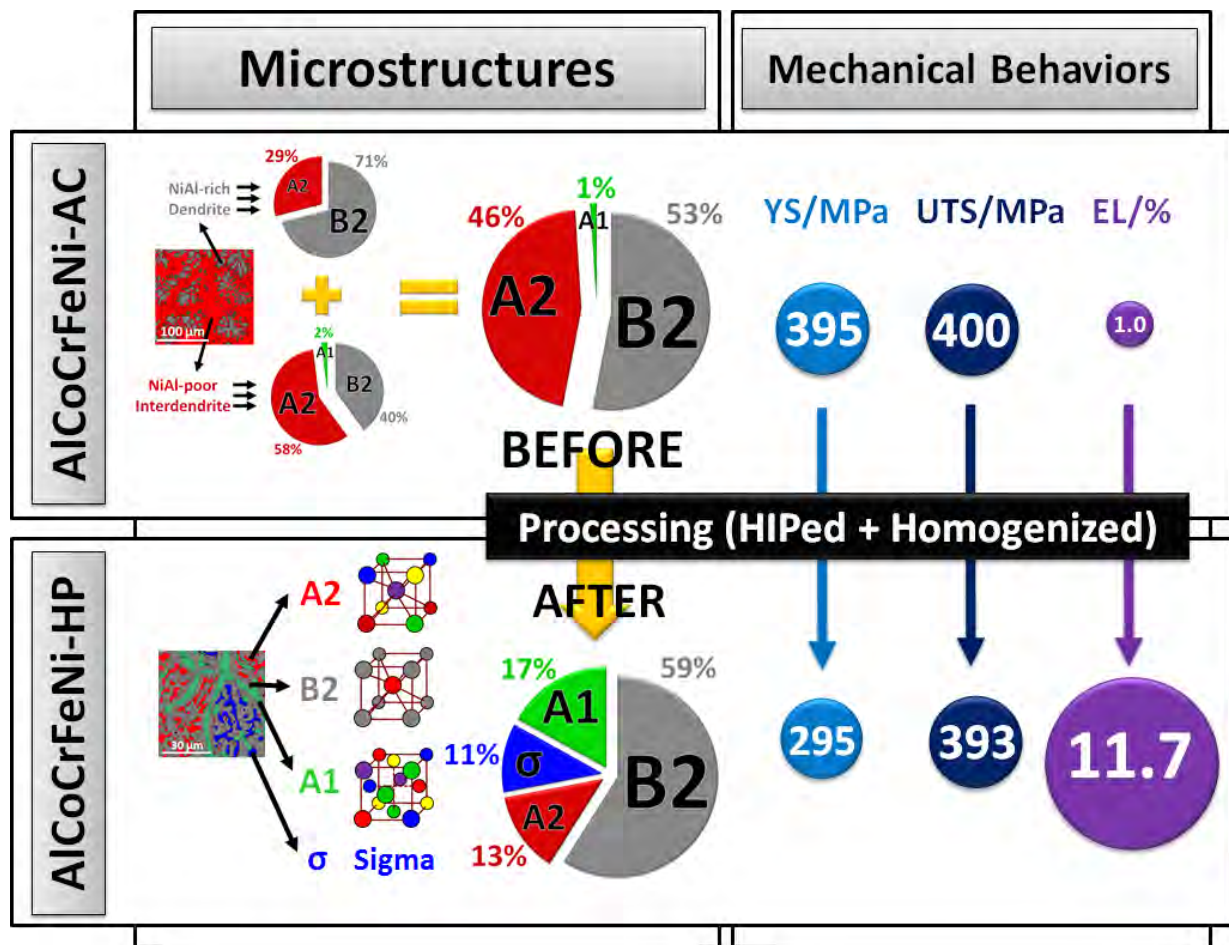


Figure 60. A summary cartoon of all major results in the present study

4.5. Summary and Conclusions

In summary, we discuss how as-cast and homogenized phases in HEAs can be identified, what phases are usually found in the as-cast and homogenized conditions, and what the thermodynamics and kinetics of phase transformations are in the AlCoCrFeNi HEA, as shown in a summary cartoon of Figure 60.

- (1) Using SEM/EDS, EBSD, STEM and high-energy synchrotron X-ray diffraction, the microstructures of the AlCoCrFeNi-AC alloy are identified to have clear intra-granular dendritic structures containing two regions, NiAl-rich dendrites and NiAl-poor interdendritic regions. The TEM/STEM and the selective etching technique further confirm that both NiAl-rich and NiAl-poor regions have a fine A2+B2 nano-lamellar structure. The difference between two regions is that the NiAl-rich dendrite regions are enriched with the B2 phase, while the NiAl-poor interdendrite regions are enriched with the A2 phase as well as a small amount of A1 nanoprecipitates (less than 1-2 %).

- (2) Four phases, A2, B2, A1, and σ phases, are observed in the AlCoCrFeNi-HP. A2 nanoprecipitates embedded in the B2 matrix are also found in the homogenized condition, while blocky wall-like A1 phases along boundaries are identified and free of precipitates.
- (3) A noticeable increase in the tensile ductility occurs after the HIP and homogenized treatment. During tensile testing at 700 °C, the elongation of the homogenized alloy is 11.7 %, while the as-cast alloy show the elongation of only 1.0 %. The ultimate tensile strength at 700 °C is almost unaffected by the heat treatment, 400 MPa and 393 MPa, respectively.
- (4) The reason for the limited elongation of the AlCoCrFeNi-AC alloy may be that dislocation motion through these finely-spaced interfaces (50-100 nm) is very difficult, resulting in higher yield strength. The improvement of ductility for the AlCoCrFeNi-HP alloy may be due to breaking up the A2+B2 lamella into larger domains, the occurrence of the relatively ductile FCC phase, reduced casting defects, and relieved residual stress.
- (5) The CALPHAD thermodynamic modeling, including the solidification path and the phase map, are well consistent with the experimental data.

The authors believe that this study will pave the way for the characterization and optimization of the AlCoCrFeNi alloy and the microstructures of the similar HEAs system. Meanwhile, it is the authors' hope that this study will draw more attention of scientists to research homogenized HEAs with balanced mechanical properties, perhaps with multiple phases, rather than the only pursuit of single-phase solid-solution HEAs, which is also emphasized by Miracle et al. [85]. It even provides support toward the composition design of HEAs based on the composition-structure-property relationship. The fundamental understanding of microstructures will lay down the foundation for the discovery of new HEAs with improved materials properties in extreme environments. HEAs as a new class of advanced materials with competitive high strengths at elevated temperatures and with reasonable ductility may become the next-generation structural materials. The development of such novel materials will bring significant impacts on some extreme environmental engineering for wide applications.

References

- [1] Yeh JW, Chen SK, Lin SJ, Gan JY, Chin TS, Shun TT, et al. Nanostructured high-entropy alloys with multiple principal elements: novel alloy design concepts and outcomes. *Adv Eng Mater.* 2004;6:299-303.
- [2] Cantor B, Kim KB, Warren PJ. Novel multicomponent amorphous alloys. In: Ma E, Atzmon M, Koch CC, editors. *Metastable, Mechanically Alloyed and Nanocrystalline Materials*. Zurich-Uetikon: Trans Tech Publications Ltd; 2002. p. 27-31.
- [3] Zhou YJ, Zhang Y, Wang YL, Chen GL. Solid solution alloys of AlCoCrFeNiTi_x with excellent room-temperature mechanical properties. *Appl Phys Lett.* 2007;90.
- [4] Gludovatz B, Hohenwarter A, Catoor D, Chang EH, George EP, Ritchie RO. A fracture-resistant high-entropy alloy for cryogenic applications. *Science.* 2014;345:1153-8.
- [5] Zhang Y, Zuo TT, Tang Z, Gao MC, Dahmen KA, Liaw PK, et al. Microstructures and properties of high-entropy alloys. *Progress in Materials Science.* 2014;61:1-93.
- [6] Egami T, Guo W, Rack PD, Nagase T. Irradiation resistance of multicomponent alloys. *Metall and Mat Trans A.* 2014;45:180-3.
- [7] Wu Z, Bei H, Pharr GM, George EP. Temperature dependence of the mechanical properties of equiatomic solid solution alloys with face-centered cubic crystal structures. *Acta Mater.* 2014;81:428-41.
- [8] Was GS. *Fundamentals of Radiation Materials Science: Metals and Alloys*. New York: Springer; 2007.
- [9] Zinkle SJ, Busby JT. Structural materials for fission and fusion energy. *Mater Today.* 2009;12:12-9.
- [10] de la Rubia TD, Averback RS, Hsieh H, Benedek R. Molecular dynamics simulation of displacement in Cu and Ni - Thermal spike behavior. *J Mater Res.* 1989;4:579-86.
- [11] Bacon DJ, Calder AF, Harder JM, Wooding SJ. Computer simulation of low-energy displacement events in pure bcc and hcp metals. *J Nucl Mater.* 1993;205:52-8.
- [12] Osetsky YN, Serra A, Singh BN, Golubov SI. Structure and properties of clusters of self-interstitial atoms in fcc copper and bcc iron. *Philos Mag A-Phys Condens Matter Struct Defect Mech Prop.* 2000;80:2131-57.
- [13] Calder AF, Bacon DJ. A molecular dynamics study of displacement cascades in alpha iron. *J Nucl Mater.* 1993;207:25-45.
- [14] Soneda N, de la Rubia TD. Defect production, annealing kinetics and damage evolution in alpha-Fe: an atomic-scale computer simulation. *Philos Mag A-Phys Condens Matter Struct Defect Mech Prop.* 1998;78:995-1019.
- [15] Stoller RE, Odette GR, Wirth BD. Primary damage formation in bcc iron. *J Nucl Mater.* 1997;251:49-60.
- [16] Stoller RE. The role of cascade energy and temperature in primary defect formation in iron. *J Nucl Mater.* 2000;276:22-32.

- [17] Calder AF, Bacon DJ, Barashev AV, Osetsky YN. Effect of mass of the primary knock-on atom on displacement cascade debris in alpha-iron. *Philos Mag Lett*. 2008;88:43-53.
- [18] Selby AP, Xu DH, Juslin N, Capps NA, Wirth BD. Primary defect production by high energy displacement cascades in molybdenum. *J Nucl Mater*. 2013;437:19-23.
- [19] Morishita K, de la Rubia TD. A molecular dynamics simulation study of displacement cascades in vanadium. *J Nucl Mater*. 1999;271:35-40.
- [20] Wooding SJ, Bacon DJ, Phythian WJ. A computer-simulation study of displacement cascades in alpha-titanium. *Philos Mag A-Phys Condens Matter Struct Defect Mech Prop*. 1995;72:1261-79.
- [21] Wooding SJ, Bacon DJ. A molecular dynamics study of displacement cascades in alpha-zirconium. *Philos Mag A-Phys Condens Matter Struct Defect Mech Prop*. 1997;76:1033-51.
- [22] Wooding SJ, Howe LM, Gao F, Calder AF, Bacon DJ. A molecular dynamics study of high-energy displacement cascades in alpha-zirconium. *J Nucl Mater*. 1998;254:191-204.
- [23] Ackland GJ, Bacon DJ, Calder AF, Harry T. Computer simulation of point defect properties in dilute Fe-Cu alloy using a many-body interatomic potential. *Philos Mag A-Phys Condens Matter Struct Defect Mech Prop*. 1997;75:713-32.
- [24] Gao F, Bacon DJ. Point-defect and threshold displacement energies in Ni₃Al .1. Point-defect properties. *Philos Mag A-Phys Condens Matter Struct Defect Mech Prop*. 1993;67:275-88.
- [25] Gao F, Bacon DJ. Molecular dynamics study of displacement cascades in Ni₃Al.1. General features and defect production efficiency. *Philos Mag A-Phys Condens Matter Struct Defect Mech Prop*. 1995;71:43-64.
- [26] Deng HF, Bacon DJ. Molecular-dynamics study of displacement cascades in Cu-Au solid solutions. *Physical Review B*. 1996;53:11376-87.
- [27] Zhu HL, Lam NQ. Displacement cascades in the ordered compound CuTi studied by molecular-dynamics simulations. *Nucl Instrum Methods Phys Res Sect B-Beam Interact Mater Atoms*. 1995;95:25-33.
- [28] Daw MS, Baskes MI. Semiempirical, Quantum Mechanical Calculation of Hydrogen Embrittlement in Metals. *Phys Rev Lett*. 1983;50:1285-8.
- [29] Daw MS, Baskes MI. Embedded-atom method - derivation and application to impurities, surfaces, and other defects in metals. *Physical Review B*. 1984;29:6443-53.
- [30] Baskes MI. Modified embedded-atom potentials for cubic materials and impurities. *Physical Review B*. 1992;46:2727-42.
- [31] Finnis MW, Sinclair JE. A simple empirical N-body potential for transition-metals. *Philos Mag A-Phys Condens Matter Struct Defect Mech Prop*. 1984;50:45-55.
- [32] Kinchin GH, Pease RS. The displacement of atoms in solids by radiation Reports on Progress in Physics. 1955;18:1.

- [33] Norgett MJ, Robinson MT, Torrens IM. A proposed method of calculating displacement dose rates. *Nucl Eng Des.* 1975;33:50-4.
- [34] Wolfer WG. Fundamental properties of defects in metals. In: Konings R, Allen TR, Stoller RE, Yamanaka S, editors. *Comprehensive Nuclear Materials*. Amsterdam: Elsevier Ltd.; 2012.
- [35] Johnson RA. Interstitials and vacancies in α Iron. *Physical Review.* 1964;134:A1329-A36.
- [36] Willaime F, Fu CC, Marinica MC, Dalla Torre J. Stability and mobility of self-interstitials and small interstitial clusters in alpha-iron: ab initio and empirical potential calculations. *Nucl Instrum Methods Phys Res Sect B-Beam Interact Mater Atoms.* 2005;228:92-9.
- [37] Guo W, Iwashita T, Egami T. Universal local strain in solid-state amorphization: The atomic size effect in binary alloys. *Acta Mater.* 2014;68:229-37.
- [38] Guo W, Dmowski W, Noh JY, Rack P, Liaw PK, Egami T. Local Atomic Structure of a High-Entropy Alloy: An X-Ray and Neutron Scattering Study. *Metall Mater Trans A-Phys Metall Mater Sci.* 2013;44A:1994-7.
- [39] Nicholson DM, Ojha M, Egami T. First-principles local stress in crystalline and amorphous metals. *Journal of Physics: Condensed Matter.* 2013;25:435505.
- [40] Tian F, Varga LK, Chen N, Delczeg L, Vitos L. Ab initio investigation of high-entropy alloys of 3d elements. *Physical Review B.* 2013;87:075144.
- [41] Malerba L. Molecular dynamics simulation of displacement cascades in alpha-Fe: A critical review. *J Nucl Mater.* 2006;351:28-38.
- [42] Calder AF, Bacon DJ, Barashev AV, Osetsky YN. On the origin of large interstitial clusters in displacement cascades. *Philos Mag.* 2010;90:863-84.
- [43] Eshelby JD. The determination of the elastic field of an ellipsoidal inclusion, and related problems. *Proceedings of the Royal Society of London Series a-Mathematical and Physical Sciences.* 1957;241:376-96.
- [44] Dasgupta R, Gendelman O, Mishra P, Procaccia I, Shor CABZ. Shear localization in three-dimensional amorphous solids. *Phys Rev E.* 2013;88:032401.
- [45] Phythian WJ, Stoller RE, Foreman AJE, Calder AF, Bacon DJ. A comparison of displacement cascades in copper and iron by molecular-dynamics and its application to microstructural evolution. *J Nucl Mater.* 1995;223:245-61.
- [46] Bacon DJ, Calder AF, Gao F, Kapinos VG, Wooding SJ. Computer-simulation of defect production by displacement cascades in metals. *Nucl Instrum Methods Phys Res Sect B-Beam Interact Mater Atoms.* 1995;102:37-46.
- [47] Vitek V. Pair potentials in atomistic computer simulations. *MRS Bull.* 1996;21:20-3.
- [48] Olander DR. Fundamental aspects of nuclear reactor fuel elements: Technical Information Center, Office of Public Affairs, Energy Research and Development Administration; 1976.

- [49] Bai XM, Voter AF, Hoagland RG, Nastasi M, Uberuaga BP. Efficient Annealing of Radiation Damage Near Grain Boundaries via Interstitial Emission. *Science*. 2010;327:1631-4.
- [50] Yamamoto Y, Brady MP, Lu ZP, Maziasz PJ, Liu CT, Pint BA, et al. Creep-Resistant, Al₂O₃-Forming Austenitic Stainless Steels. *Science*. 2007;316:433-6.
- [51] Morris JR, Song XY. The melting lines of model systems calculated from coexistence simulations. *J Chem Phys*. 2002;116:9352-8.
- [52] Morris JR, Wang CZ, Ho KM, Chan CT. Melting line of aluminum from simulations of coexisting phases. *Physical Review B*. 1994;49:3109-15.
- [53] Peng LJ, Morris JR, Aga RS. A parameter-free prediction of simulated crystal nucleation times in the Lennard-Jones system: From the steady-state nucleation to the transient time regime. *J Chem Phys*. 2010;133.
- [54] Steinhardt PJ, Nelson DR, Ronchetti M. Bond-orientational order in liquids and glasses. *Physical Review B*. 1983;28:784-805.
- [55] Xu D. Development of novel binary and multi-component bulk metallic glasses: California Institute of Technology; 2005.
- [56] Yeh JW, Chen SK, Lin SJ, Gan JY, Chin TS, Shun TT, et al. Nanostructured High-Entropy Alloys with Multiple Principal Elements: Novel Alloy Design Concepts and Outcomes. *Adv Eng Mater*. 2004;6:299-303.
- [57] Tang Z, Gao MC, Diao HY, Yang TF, Liu JP, Zuo TT, et al. Aluminum Alloying Effects on Lattice Types, Microstructures, and Mechanical Behavior of High-Entropy Alloys Systems. *Jom-Us*. 2013;65:1848-58.
- [58] Chen YY, Duval T, Hung UD, Yeh JW, Shih HC. Microstructure and electrochemical properties of high entropy alloys—a comparison with type-304 stainless steel. *Corros Sci*. 2005;47:2257-79.
- [59] Hemphill MA, Yuan T, Wang GY, Yeh JW, Tsai CW, Chuang A, et al. Fatigue behavior of Al_{0.5}CoCrCuFeNi high entropy alloys. *Acta Mater*. 2012;60:5723-34.
- [60] Kaufman L, Bernstein H. Computer calculation of phase diagrams with special reference to refractory metals. New York: Academic Press; 1970.
- [61] Chang YA, Chen S, Zhang F, Yan X, Xie F, Schmid-Fetzer R, et al. Phase diagram calculation: past, present and future. *Progress in Materials Science*. 2004;49:313-45.
- [62] Dinsdale AT. SGTE data for pure elements. *Calphad*. 1991;15:317-425.
- [63] Redlich O, Kister A. Algebraic representation of thermodynamic properties and the classification of solutions. *Industrial & Engineering Chemistry*. 1948;40:345-8.
- [64] Ansara I. Comparison of methods for thermodynamic calculation of phase diagrams *International Metals Reviews*. 1979;24:20-53.
- [65] Sundman B, Jansson B, Andersson J. Calphad-computer coupling of phase diagrams and thermochemistry. *Calphad*. 1985;9:153-90.
- [66] Andersson J-O, Guillermet AF, Hillert M, Jansson B, Sundman B. A compound-energy

model of ordering in a phase with sites of different coordination numbers. *Acta metallurgica*. 1986;34:437-45.

[67] Oates WA, Wenzl H. The bond-energy model for ordering in a phase with sites of different coordination numbers. *Calphad-Comput Coupling Ph Diagrams Thermochem*. 1992;16:73-8.

[68] Chen SL, Kao CR, Chang YA. A generalized quasi-chemical model for ordered multicomponent, multi-sublattice intermetallic compounds with anti structure defects. *Intermetallics*. 1995;3:233-42.

[69] Cao W, Chen S-L, Zhang F, Wu K, Yang Y, Chang Y, et al. PANDAT software with PanEngine, PanOptimizer and PanPrecipitation for multi-component phase diagram calculation and materials property simulation. *Calphad*. 2009;33:328-42.

[70] Hari Kumar K, Wollants P. Some guidelines for thermodynamic optimisation of phase diagrams. *Journal of alloys and compounds*. 2001;320:189-98.

[71] Kao Y-F, Chen S-K, Chen T-J, Chu P-C, Yeh J-W, Lin S-J. Electrical, magnetic, and Hall properties of $\text{Al}_x\text{CoCrFeNi}$ high-entropy alloys. *J Alloys Compd*. 2011;509:1607-14.

[72] Lu K. The future of metals. *Science*. 2010;328:319-20.

[73] Cantor B, Chang ITH, Knight P, Vincent AJB. Microstructural development in equiatomic multicomponent alloys. *Mater Sci Eng A*. 2004;375:213-8.

[74] Zhou YJ, Zhang Y, Wang YL, Chen GL. Solid solution alloys of AlCoCrFeNiTi_x with excellent room-temperature mechanical properties. *Appl Phys Lett*. 2007;90:181904.

[75] Senkov ON, Wilks GB, Miracle DB, Chuang CP, Liaw PK. Refractory high-entropy alloys. *Intermetallics*. 2010;18:1758-65.

[76] Zhang Y, Yang X, Liaw PK. Alloy design and properties optimization of high-entropy alloys. *Jom-Us*. 2012;64:830-8.

[77] Otto F, Yang Y, Bei H, George EP. Relative effects of enthalpy and entropy on the phase stability of equiatomic high-entropy alloys. *Acta Mater*. 2013;61:2628-38.

[78] Senkov ON, Senkova SV, Woodward C, Miracle DB. Low-density, refractory multi-principal element alloys of the Cr–Nb–Ti–V–Zr system: Microstructure and phase analysis. *Acta Mater*. 2013;61:1545-57.

[79] Zhu C, Lu ZP, Nieh TG. Incipient plasticity and dislocation nucleation of FeCoCrNiMn high-entropy alloy. *Acta Mater*. 2013;61:2993-3001.

[80] Zhang Y, Zuo T, Cheng Y, Liaw PK. High-entropy Alloys with High Saturation Magnetization, Electrical Resistivity, and Malleability. *Sci Rep*. 2013;3:1455.

[81] Senkov ON, Senkova SV, Miracle DB, Woodward C. Mechanical properties of low-density, refractory multi-principal element alloys of the Cr–Nb–Ti–V–Zr system. *Mater Sci Eng A*. 2013;565:51-62.

[82] Guo W, Dmowski W, Noh J-Y, Rack P, Liaw P, Egami T. Local atomic structure of a high-entropy alloy: an x-ray and neutron scattering study. *Metall Mater Trans A*. 2013;44:1994-7.

- [83] Zhang Y, Zuo TT, Tang Z, Gao MC, Dahmen KA, Liaw PK, et al. Microstructures and properties of high-entropy alloys. *Prog Mater Sci.* 2014;61:1-93.
- [84] Tian F, Delczeg L, Chen N, Varga LK, Shen J, Vitos L. Structural stability of NiCoFeCrAl high-entropy alloy from *ab initio* theory. *Phys Rev B.* 2013;88:085128.
- [85] Miracle DB, Miller JD, Senkov ON, Woodward C, Uchic MD, Tiley J. Exploration and Development of High Entropy Alloys for Structural Applications. *Entropy.* 2014;16:494-525.
- [86] Tang Z, Huang L, He W, Liaw P. Alloying and Processing Effects on the Aqueous Corrosion Behavior of High-Entropy Alloys. *Entropy.* 2014;16:895-911.
- [87] Zhang Y, Lu ZP, Ma SG, Liaw PK, Tang Z, Cheng YQ, et al. Guidelines in predicting phase formation of high-entropy alloys. *MRS Communications.* 2014;4:57-62.
- [88] Huang PK, Yeh JW, Shun TT, Chen SK. Multi-principal-element alloys with improved oxidation and wear resistance for thermal spray coating. *Adv Eng Mater.* 2004;6:74-8.
- [89] Senkov ON, Scott JM, Senkova SV, Miracle DB, Woodward CF. Microstructure and room temperature properties of a high-entropy TaNbHfZrTi alloy. *J Alloys Compd.* 2011;509:6043-8.
- [90] Senkov ON, Wilks GB, Scott JM, Miracle DB. Mechanical properties of Nb₂₅Mo₂₅Ta₂₅W₂₅ and V₂₀Nb₂₀Mo₂₀Ta₂₀W₂₀ refractory high entropy alloys. *Intermetallics.* 2011;19:698-706.
- [91] Gao MC, Alman DE. Searching for Next Single-Phase High-Entropy Alloy Compositions. *Entropy.* 2013;15:4504-19.
- [92] Takeuchi A, Amiya K, Wada T, Yubuta K, Zhang W. High-Entropy Alloys with a Hexagonal Close-Packed Structure Designed by Equi-Atomic Alloy Strategy and Binary Phase Diagrams. *Jom-Us.* 2014:1-9.
- [93] Feuerbacher M, Heidelmann M, Thomas C. Hexagonal High-entropy Alloys. *Materials Research Letters.* 2014;1. DOI:10.1080/21663831.2014.951493.
- [94] Singh S, Wanderka N, Murty BS, Glatzel U, Banhart J. Decomposition in multi-component AlCoCrCuFeNi high-entropy alloy. *Acta Mater.* 2011;59:182-90.
- [95] Li C, Li JC, Zhao M, Jiang Q. Effect of aluminum contents on microstructure and properties of Al_xCoCrFeNi alloys. *J Alloys Compd.* 2010;504, Supplement 1:S515-S8.
- [96] Kao Y-F, Chen T-J, Chen S-K, Yeh J-W. Microstructure and mechanical property of as-cast, -homogenized, and -deformed Al_xCoCrFeNi (0 ≤ x ≤ 2) high-entropy alloys. *J Alloys Compd.* 2009;488:57-64.
- [97] Lin C-M, Tsai H-L, Bor H-Y. Effect of aging treatment on microstructure and properties of high-entropy Cu_{0.5}CoCrFeNi alloy. *Intermetallics.* 2010;18:1244-50.
- [98] Tsai CW, Chen YL, Tsai MH, Yeh JW, Shun TT, Chen SK. Deformation and annealing behaviors of high-entropy alloy Al_{0.5}CoCrCuFeNi. *J Alloys Compd.* 2009;486:427-35.
- [99] Kuznetsov AV, Shaysultanov DG, Stepanov ND, Salishchev GA, Senkov ON. Tensile

properties of an AlCrCuNiFeCo high-entropy alloy in as-cast and wrought conditions. *Mater Sci Eng A*. 2012;533:107-18.

[100] Chou HP, Chang YS, Chen SK, Yeh JW. Microstructure, thermophysical and electrical properties in $\text{Al}_x\text{CoCrFeNi}$ ($0 \leq x \leq 2$) high-entropy alloys. *Mater Sci Eng, B*. 2009;163:184-9.

[101] Ng C, Guo S, Luan J, Shi S, Liu CT. Entropy-driven phase stability and slow diffusion kinetics in an $\text{Al}_{0.5}\text{CoCrCuFeNi}$ high entropy alloy. *Intermetallics*. 2012;31:165-72.

[102] Hsieh K-C, Yu C-F, Hsieh W-T, Chiang W-R, Ku JS, Lai J-H, et al. The microstructure and phase equilibrium of new high performance high-entropy alloys. *J Alloys Compd*. 2009;483:209-12.

[103] Tsai CW, Tsai MH, Yeh JW, Yang CC. Effect of temperature on mechanical properties of $\text{Al}_{0.5}\text{CoCrCuFeNi}$ wrought alloy. *J Alloys Compd*. 2010;490:160-5.

[104] Wang W-R, Wang W-L, Wang S-C, Tsai Y-C, Lai C-H, Yeh J-W. Effects of Al addition on the microstructure and mechanical property of $\text{Al}_x\text{CoCrFeNi}$ high-entropy alloys. *Intermetallics*. 2012;26:44-51.

[105] Wang YP, Li BS, Ren MX, Yang C, Fu HZ. Microstructure and compressive properties of AlCrFeCoNi high entropy alloy. *Mater Sci Eng A*. 2008;491:154-8.

[106] Cui HB, Wang Y, Wang JY, Guo XF, Fu HZ. Microstructural evolution and corrosion behavior of directionally solidified FeCoNiCrAl high entropy alloy. *China Foundry*. 2011;8:259-63.

[107] Zhu JM, Fu HM, Zhang HF, Wang AM, Li H, Hu ZQ. Microstructure and compressive properties of multiprincipal component AlCoCrFeNiC_x alloys. *J Alloys Compd*. 2011;509:3476-80.

[108] Ma SG, Zhang Y. Effect of Nb addition on the microstructure and properties of AlCoCrFeNi high-entropy alloy. *Mater Sci Eng A*. 2012;532:480-6.

[109] Wang FJ, Zhang Y, Chen GL, Davies HA. Cooling rate and size effect on the microstructure and mechanical properties of AlCoCrFeNi high entropy alloy. *J Eng Mater Technol*. 2009;131.

[110] Zhu JM, Fu HM, Zhang HF, Wang AM, Li H, Hu ZQ. Microstructures and compressive properties of multicomponent AlCoCrFeNiMox alloys. *Mater Sci Eng, A*. 2010;527:6975-9.

[111] Li C, Zhao M, Li JC, Jiang Q. B2 structure of high-entropy alloys with addition of Al. *J Appl Phys*. 2008;104:113504.

[112] Wang W-R, Wang W-L, Yeh J-W. Phases, microstructure and mechanical properties of $\text{Al}_x\text{CoCrFeNi}$ high-entropy alloys at elevated temperatures. *J Alloys Compd*. 2014;589:143-52.

[113] Zhang Y. Mechanical properties and structures of high entropy alloys and bulk metallic glasses composites. *Mater Sci Forum*. 2010;654-656:1058-61.

[114] Widom M, Huhn WP, Maiti S, Steurer W. Hybrid Monte Carlo/Molecular Dynamics Simulation of a Refractory Metal High Entropy Alloy. *Metall Mat Trans A*. 2014;45:196-200.

- [115] Joubert JM. Crystal chemistry and Calphad modeling of the sigma phase. *Prog Mater Sci.* 2008;53:528-83.
- [116] Cao HB, Pan Y, Ding L, Zhang C, Zhu J, Hsieh KC, et al. Synthesis of copper-rich amorphous alloys by computational thermodynamics. *Acta Mater.* 2008;56:2032-6.
- [117] Bei H, Yang Y, Viswanathan GB, Rawn CJ, George EP, Tiley J, et al. Formation, stability and crystal structure of the σ phase in Mo–Re–Si alloys. *Acta Mater.* 2010;58:6027-34.
- [118] Yang Y, Zhang C, Chen S, Morgan D, Chang YA. First-principles calculation aided thermodynamic modeling of the Mo–Re system. *Intermetallics.* 2010;18:574-81.
- [119] Zhang C, Zhang F, Chen S, Cao W. Computational thermodynamics aided high-entropy alloy design. *Jom-U.S.* 2012;64:839-45.
- [120] Chou K-C, Austin Chang Y. A Study of Ternary Geometrical Models. *Berichte der Bunsengesellschaft für physikalische Chemie.* 1989;93:735-41.
- [121] Zhang C, Zhang F, Chen S-L, Cao W-S, Chang Y. Thermodynamic modeling and experimental investigation of the phase stability at the Ni-rich region of the Ni–Al–Cr–Ir system. *Acta Mater.* 2011;59:6246-56.
- [122] Zhang C, Gao M, Yang Y, Zhang F. Thermodynamic modeling and first-principles calculations of the Mo–O system. *Calphad.* 2014;45:178-87.
- [123] Scheil E. Über die Eutektische Kristallisation (On Eutectic Crystallization). *Z Metallkd.* 1942;34:70-2.
- [124] Tsai M-H, Yuan H, Cheng G, Xu W, Tsai K-Y, Tsai C-W, et al. Morphology, structure and composition of precipitates in Al_{0.3}CoCrCu_{0.5}FeNi high-entropy alloy. *Intermetallics.* 2013;32:329-36.
- [125] Bergman G, Shoemaker DP. The Determination of the Crystal Structure of the Sigma-Phase in the Iron Chromium and Iron Molybdenum Systems. *Acta Crystallogr.* 1954;7:857-65.
- [126] Chen J, Young B. Stress-strain curves for stainless steel at elevated temperatures. *Eng Struc.* 2006;28:229-39.
- [127] Venkatesh V, Rack HJ. Elevated temperature hardening of INCONEL 690. *Mech Mater.* 1998;30:69-81.
- [128] Schaeublin R, Leguey T, Spatig P, Baluc N, Victoria M. Microstructure and mechanical properties of two ODS ferritic/martensitic steels. *J Nucl Mater.* 2002;307:778-82.
- [129] Sundar RS, Deevi SC. High-temperature strength and creep resistance of FeAl. *Mater Sci Eng A.* 2003;357:124-33.
- [130] Li JC, Wu TY, Riquier Y. Sigma-phase precipitation and its effect on the mechanical-properties of a super duplex stainless-steel. *Mater Sci Eng A.* 1994;174:149-56.
- [131] Liu CT. Recent advances in ordered intermetallics. *Mater Chem Phys.* 1995;42:77-86.
- [132] Sikka VK, Deevi SC, Viswanathan S, Swindeman RW, Santella ML. Advances in processing of Ni₃Al-based intermetallics and applications. *Intermetallics.* 2000;8:1329-37.

- [133] Noh S, Kasada R, Kimura A. Solid-state diffusion bonding of high-Cr ODS ferritic steel. *Acta Mater.* 2011;59:3196-204.
- [134] Hirata A, Fujita T, Wen YR, Schneibel JH, Liu CT, Chen MW. Atomic structure of nanoclusters in oxide-dispersion-strengthened steels. *Nat Mater.* 2011;10:922-6.
- [135] Liu CT, Schneibel JH, Maziasz PJ, Wright JL, Easton DS. Tensile properties and fracture toughness of TiAl alloys with controlled microstructures. *Intermetallics.* 1996;4:429-40.
- [136] Liu Z, Guo S, Liu X, Ye J, Yang Y, Wang X-L, et al. Micromechanical characterization of casting-induced inhomogeneity in an Al_{0.8}CoCrCuFeNi high-entropy alloy. *Scripta Mater.* 2011;64:868-71.
- [137] Ishida K, Nishizawa T. The Co-Cr (Cobalt-Chromium) system. *J Phase Equilib.* 1990;11:357-70.
- [138] ASM International. Alloy Phase Diagram Committee., ASM International. Handbook Committee. ASM handbook. Materials Park, Ohio: ASM International; 1992.
- [139] Senkov ON, Scott JN, Senkova SV, Meisenkothen F, Miracle DB, Woodward CF. Microstructure and elevated temperature properties of a refractory TaNbHfZrTi alloy. *J Mater Sci.* 2012;47:4062-74.
- [140] He JY, Liu WH, Wang H, Wu Y, Liu XJ, Nieh TG, et al. Effects of Al addition on structural evolution and tensile properties of the FeCoNiCrMn high-entropy alloy system. 101016/jactamat201309037 *Acta Mater.* 2013.
- [141] Lucas MS, Wilks GB, Mauger L, Munoz JA, Senkov ON, Michel E, et al. Absence of long-range chemical ordering in equimolar FeCoCrNi. *Appl Phys Lett.* 2012;100:251907.
- [142] Otto F, Dlouhý A, Somsen C, Bei H, Eggeler G, George EP. The influences of temperature and microstructure on the tensile properties of a CoCrFeMnNi high-entropy alloy. *Acta Mater.* 2013;61:5743-55.
- [143] Wu Z, Bei H, Otto F, Pharr GM, George EP. Recovery, recrystallization, grain growth and phase stability of a family of FCC-structured multi-component equiatomic solid solution alloys. *Intermetallics.* 2014;46:131-40.
- [144] Senkov ON, Senkova SV, Woodward C. Effect of aluminum on the microstructure and properties of two refractory high-entropy alloys. *Acta Mater.* 2014;68:214-28.
- [145] Bei H, Shim S, George E, Miller M, Herbert E, Pharr G. Compressive strengths of molybdenum alloy micro-pillars prepared using a new technique. *Scripta Mater.* 2007;57:397-400.
- [146] Bei H, Shim S, Pharr GM, George EP. Effects of pre-strain on the compressive stress-strain response of Mo-alloy single-crystal micropillars. *Acta Mater.* 2008;56:4762-70.
- [147] Hou JS, Zhou LZ, Yuan C, Tang Z, Guo JT, Qin XZ, et al. The effect of reheat treatments on recovering the creep behavior of a corrosion-resistant nickel-based superalloy. *Mater Sci Eng A.* 2013;560:25-33.
- [148] Vander Voort GF. Metallography, principles and practice. New York: New York :

McGraw-Hill; 1984.